Carlos Filipe Santos Costa

BSc in Cell and Molecular Biology

Interaction between gold nanoparticles and blood proteins to define disease states

Dissertation for the Master's Degree in Biochemistry

Supervisor: Prof. Dr. José Ricardo Ramos Franco Tavares, UCIBIO, REQUIMTE, Departamento de Química, Faculdade de Ciências e Tecnologia, Universidade NOVA de Lisboa

Co-supervisor: Prof. Dr. Ludwig Krippahl, NOVA LINCS, Departamento de Informática, Faculdade de Ciências e Tecnologia, Universidade NOVA de Lisboa

Jury:

Presidente:	Prof. Dr. Carlos Alberto Gomes Salgueiro
Arguente:	Prof. Dr. Nuno Correia Santos
Vogal:	Prof. Dr. José Ricardo Ramos Franco Tavares

FACULDADE DE CIÊNCIAS E TECNOLOGIA
UNIVERSIDADE NOVA DE LISBOA

September 2019

Interaction between gold nanoparticles and blood proteins to define disease states

This page intentionally left blank

Acknowledgements

To my supervisors, Professor Ricardo Franco and Professor Ludwig Krippahl, for the opportunity to work on such an interesting topic, combining the fields of bionanotechnology and bioinformatics for innovative and promising approaches to biomedical research and development of novel diagnostic tools; and for all the orientation and help throughout this investigation.

To Miguel Peixoto de Almeida, PhD and Professor Eulália Pereira from Faculdade de Ciências da Universidade do Porto, for kindly answering my questions as they arose and for the materials provided, which were essential for this dissertation.

To everyone I met working on laboratory 603: to Maria João Oliveira, for being a good friend with whom I learned much; to David Peitinho, for briefing this topic and aiding with my questions; to Marina Bento, Bruno Guerreiro, Rosaceleste Zumpano, Rocío Jurado and Diego Wiechers, for all the valuable advices and moments of leisure; and to João Cadete, Rafaela Martins and Tiago Roquito, for being the best students they were in my first experience as a co-supervisor to a bachelor's dissertation.

To all my colleagues from the Master in Biochemistry, for having me integrated amongst some of the friendliest people I know.

To anTUNiA – Tuna de Ciências e Tecnologia da Universidade NOVA de Lisboa, for contributing to maintaining a productive mind by providing a musical distraction in great company.

Last – but definitely not least – to my family, for making all of this possible and for the investment and support throughout my academic path.

This page intentionally left blank

Abstract

Noble metal nanoparticles constitute promising biosensors due to a high and tailored affinity to biomolecules such as proteins, forming protein coronas of distinct compositions on the surface. Gold nanoparticles (AuNP) are particularly interesting for a relatively easy, quick and inexpensive synthesis, low toxicity and ease of functionalization with bifunctional molecules, which typically have thiol groups bound to the AuNP surface and bio-friendly chemical groups at the opposite end, allowing for controlled protein adsorption. Functionalized AuNP can be used as probing agents for blood samples and health states determined by the protein corona composition, which is divided into a strongly bound innermost hard corona and a looser external soft corona.

The objective of this work was to further understand the behaviour of plasma proteins integrating the corona. To attain these objectives, conjugates were prepared with ca. 15 and 40 nm diameter AuNP and two important plasma proteins: serum albumin and fibrinogen.

AuNP synthesis was by a modified Turkevich method, with diameter and concentration determined by UV-Vis spectroscopy. AuNP were functionalized with 11-mercaptoundecanoic acid and conjugated with bovine or human serum albumin or fibrinogen. These single protein conjugates were evaluated for colloidal stability with ionic strength and pH variation through UV-Vis, protein conformational changes through circular dichroism (CD), hydrodynamic diameter changes upon centrifugation through dynamic light scattering (DLS) and electrophoretic mobility and concentration dependent conjugation efficiency were determined through agarose gel electrophoresis (AGE). Analysis of AGE profiles was by the open source electrophoresis gel image processing software eReuss.

CD confirmed α-helix loss for conjugated serum albumins. DLS showed a hydrodynamic diameter decrease for centrifuged 42 nm AuNP conjugates, with high polydispersity indexes for 13 nm ones, suggesting aggregation. AGE revealed electrophoretic mobility decreases as the protein:AuNP ratio increases, data fitted to a Langmuir adsorption model.

Serum albumin undergoes conformational alterations upon conjugation with AuNP. Centrifugation affects the protein corona, despite its tendency to aggregate AuNP. Overall, CD, DLS and AGE were demonstrated as useful techniques for the characterisation of the protein corona.

Keywords: Blood plasma proteins, protein corona, gold nanoparticles, circular dichroism, dynamic light scattering, electrophoresis

This page intentionally left blank

Resumo

Nanopartículas de metais nobres constituem biossensores promissores devido a uma elevada e configurável afinidade para biomoléculas como proteínas, formando coroas proteicas de composições distintas à superfície. Nanopartículas de ouro (AuNP) são particularmente interessantes pela síntese relativamente fácil, rápida e económica, baixa toxicidade e facilidade de funcionalização com moléculas bifuncionais com grupos tiol ligados à superfície das AuNP e grupos químicos biocompatíveis na extremidade oposta, permitindo a adsorção controlada de proteínas. AuNP funcionalizadas podem ser usadas como sondas em amostras de sangue, sendo o estado de saúde determinado pela composição da coroa proteica, a qual é dividida numa *hard corona* interna fortemente ligada e numa *soft corona* externa fracamente ligada.

O objetivo deste trabalho foi melhorar a compreensão do comportamento das proteínas do plasma integrando a corona. Para atingir este objetivo, conjugados foram preparados com AuNP de ca. 15 e 40 nm de diâmetro e duas importantes proteínas do plasma: albumina do soro e fibrinogénio.

A síntese das AuNP seguiu um método de Turkevich modificado, sendo o diâmetro e concentração determinados através de UV-Vis. As AuNP foram funcionalizadas com ácido 11-mercaptoundecanóico e conjugadas com albumina do soro ou fibrinogénio bovinos ou humanos. Conjugados foram avaliados pela estabilidade coloidal variando força iónica ou pH por UV-Vis, pelas modificações conformacionais nas proteínas por dicroísmo circular (CD), pela diferença no diâmetro hidrodinâmico após centrifugação por dispersão dinâmica de luz (DLS) e a mobilidade eletroforética e eficácia de conjugação dependente da concentração determinadas por eletroforese em gel de agarose (AGE), cujos perfis foram analisados pelo programa eReuss.

CD confirmou perda de α-hélices em conjugados de albumina do soro. DLS apresentou um decréscimo no diâmetro hidrodinâmico de conjugados de AuNP de 42 nm centrifugados, com altos índices de polidispersidade nos de 13 nm, sugerindo agregação. AGE revelou que a mobilidade eletroforética diminui com o aumento da razão proteína:AuNP, dados ajustados a um modelo de adsorção de Langmuir.

A albumina do soro sofre alterações conformacionais após conjugação com AuNP. A centrifugação afeta a coroa proteica, apesar da tendência para agregar AuNP. CD, DLS e AGE foram demonstradas como sendo técnicas úteis para a caracterização da coroa proteica.

Termos chave: Proteínas do plasma sanguíneo, coroa proteica, nanopartículas de ouro, dicroísmo circular, dispersão dinâmica de luz, eletroforese

This page intentionally left blank

Table of contents

List of figures

List of tables

This page intentionally left blank

List of abbreviations

ACF	Auto-correlation function
AF4	Asymmetrical flow field flow fractionation
AFM	Atomic force microscopy
AGE	Agarose gel electrophoresis
APBS	Adaptative Poisson-Boltzmann solver
AuNP	Gold nanoparticle(s)
BPF	Bovine plasma fibrinogen
BSA	Bovine serum albumin
CCC	Critical coagulation concentration
CD	Circular dichroism
DLS	Dynamic light scattering
DLVO	Derjaguin, Landau, Verwey, and Overbeek
EDL	Electric double layer
FTIR	Fourier transform infrared spectroscopy
HC	Hard corona
HPF	Human plasma fibrinogen
HSA	Human serum albumin
LSPR	Localised surface plasmon resonance
MADLS	Multi-angle dynamic light scattering
MUA	11-mercaptoundecanoic acid
NTA	Nanoparticle tracking analysis
PDB	Protein data bank
PDI	Polydispersity index
pI	Isoelectric point
RCSB	Research collaboratory for structural bioinformatics
SAM	Self-assembled monolayer
SAXS	Small angle X-ray scattering
SC	Soft corona
SDS-PAGE	Sodium dodecyl sulphate-polyacrylamide gel electrophoresis
SLS	Static light scattering
SPR	Surface plasmon resonance
TAE	Tris-acetate-ethylenediaminetetraacetic acid
TEM	Transmission electron microscopy
UniProt	Universal protein resource
UV-Vis	Ultraviolet-visible

This page intentionally left blank

1 Introduction

1.1 Blood proteins

Blood is amongst the most abundant body fluids in animals, acting as the main transportation network in the entire organism, reaching out to deliver nutrients and oxygen to all cells whilst collecting metabolic waste products for disposal, as well as a vehicle for immune response and wound sealing and a body temperature regulator. It can be fractioned into a solid and a liquid phase. The former comprises the blood cells and makes up approximately 45% of its total volume, most of which being erythrocytes, with leukocytes and platelets falling under < 1%, although the erythrocyte volume percentage – known as the haematocrit – varies according to some factors such as gender, with normal values ranging from 42% to 52% in males and from 37% to 47% in females. Despite the proteins found on blood cells, such as haemoglobin, the majority of all blood proteins are contained in the blood plasma – the liquid phase making up the remaining approximate 55% of the total blood volume. At 7% of the total blood plasma volume, the hundreds of different types of blood plasma proteins represent its major constituents besides water, which makes up 92% of plasma. These free circulating blood plasma proteins can be categorised into three groups – albumin, globulins and fibrinogen (table 1.1).[1–3]

Table 1.1. Blood plasma constituents. Adapted from [1].

Plasma constituent and abundance	Constituent type and abundance	Production site	Major function(s)
Water 92%	Fluid	Absorbed in intestine; metabolised	Transport medium
Plasma proteins 7%	Albumin 54-60%	Liver	Transport; maintain osmotic concentration
	Globulins 35-38%	α-globulins – liver	Transport; maintain osmotic concentration
		β-globulins – liver	Transport; maintain osmotic concentration
		γ-globulins – plasma cells	Immune response
	Fibrinogen 4-7%	Liver	Blood clotting in haemostasis
Regulatory proteins < 1%	Hormones and enzymes	Various sources	Regulate various body functions
Other solutes 1%	Nutrients, gases and wastes	Various sources	Numerous and varied

As blood flows throughout the organism, it suffers alterations to its plasma protein concentrations when passing through diseased cells or tissues. By completely characterising how the plasma protein profile of a healthy individual changes in accordance to natural factors, such as genetic background, age, disease history and life style, it is possible to define a baseline against which diseased plasma protein profiles can be compared in order to define disease states.[4–8] The present work focused on albumin and fibrinogen.

1.1.1 Serum albumin

The most abundant protein in blood plasma, serum albumin is a monomeric globular protein of approximately 67 kDa, which is produced in the liver and acts as a versatile transportation protein, being capable of binding to and carrying along the bloodstream hydrophobic biomolecules, such as fatty acids, as well as hormones and even certain drugs. It is comprised of three homologous domains (I, II and III), each divided into two sub-domains named A and B, of six and four α-helices, respectively. Hydrophobic pockets in the sub-domains IIA and IIIA – designated Sudlow's sites I and II, respectively – are known binding points for some ligands, such as drugs. Structurally, serum albumin consists of 67% α-helices, with the remainder being random coils, stabilised by 17 internal disulphide bridges between 34 cysteine residues into an equilateral triangle shape (figure 1.1), which it retains under a pH range from 4.5 to 8.0 and beyond which this natural shape unfolds. In aged protein solutions, serum albumin dimers may sometimes form through the free Cys-34 thiol group.[9–14]

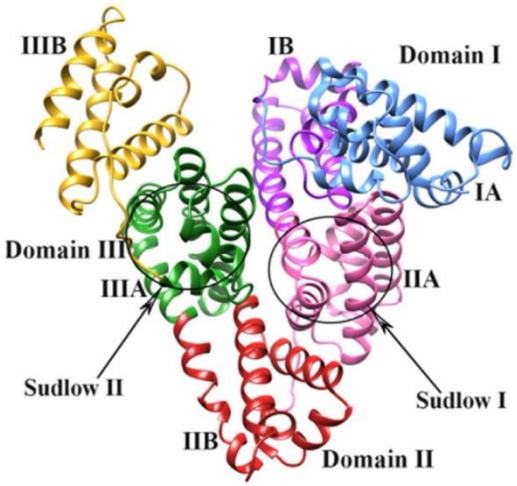

Figure 1.1. Structural representation of human serum albumin and its domains, sub-domains and Sudlow's binding sites I and II.[9]

1.1.2 Fibrinogen

Despite being the least abundant of the three blood plasma protein groups, comprising 4-7% of all plasma proteins[1], fibrinogen is a rather individually abundant protein in blood, at 3 mg/mL[15]; and an essential factor to the coagulation cascade and a unique and vital protein in the organism, its presence or absence differentiating between plasma and serum, respectively. A rod-shaped glycoprotein of approximately 340 kDa produced in the liver, fibrinogen is composed of three symmetrical pairs of polypeptide chains, designated Aα, Bβ and γ, which are held together by disulphide bridges and mainly comprised of coiled coils extended linearly, with three distinct globular domains formed at the chain termini regions. A central domain (E) contains the termini of all three pairs of chains, whilst at the two distal domains, located on both extremities of the molecule (D), are the C-termini of the Bβ and γ chains. In response to injury, fibrinogen, a soluble protein, is cleaved by the serine protease thrombin into insoluble fibrin monomers, which polymerise into fibrils and subsequently branch to form a clot (figure 1.2).[15–20]

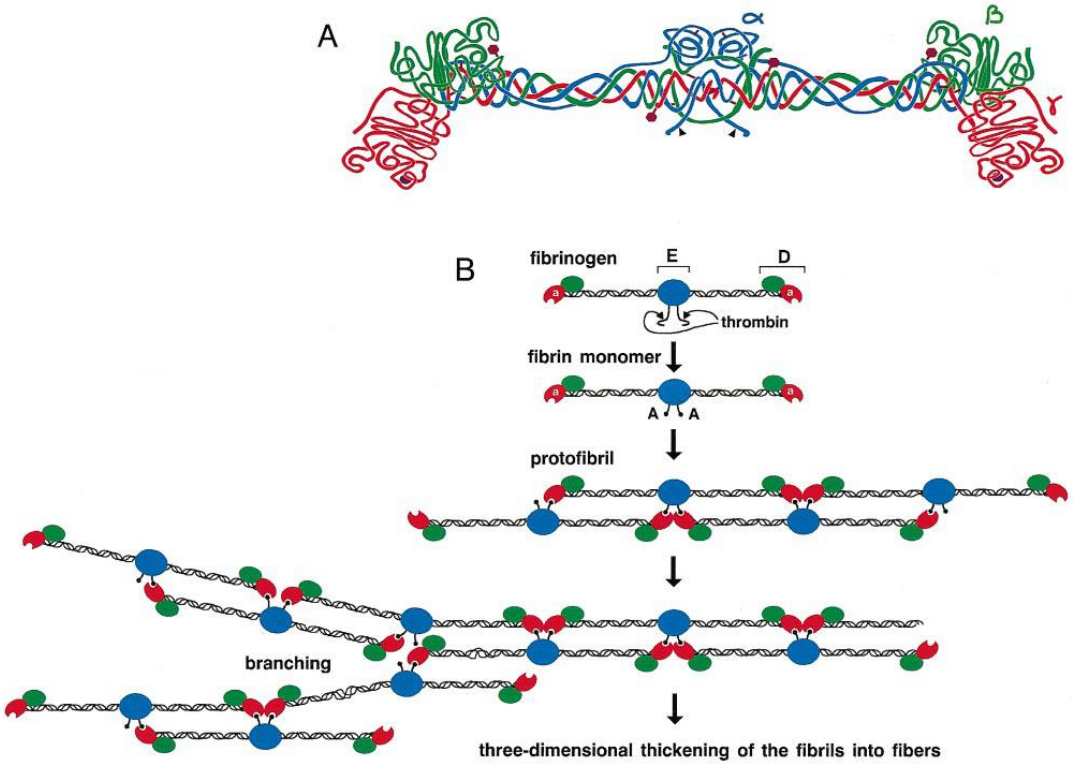

Figure 1.2. Structural representation of human fibrinogen and its Aα (blue), Bβ (green) and γ (red) chains (A) and a depiction of the fibrin polymerisation process through the cleavage of fibrinopeptides by thrombin (B).[15]

The C-termini of the Aα chains are typically associated with the E domain through non-covalent interactions, although these chains are known to suffer conformational alterations depending on solution conditions such as pH or ionic strength, further changing the shape of the fibrinogen molecule beyond its already inherent flexibility. Under physiological conditions, including a pH = 7.4 – that of healthy blood – fibrinogen is mostly found in a semi-collapsed conformation, as the electrostatic potential at the E domain becomes negatively charged, causing an electrostatic attraction of the positively charged C-termini of the Aα chains (figure 1.3).[21]

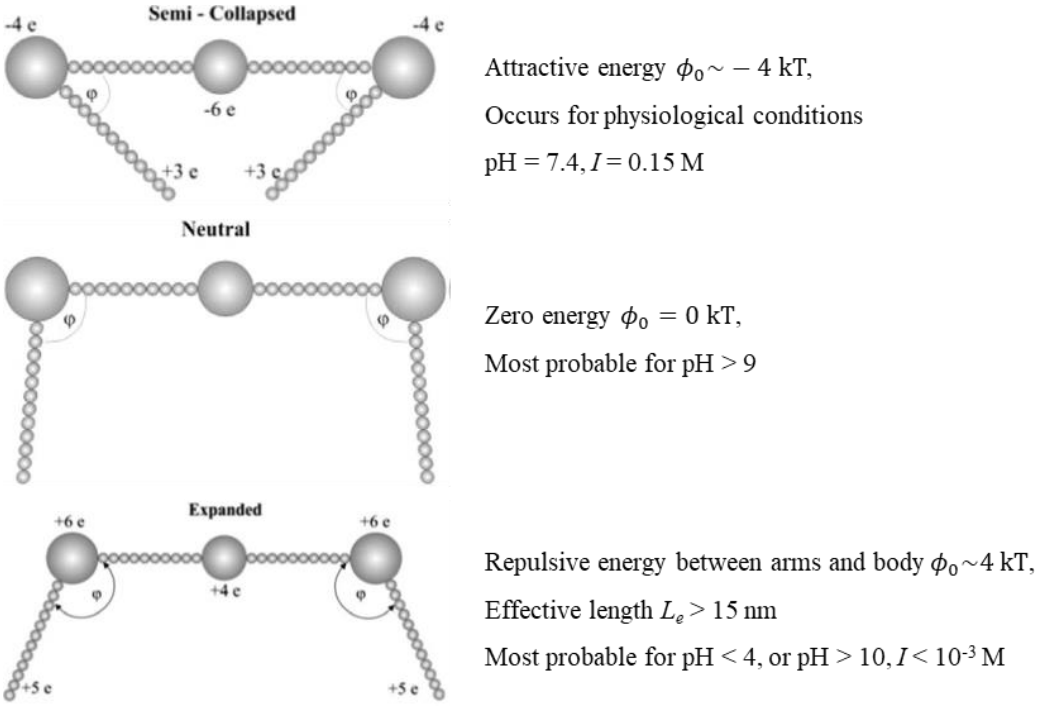

Figure 1.3. Predicted fibrinogen conformations depending on solution conditions. Adapted from [21].

1.2 Gold nanoparticles

Nanoparticles of various compositions and shapes can and have been utilised in studies resorting to the characterisation of a protein corona formed from blood plasma proteins in order to define diseases and states thereof.[22–25] The present work focused on spherical gold nanoparticles (AuNP) and further exploited the potential and interesting properties of the AuNP for diagnostic purposes.

AuNP consist of structures made of elemental gold in a size range of 1-100 nanometres, in which nanotechnological and biomedical interest has grown in recent years due to an easy and quick synthesis and the unique and exploitable physicochemical and optical properties gold possesses at the nanoscale. AuNP retain great stability whilst also showing high versatility, with possible applications ranging from imaging, sensing, assisted drug delivery or cancer therapy. The ease of imparting functionality to these nanoparticles with different functionalization molecules contributes to this versatility. Moreover, these nanostructures also present relatively low cytotoxicity, making AuNP excellent candidates for *in vivo* applications, which complement the high accessibility to biological cells or tissues inherent to particles this small.[26–31]

In any metal surface of small dimensions, incident light excites the free electrons of metal atoms at the media interface into oscillating in resonance with its electric field. Such free electron oscillations are collectively denominated a plasmon (plasma + boson), since the negatively charged electron clouds are displaced from the respective equilibrium position at a lattice of positively charged ions – as occurs in plasma – and oscillate at a quite precise frequency, classifying as a bosonic quasi-particle excitation. This effect is known as surface plasmon resonance (SPR) and causes the absorption of incident light at specific wavelengths, unique for each surface of different compositions, sizes or surface modifications. However, this phenomenon does not occur in bulk metal, as the plasmon and photon energy dispersion curves never intersect in the internal atoms. Should the plasmons be confined to a structure smaller than the wavelength of the incident light, such as a nanoparticle, then the SPR is said to be localised (LSPR) (figure 1.4).

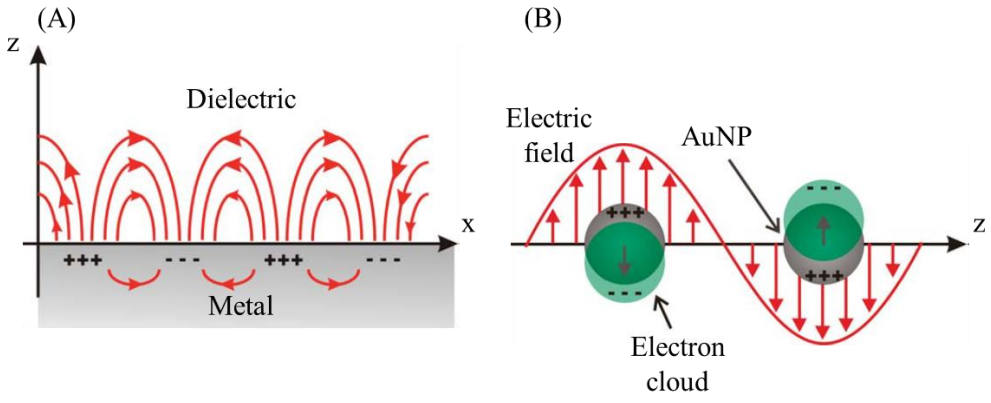

Figure 1.4. The electric field of incident light induces the SPR phenomenon on a metal surface (A) or its localised variant, LSPR if the surface plasmons are confined to a structure smaller than the wavelength of the incident light (B), such as nanoparticles. Adapted from [32].

In the case of monodisperse 15 nm AuNP, for example, the LSPR effect causes the absorption of light at a wavelength of approximately 520 nm, whilst red light is entirely reflected, hence the red colour characteristic to colloidal gold suspensions. Certain alterations to the absorption spectrum convey much information regarding the nanoparticles in study. For instance, shifts in the absorption peak can indicate the adsorption of some substance to the surface of the nanoparticle, changing the refractive index of the immediate medium surrounding it and thus altering the wavelengths affected by the LSPR. Other effects include an increased absorption spectrum width or having more than one absorption peak, which are all indicative of polydispersity and due to the LSPR coupling of nanoparticle populations of different sizes. Furthermore, larger nanoparticles absorb light with more intensity than smaller ones (figure 1.5).[32–36]

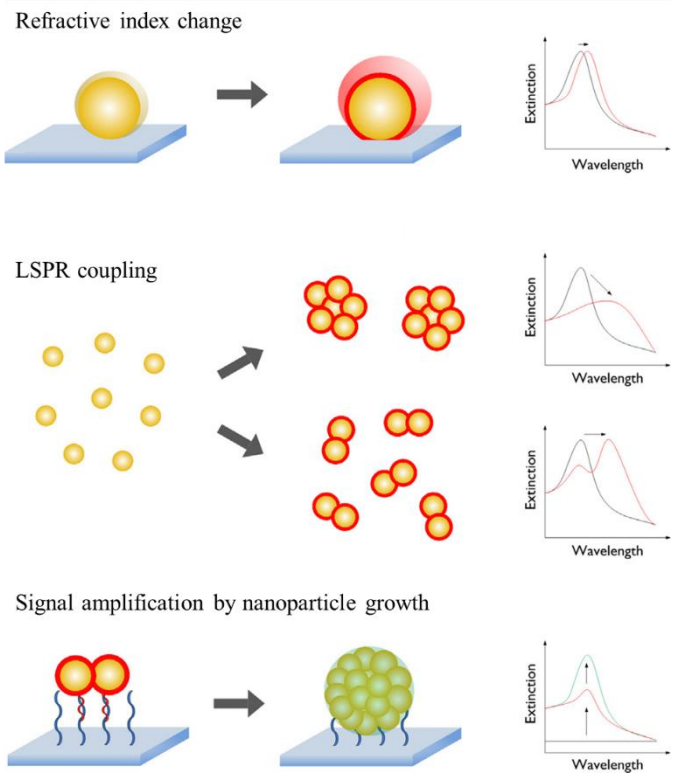

Figure 1.5. Some exploitable LSPR alterations on plasmonic nanoparticles include refractive index change based on surface composition, signal coupling characteristic to nanoparticle aggregation or signal amplification with the increase of nanoparticle size. Adapted from [34].

1.2.1 Synthesis

AuNP can be synthesised through various methods, some based on a top-down approach, others on a bottom-up chemical reaction, namely the reduction of a gold salt. The synthesis method determines the shape and size of the AuNP. For this work, the simple bottom-up chemical approach first described by Turkevich et al. was used, which relies on chloroauric acid ($HAuCl_4$) as a gold precursor and sodium citrate ($Na_3C_6H_5O_7$) as a reducing agent, both heated in an aqueous solution, in which several reactions occur in parallel, the first in a sequence being the oxidation of citrate into dicarboxy acetone, promoting the reduction of auric salt into aurous salt, which subsequently disproportionates to gold atoms:

$$C_6H_5O_7^{3-} \rightarrow C_5H_4O_5^{2-} + CO_2 + H^+ + 2e^- \qquad \text{Equation 1.1}$$

$$AuCl_3 + 2e^- \rightarrow AuCl + 2Cl^- \qquad \text{Equation 1.2}$$

$$3AuCl \rightarrow 2Au^0 + AuCl_3 \qquad \text{Equation 1.3}$$

As the concentration of disproportionated gold atoms increases, these aggregate to form nuclei which grow by absorbing further gold atoms produced by disproportionation (figure 1.6).

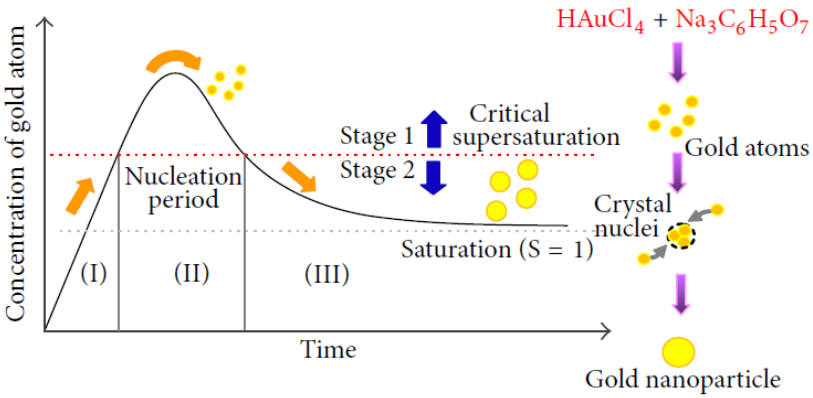

Figure 1.6. Synthesis of AuNP through citrate reduction.[37]

Sodium citrate acts as the reducing agent as well as a capping agent which stabilises the surface of the AuNP during the growth phase. Thus, by altering its concentration, it is possible to adjust the size of synthesised nanoparticles, since having less citrate present results in fewer ions to stabilise the surface of the AuNP, allowing these to grow larger.[37–40] Additionally, the order in which the gold precursor and the reducing agent are added to the reaction affects the polydispersity of AuNP. Whilst Turkevich et al. added sodium citrate to a heated chloroauric acid solution, which became known as the "direct method"; the reverse order, or the "reverse method", has been observed to yield less polydisperse nanoparticles, since heating the sodium citrate prior to adding the chloroauric acid ensures its partial oxidation before coming into contact with the gold salt, therefore substantially increasing the nucleation and growth rates and greatly narrowing the size distribution (figure 1.7).[41]

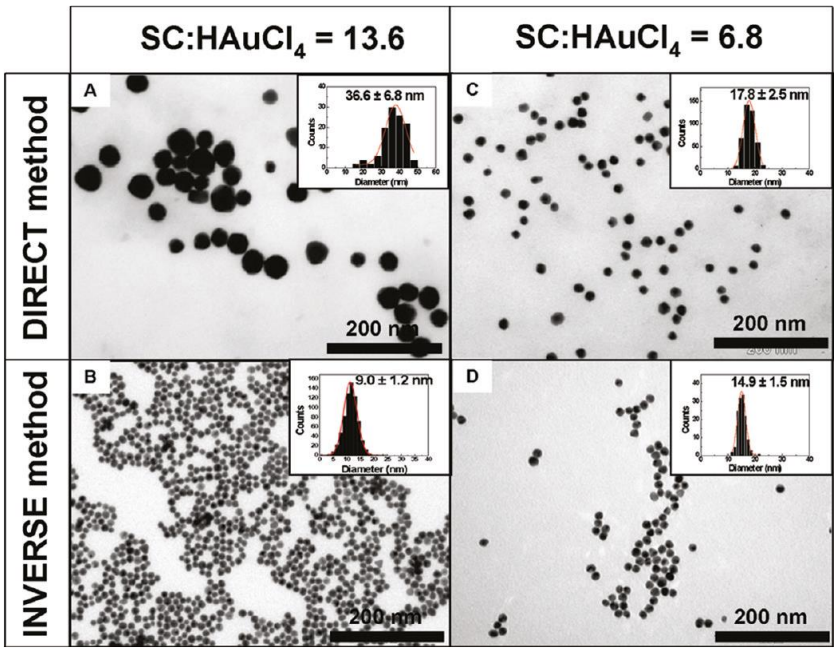

Figure 1.7. Transmission electron microscopy (TEM) morphological characterisation of AuNP synthesised using the direct and inverse methods with two citrate:$HAuCl_4$ ratios. Size distribution is represented in the inset graphs.[41]

1.2.2 Electric double layer

Nanoparticles can be found in the form of colloids – solid particles suspended in a continuous liquid – and, as such, can acquire the electric charge of adsorbed ions found in the colloidal suspension and attract counterions of an opposite charge, forming what is known as the electric double layer (EDL). At the closest proximity to the surface of the nanoparticle, the Stern layer is exclusively composed of counterions – therefore possessing the maximum electric potential – and is delimited by the Stern plane, beyond which begins the diffuse layer, comprised of counterions as well as ions of an identical charge to that imparted to the nanoparticle (figure 1.8). The electric potential is inversely proportional to the distance from the nanoparticle surface, becoming null at the edge of the EDL. As a nanoparticle diffuses through the colloid, a layer of the surrounding liquid becomes attached to its surface due to electrostatic forces derived from the EDL. The boundary between these captured molecules and the free ones is the slipping plane, located in the diffuse layer. The electric potential at the slipping plane is the ζ-potential (zeta potential) and is the only measurable value in the electric potential of a colloid.[42–44]

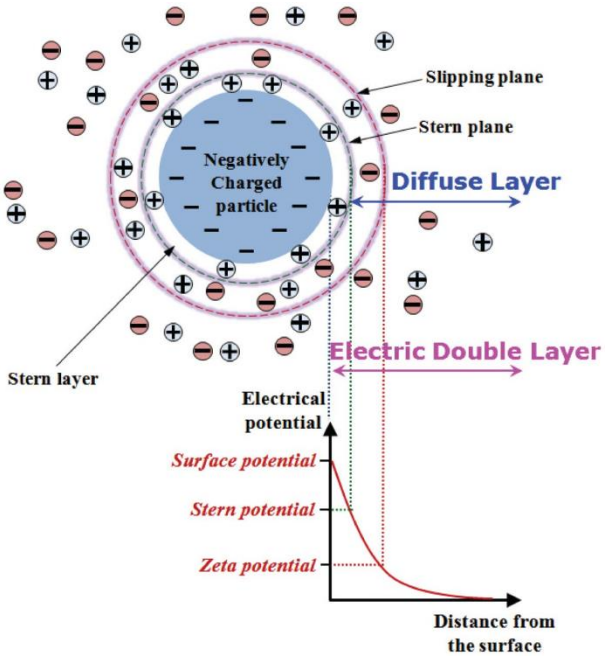

Figure 1.8. The electric double layer on a spherical particle with the electrical potential curve for each plane.[42]

In studies involving colloids, it is important to consider colloidal stability, which is explained by the DLVO theory – named after Derjaguin, Landau, Verwey and Overbeek – as the balance between the Coulombic or electrostatic repulsions and the van der Waals attractions amongst identically charged suspended particles. Therefore, the colloidal stability of nanoparticles of different compositions can be determined by the total interaction energy between two approaching particles (V_T) in function of the distance separating both (x), which is given as the sum of the van der Waals attractive potential energy (V_A) and the EDL repulsive potential energy (V_R), at that distance:

$$V_T(x) = V_A(x) + V_R(x) \qquad \text{Equation 1.4}$$

$$V_A(x) = -\frac{Ar}{12x} \qquad \text{Equation 1.5}$$

$$V_R(x) = 2\pi\varepsilon_r\varepsilon_0 r\zeta^2 e^{-\kappa x} \qquad \text{Equation 1.6}$$

A is the Hamaker constant, *r* the radius of the particles, ε_r the medium relative permittivity, ε_0 the vacuum permittivity, ζ the ζ-potential, *e* the elementary charge and κ the Debye-Hückel parameter, the reciprocal of which is known as the Debye length and represents the thickness of the EDL:

$$\kappa^{-1} = \sqrt{\frac{\varepsilon_r\varepsilon_0 k_B T}{2e^2 I}} \qquad \text{Equation 1.7}$$

k_B is the Boltzmann constant, *T* the temperature and *I* the ionic strength of the electrolytes. This also demonstrates how the electrolyte concentration affects the thickness of the EDL and, consequently, the ζ-potential.

As two identically charged colloidal particles approach, the total interaction energy tends from null to predominantly repulsive – the primary maximum – beyond which, at even shorter distances, the van der Waals attraction overcomes the EDL electrostatic repulsion – the primary minimum – and both particles become irreversibly aggregated. However, if the concentration of counterions is high enough, a secondary minimum appears at a slightly longer distance than that of the primary maximum, at which the particles undergo a weak and reversible aggregation designated flocculation (figure 1.9).[42,45,46]

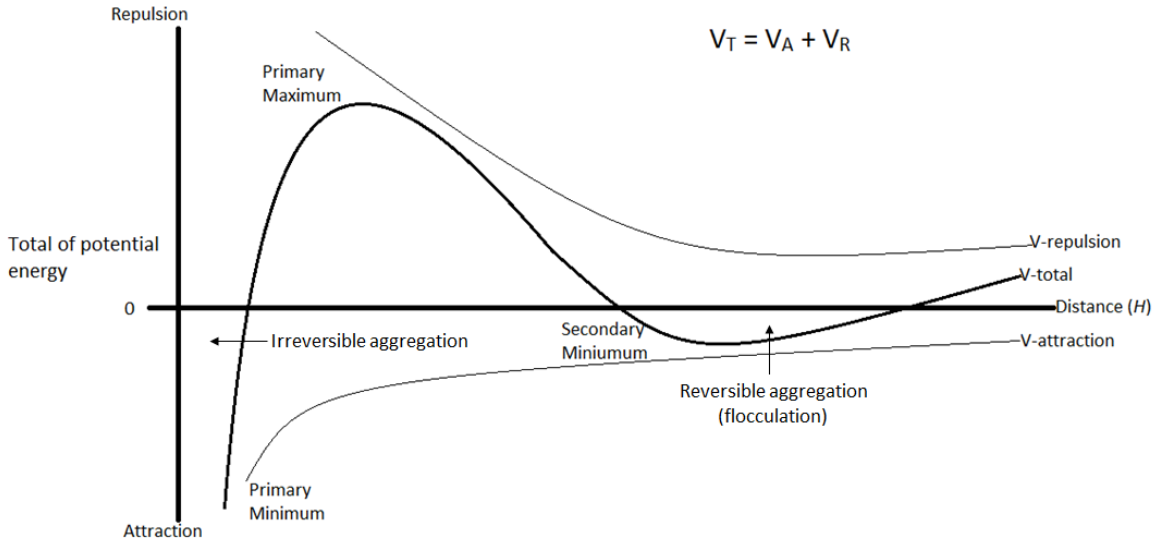

Figure 1.9. Total interaction energy between two colloidal particles in dependence of the separation distance, as per the DLVO theory. Adapted from [47].

Both the EDL electrostatic repulsions and van der Waals attractions amongst colloidal particles greatly depend on the distance between these. However, the attractive interactions are also proportional to particle size, being weaker on smaller particles, which are therefore more stable.[48] On the other hand, the EDL electrostatic repulsions are influenced by its thickness and the ζ-potential, which, as previously mentioned, are both affected by the electrolyte concentration. Monovalent salts, for example, can induce a momentary dipole, which weakens the repulsion of suspended particles.[42] The minimum concentration of counterions required for the aggregation of colloidal particles is denominated the critical coagulation concentration (CCC).[49,50] Moreover, the ζ-potential becomes virtually null at a colloid pH equal to the pI of the nanoparticles, as it reaches the point of zero charge and repulsive forces cease, which means these are most unstable and possess a high tendency to aggregate.[51] Alterations in the microenvironment such as increased ionic strength or lowered pH not only impact the stability of nanoparticles, but might also cause the desorption of proteins contained in the protein corona.[52]

1.2.3 Functionalization

Citrate binds to the surface of AuNP through physisorption, by weak and easily disrupted van der Waals interactions. In order to impart greater stability – thus avoiding aggregation – and introduce tailored functionality, AuNP are typically exposed to molecules with a higher affinity to the surface of these nanoparticles, such as thiolates, as the sulphur atom in the thiol group binds through chemisorption to the gold atoms[53] and effectively replaces citrate as a capping agent. These thiolated functionalization molecules include a terminal group opposite to the thiol group, which determines the surface chemistry and charge of the AuNP and through which molecules such as proteins adsorb to the nanoparticle, with the functionalization agent as an intermediate. A hydrophobic spacer exists between the thiol group and the functionalizing group, which promotes the formation of a self-assembled monolayer (SAM) of capping agent fully covering the surface of AuNP. For this work, 11-mercaptoundecanoic acid (MUA) was used as a capping agent, which possesses a carboxylic group at the functionalizing end, imparting AuNP with a negative surface charge and allowing for the electrostatic binding to the positively charged regions of the studied proteins (figure 1.10).[54,55] Furthermore, AuNP with a negatively charged surface have been demonstrated to exhibit less cytotoxicity than positively charged ones, therefore being more advantageous for *in vivo* diagnostics applications.[56]

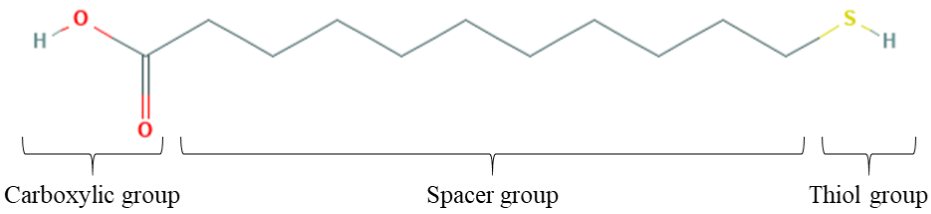

Figure 1.10. Structural representation of 11-mercaptoundecanoic acid. Molecule image generated with PubChem.

1.2.4 Conjugation

As diffusing proteins and capped AuNP come into contact, an initial adsorption depends on the electrostatic attraction forces between the charged surface of the nanoparticles and the amino acids with the opposite charge on the protein. Upon first contact, proteins remain adsorbed to the AuNP primarily through van der Waals forces, although hydrogen bonds can also occur between the proteins and AuNP capping molecules, as well as acid-base adducts, dipole-dipole interactions or London dispersion forces. Once adsorbed, proteins replace the ions and water molecules on the AuNP surface, whereas the AuNP occupy the protein solvent shell.[23]

The adsorption of proteins to a capped AuNP directly affects its electrophoretic mobility, as the surface charge of the nanoparticle is reduced. Furthermore, electrophoretic mobility variations can also be related to the degree of protein coverage the AuNP exhibits.[23] The electrophoretic mobility difference between unconjugated AuNP and AuNP with increasing single protein coverage degrees has been found to fit the Langmuir adsorption model.[11,22,23,57] This model fundamentally assumes proteins behave as an ideal gas at isothermal conditions and defines the loss of electrophoretic mobility as proportional to the occupancy of the AuNP surface, which depends on the free protein concentration and a thermodynamic equilibrium constant. Additionally, proteins are assumed to bind to definite surface sites, with each site having the capacity for one protein only; and also that the binding energy for each protein is independent of steric hindrance caused by proteins adsorbed to neighbouring sites.[58] One limitation to approximating AuNP-protein conjugation to this model is that the free protein concentration is assumed as equal to the initial protein concentration, whereas, in reality, the free protein concentration decreases over time as it is adsorbed to the surface of AuNP. This becomes increasingly more pronounced at lower initial protein concentrations. Another problem arises with the assumption of a linear proportionality between the loss of electrophoretic mobility and the occupancy of the AuNP surface, implying a constant electrophoretic mobility loss for increasing amounts of protein. In reality, as it has been empirically observed[11,22,23], the electrophoretic mobility loss decreases as more protein is adsorbed to the surface of the AuNP. Despite this, the Langmuir adsorption model has seen extensive use to study protein adsorption phenomena.[57]

1.3 Protein corona

The previously mentioned characterisation of plasma protein profiles pertaining to healthy and diseased individuals is a continuing study which has been performed based on the adsorption of these proteins to specific surfaces – typically nanomaterials, such as nanoparticles – upon exposure to blood samples.[7,8,22,59] These protein-surface interactions rely on van der Waals forces as well as the contact between charged amino acids – which are hydrophilic and therefore located externally on the protein – and the charged surface; and can be of geometric, chemical and/or electrical nature.[52] Numerous factors pertaining to the proteins, the surface and the medium influence these interactions. For instance, larger proteins, more elongated, unstable or with higher unfolding rates possess a greater number of contact points in the same way more textured surfaces have a broader surface area.[52]

Moreover, the adsorption of proteins to a surface begins as a fast electrostatic binding, yet in time slow protein rearrangements can occur, ranging from orientation shifts (figure 1.11) to conformational alterations, in order to present the most contact points to the surface.[23]

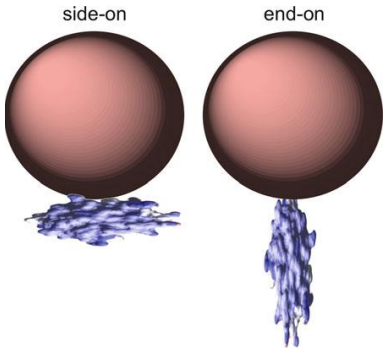

Figure 1.11. Possible orientations of a prolate ellipsoid protein bound to the surface of a spherical nanoparticle.[23]

Positively charged proteins adsorb more strongly to a negatively charged surface and vice-versa. However, lateral repulsions between proteins of identical charge can hinder further adsorption as more proteins accumulate at the surface. Because of this, protein-surface interactions are maximised at a pH closer to the pI of the protein, since its net surface charge is nearly neutral. This also points out to the importance of microenvironmental factors of the medium, such as pH.

Furthermore, proteins might also undergo conformational alterations in response to medium pH, temperature or ionic strength, as well as a consequence of being adsorbed to a surface, thus exposing different binding points to it. This can be influenced by the bulk protein concentration (figure 1.12) and greatly depends on the different stability constants.[52]

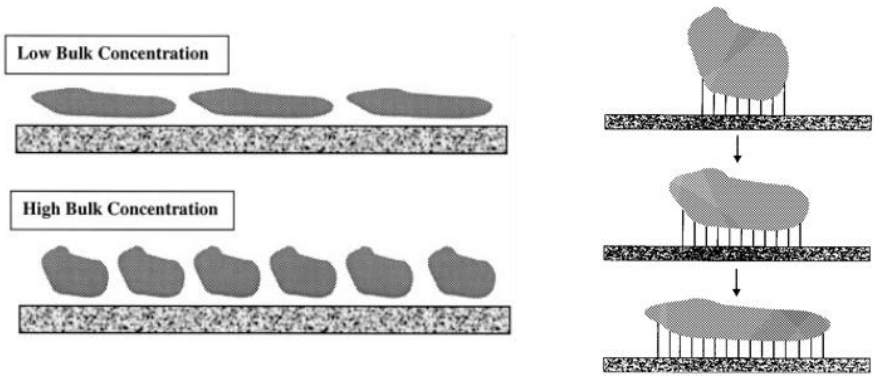

Figure 1.12. Proteins undergo conformational alterations depending on bulk protein concentration (left) or surface exposure time (right). Adapted from [52].

In a suspension, such as a blood sample, proteins are subject to diffusion, through which these come into contact with the surface. The diffusion rate can be described by equation 1.8:

$$\frac{\delta c}{\delta t} = D\frac{\delta^2 c}{\delta x^2} \qquad \text{Equation 1.8}$$

c is the protein concentration, *t* the time, *D* the diffusion coefficient and *x* the distance the protein travelled to reach the surface. Assuming short times and an equivalence between the rates of diffusion and of adsorption, this can be simplified to equation 1.9:

$$\frac{\mathrm{d}n}{\mathrm{d}t} = c_0\sqrt{\frac{D}{\pi t}} \qquad \text{Equation 1.9}$$

n is the protein concentration at the surface and c_0 the bulk protein concentration. This shows that the protein adsorption efficiency is directly proportional to its bulk concentration as well as the diffusion coefficient.

In fact, an interesting phenomenon has been documented whereby the composition of the protein coating of a surface exposed to a blood sample varies with time. The most abundant or smaller proteins – therefore with higher diffusion coefficients – adsorb first, only to be gradually replaced by others with greater affinity to the surface, which either exist in the plasma at a lower concentration, possess a lower diffusion coefficient, or both. This is known as the Vroman effect.[52,59,60] The rate at which the diffusing plasma proteins arrive at a surface can be derived from equation 1.9 and given as $c_0\sqrt{D}$ (table 1.2).[60]

Table 1.2. Rate of arrival of the twelve most abundant plasma proteins at a surface based exclusively on diffusion. Adapted from [60].

Protein	**c (μM)**	**D (10^{-7} cm^2s^{-1})**	$\boldsymbol{c_0\sqrt{D}}$
Albumin	600	6.1	1500
IgG	100	4.0	200
α_1-antitrypsin	40	5.2	91
Transferrin	30	5.0	67
α_2-haptoglobins	20	4.7	43
IgA	18	4.6	39
HDL	15	4.0	30
Complement 3	9	4.5	19
Fibrinogen	7.5	2.0	11
α_2-macroglobulin	3.3	2.4	5
LDL	2	2.0	3
IgM	1	2.6	1.6

Nanoparticles of various compositions and shapes have seen extensive use as surfaces onto which plasma proteins adsorb for subsequent profiling[7,8,61,62], the most common shape being the sphere, since it is easier to synthesise and possesses an isotropic surface charge distribution[63,64]. The protein coating enveloping these spherical nanostructures is denominated the protein corona, which behaves much like the previously discussed EDL and is divided into two layers: the hard corona and the soft corona (figure 1.13). The hard corona corresponds to the innermost monolayer, composed of proteins with the highest affinity to the nanoparticle over the exposure time, as per the Vroman effect, which bind directly to the surface of the nanoparticle. Protein exchange rates with the immediate microenvironment are minimal at this layer and adsorption is practically irreversible, as proteins are displaced exclusively by others of higher affinity. The soft corona, on the other hand, designates the collective outer layers, which establish protein-protein interactions with the hard corona as well as mutually, thus making the soft corona more loosely adsorbed, so much that mechanical methods such as centrifugation are typically used to separate it from the nanoparticle-protein complex. At this layer, protein adsorption is reversible and the exchange rates are comparatively much higher.[7,8,24,59,61,62,65]

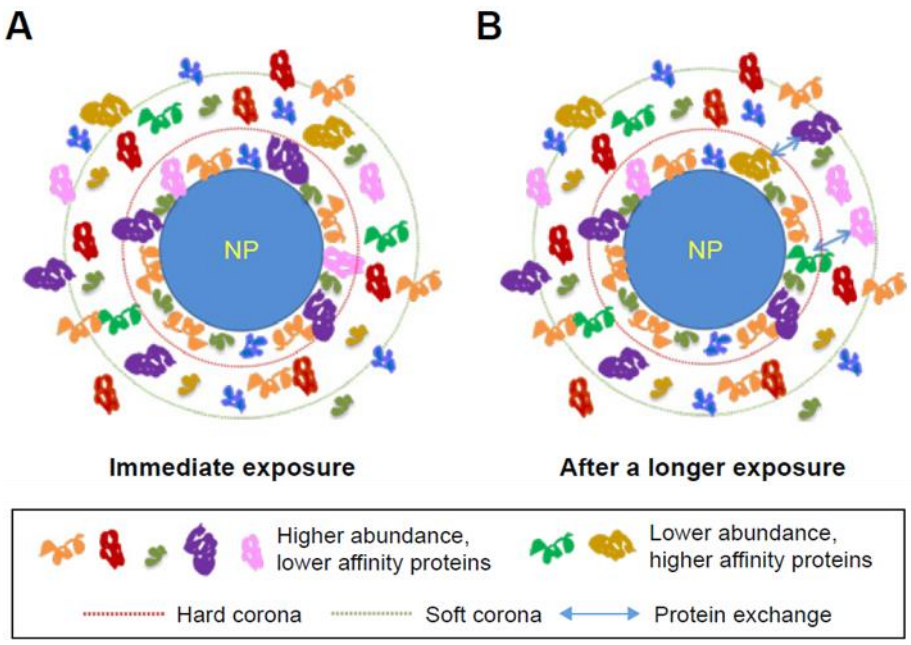

Figure 1.13. Composition of a protein corona formed on a spherical nanoparticle upon exposure to blood (A) and after some exposure time (B). Adapted from [59].

Previous studies[7,8] have exploited the protein corona and successfully demonstrated a correlation between individual protein coronas profiles and specific diseases (figures 1.14 and 1.15).

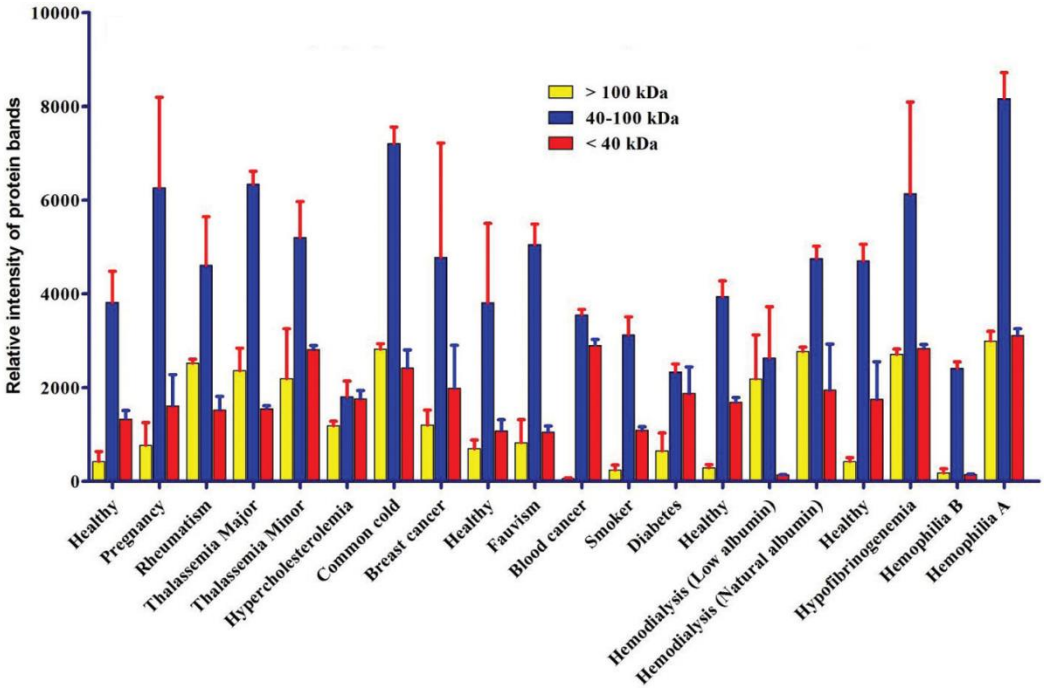

Figure 1.14. Relative intensity of silver stained SDS-PAGE protein bands pertaining to polystyrene nanoparticles incubated with plasma (50%) from different patients. Adapted from [7].

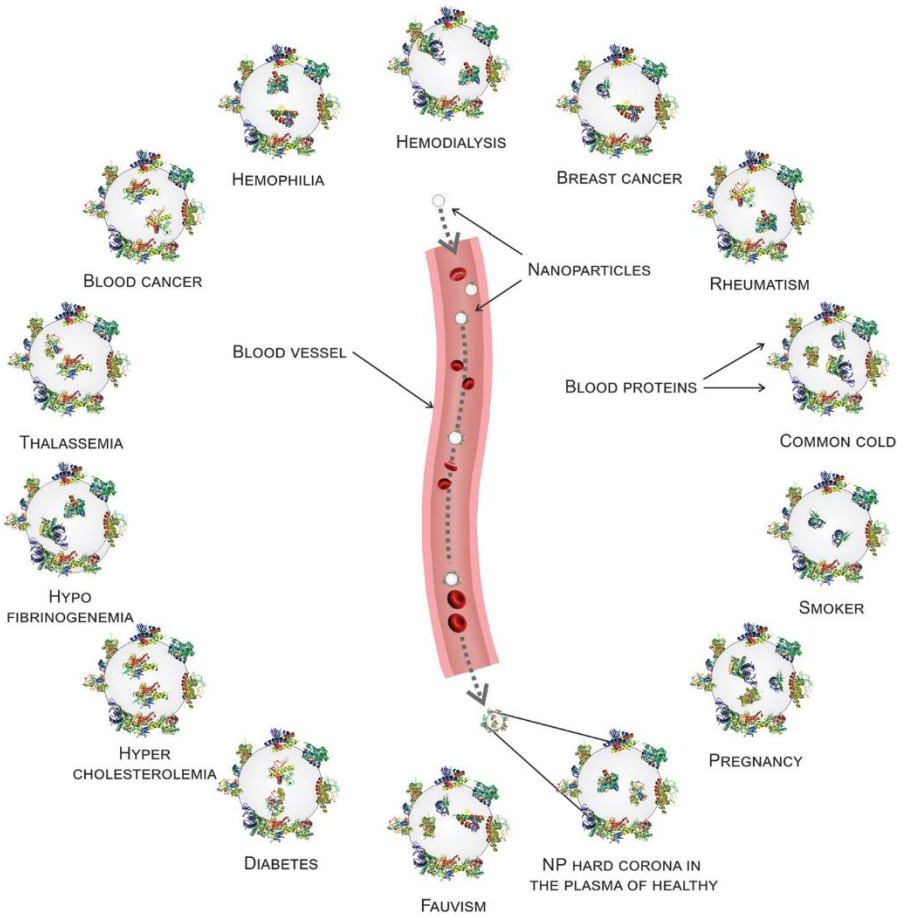

Figure 1.15. Different protein hard coronas are formed on nanoparticles exposed to a blood sample depending on several diseases or medical conditions.[7]

1.4 Toxicology concerns

As AuNP can potentially be employed in various *in vivo* nanomedical applications in the future, some considerations must be addressed, namely the health risks. Despite virtually no cytotoxicity being reported for these nanoparticles, the long-term effects of exposure are still being evaluated. The protein corona formed through the conjugation of plasma proteins with AuNP introduced into the bloodstream enhances biocompatibility and dissimulates the nanoparticles to leukocytes and macrophages, avoiding an immune response for a time. Yet, depending on the protein corona composition, an immune response can be suppressed just as well as it can be triggered. Moreover, previous studies have determined AuNP larger than 40 nm in diameter are extremely prone to opsonisation, becoming marked for phagocytosis. Conversely, AuNP of smaller sizes also present higher colloidal stability, albeit having a poorer protein coating, hence the maximum AuNP diameter utilised in this work was 40 nm.[25,66–68]

2 Objectives

The application of gold nanoparticles in theragnostics, despite promising, must yet undergo further study in order to assess possible health risks and fully understand the mechanics behind the interactions between these nanoparticles and biomolecules, allowing for the design of novel biomedical techniques. The approach herein presented describes the implementation of spherical gold nanoparticles as probing matrixes onto which blood plasma proteins adsorb once exposed to a blood sample, functioning *in vivo* just as well as *ex vivo* – thus eliminating the health risks – and based on the premise that diseases cause fluctuations on plasma protein gradients, as already determined in previous studies. These gradients are unique for each disease and, as such, translate into unique plasma protein coronas formed on the surface of gold nanoparticles, the characterisation of which is key to profile specific protein coronas associated to the respective diseases and states thereof. However, before a comprehensive protein corona profiling can be elaborated, the adsorption mechanism of each plasma protein to gold nanoparticles must first be better understood.

This is a continuing work which has been previously performed on two important plasma proteins, serum albumin and fibrinogen, both of bovine origin. In the present work, these proteins were compared to the respective human counterparts, either sequentially, structurally and in the empirical evaluation of the conjugates formed with gold nanoparticles, considering the ultimate purpose is the design of a novel technique for the diagnosis of human diseases.

The colloidal stability of gold nanoparticle conjugates with each studied protein relative to the bare nanoparticles was compared under different ionic strength and pH conditions.

Conformational alterations of proteins adsorbed to the surface of gold nanoparticles were evaluated through circular dichroism spectroscopy.

The protein corona was studied through a comparative measurement of the hydrodynamic diameter of the soft and hard coronas formed of each studied protein on gold nanoparticles of two different sizes, using dynamic light scattering.

The molar ratio of each studied protein to a gold nanoparticle necessary to completely cover it was determined by agarose gel electrophoresis, in which conjugation curves could be visualised and through which the binding constants for each protein could be estimated.

3 Methods

All reagents and instruments are documented in Appendix II.

3.1 Synthesis of spherical gold nanoparticles

All glassware utilised throughout the experiments to contain AuNP and AuNP conjugates was previously washed with *aqua regia* – a mixture of nitric acid (HNO_3) and hydrochloric acid (HCl) in a molar ratio of 3:1, respectively – which quickly dissolves any metallic residue, following successive rinses with Milli-Q water (18.2 MΩ·cm at 25 °C) until a pH of 7.0, as measured with pH test strips.

The synthesis of spherical AuNP was achieved through the method first described by Turkevich et al.[69], with some minor modifications by Kimling et al.[70], in which sodium citrate tribasic dihydrate ($Na_3C_6H_5O_7 \cdot 2H_2O$) acts as both a reducing agent to chloroauric acid ($HAuCl_4$), thus generating the Au^0 atoms required for nucleation; and a primary capping agent to control nanoparticle growth and impede contact-induced aggregation. Chloroauric acid was added to a boiling sodium citrate solution, following the "reverse method" discussed by Ojea-Jiménez et al.[41], as it has been demonstrated to yield much less polydisperse AuNP. This reaction occurred in a round bottom flask under constant heating, magnetic stirring and reflux, as to avoid losing volume by evaporation, with subsequent concentration changes.

3.1.1 Synthesis of spherical gold nanoparticles with ca. 15 nm diameter

98 mL of Milli-Q water were heated until boiling, after which 2 mL of sodium citrate (343 mM) were added. After 5 minutes, 69.2 µL of chloroauric acid (1.42 M) were added. It is at this stage that the solution acquires an immediate dark colour, which gradually subsides to dark red. After another 5 minutes, the reaction was stopped, heating, stirring and reflux turned off; and the colloidal suspension was cooled to room temperature (25 ºC) for a few hours, before filtering through a disk filter (0.20 µm pore size) adapted to a syringe. This filtration step is to remove large aggregates in the obtained colloidal suspension and maintain polydispersity as low as possible. This method has yielded spherical AuNP of 10-15 nm in diameter, as determined by a method developed by Haiss et al.[71] (see below in section 3.2).

3.1.2 Synthesis of spherical gold nanoparticles with ca. 40 nm diameter

This protocol was based on the one kindly provided by Miguel Peixoto de Almeida, PhD, from Prof. Eulália Pereira's research group at LAQV, REQUIMTE, Faculdade de Ciências, Universidade do Porto, Portugal. 150 mL of sodium citrate (2.2 mM) were heated until boiling, with 1 mL of a 25 mM chloroauric acid solution added thereafter. After 10 minutes, the reaction was cooled to 90 ºC and 1 mL of the 25 mM chloroauric acid solution was added to the gold seeds; and again after 30 minutes. After another 30 minutes, the reaction was stopped and proceeded similarly to the method described above, for the synthesis of smaller AuNP. This method has yielded spherical AuNP of 40-45 nm in diameter, as determined by a method developed by Haiss et al.[71] (see below in section 3.2).

All colloidal suspensions of AuNP were stored in glass recipients covered with aluminium foil, in order to avoid light exposure which may induce nanoparticle aggregation; and kept at 4º C until used. pH of the as-synthesised solutions was 6.5. Note that AuNP-citrate become increasingly unstable with more acidic pH (< 7)[72], reaching a maximum point of aggregation at a pH of approximately 3.[73] This is due to citrate becoming completely protonated at lower pH, therefore reducing the number of negative surface charges, which promotes the attraction forces amongst AuNP.[72]

3.2 Gold nanoparticle characterisation

Through an empirical UV-Vis spectroscopy method discussed by Haiss et al.[71], it was possible to calculate the diameter and concentration of spherical AuNP-citrate utilising the LSPR effect and the molar extinction coefficient, respectively. This method cannot be applied to spherical AuNP larger than 100 nm or smaller than 2 nm in diameter, or to non-spherical AuNP or functionalized with other capping agents.

Triplicate UV-Vis spectra in a 750-350 nm wavelength range were taken from 1:2 dilutions of the AuNP-citrate colloidal suspension.

To estimate the diameter of the AuNP with an expected size of < 35 nm, the absorbance at the LSPR peak (A_{LSPR}) and at 450 nm ($A_{450\ nm}$) were required for the following equation:

$$\varnothing = \exp\left(\frac{\frac{A_{LSPR}}{A_{450\ nm}} - b}{m}\right) \qquad \text{Equation 3.1}$$

m and *b* represent the slope and intercept, respectively, of the equation fitted to the plotted tabular values of the $A_{LSPR}/A_{450\ nm}$ ratio against the respective AuNP diameter, in nm, presented by Haiss et al.[71] (Appendix III).

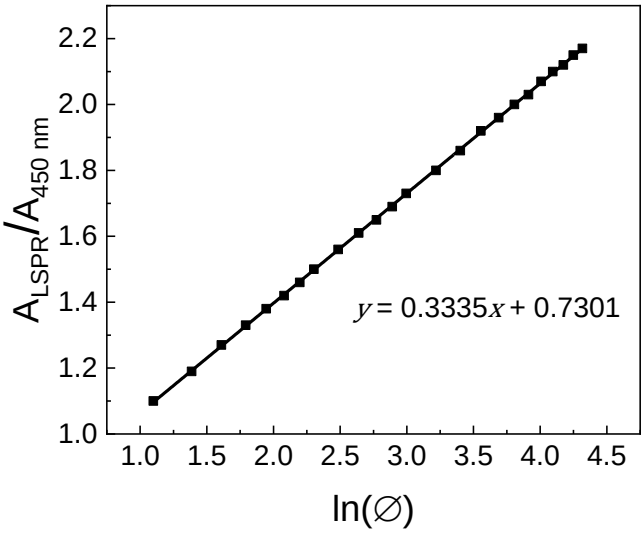

Figure 3.1. The ratio of the absorbance at the LSPR peak to the absorbance at 450 nm in dependence of the natural logarithm of AuNP diameter, in nm, can be fitted to the linear equation shown above, with an $R^2 > 0.999$.

For AuNP with an expected size of > 35 nm, a different equation was used, which requires only the wavelength at the LSPR peak:

$$\varnothing = \frac{\ln\left(\frac{\lambda_{LSPR} - 512}{6.53}\right)}{0.0216} \qquad \text{Equation 3.2}$$

Once the AuNP diameter was known, the concentration was estimated through the Beer-Lambert law by correlating the absorbance at 450 nm with the respective molar extinction coefficient (the value of which corresponds to a specific diameter, see Appendix II):

$$A_{450\ nm} = \varepsilon_{450\ nm} l c \qquad \text{Equation 3.3}$$

ε is the molar extinction coefficient ($M^{-1}\ cm^{-1}$), l the optical path (cm) and c the concentration of the diluted AuNP colloidal suspension (M), which were then multiplied by the dilution factor (1:2).

3.3 Gold nanoparticle functionalization

AuNP-citrate were functionalized with 11-mercaptoundecanoic acid (MUA) – a thiol-containing molecule which replaces the electrostatically bound citrate from the surface of AuNP, imparting these with a negative surface charge and a much higher colloidal stability. In fact, samples of AuNP-citrate tend to aggregate irreversibly after centrifugation, even at low speeds, or in agarose gel electrophoretic assays.

A stable solution of MUA 0.01 M was prepared by solubilising 21.8 mg of MUA in 10 mL absolute ethanol (HPLC grade).

The colloidal suspensions of AuNP-citrate were diluted in Milli-Q water to the intended final concentration of the AuNP-MUA stock solution. Basic water should be avoided, as it tends to induce irreversible AuNP aggregation due to the ionic strength imparted by the salt used to basify the water.

A volume of the MUA 0.01 M solution was added to the AuNP-citrate colloidal suspension for a MUA:AuNP molar ratio experimentally determined to be sufficient for a full coverage of the surface of AuNP (5000:1 for the ca. 15 nm AuNP and 15000:1 for the ca. 40 nm AuNP), under magnetic stirring for 15 minutes, after which it was incubated overnight at room temperature, thus ensuring a complete MUA monolayer formation. Any excess, unbound MUA was removed through centrifugation (9520 g for 10 minutes). AuNP concentrations greater than 5 nM have been observed to possess a high tendency to aggregate from the centrifugation, most probably due to the greater steric proximity amongst AuNP in the resulting pellet. A successful functionalization can be assessed by UV-Vis spectroscopy, in which the absorbance in the 750-600 nm wavelength range – a region in which high absorbance indicates the presence of aggregates – should be as low as possible, whilst a slight redshift (≈ 5 nm) of the LSPR peak, compared to the AuNP-citrate spectra, should be observed.

3.4 Protein preparation

All studied proteins were solubilised in potassium phosphate buffer 5 mM, pH 7.4. This apparently low ionic strength is just enough to ensure protein solubilisation and stability, whilst avoiding AuNP aggregation induced by ionic strength. This buffer was prepared by dilution in Milli-Q water of a stock 1 M solution previously prepared for the physiological pH (7.4) through the Henderson-Hasselbalch equation:

$$pH = pK_a + \log_{10}\left(\frac{[salt]}{[acid]}\right) \qquad \text{Equation 3.4}$$

Solutions of bovine and human serum albumins were prepared for a concentration of 1.0 mg/mL, by weighting 10 mg of each protein and adding 10 mL of potassium phosphate buffer.

Bovine and human plasma fibrinogen solutions were prepared for a concentration of 0.5 mg/mL, since these proteins become more difficult to solubilise and prone to coagulate at higher concentrations, by weighting 5 mg of each and adding to 10 mL of potassium phosphate buffer.

The concentration of all studied proteins was determined by bicinchoninic acid (BCA) assays, in which a calibration curve of absorbance versus protein concentration was obtained from dilutions of a BSA standard at 1.0 mg/mL in Milli-Q water (1.0 to 0 mg/mL in intervals of 0.2 mg/mL). A BCA and copper (II) sulphate mixture in a 49:1 molar ratio (known as the "working reagent", which has a green colour) was added in aliquots of 475 µL to 25 µL of the BSA standard dilutions and triplicates of each sample in microcentrifuge tubes. All tubes were immediately placed in a heat block to incubate at 37 ºC for 30 minutes. In the presence of peptide bonds, Cu^{2+} is reduced to Cu^{+}, which forms a purple coloured complex with BCA, with a maximum absorbance band at 562 nm with a colour intensity proportional to the concentration of protein present.[74]

3.5 Gold nanoparticle-protein conjugation

AuNP-protein conjugates were prepared by adding to the AuNP-MUA colloidal suspensions the required amount of a protein for the intended protein:AuNP molar ratios, as per the following equation:

$$V_p = \frac{c_n V_n x}{c_p} \qquad \text{Equation 3.5}$$

V_p and c_p represent the protein volume and concentration, respectively; V_n and c_n the AuNP-MUA colloidal suspension volume and concentration, respectively; and x the protein:AuNP molar ratio. Once the protein was added, samples were shaken at 300 RPM during 15 minutes in order to uniformize the protein distribution, followed by an incubation at 4 ºC period. For both serum albumins, incubation was overnight, thus ensuring the adsorption process reached the thermodynamic equilibrium. However, for both fibrinogens, this period was reduced to a minimum of 2 hours, since conjugates with these proteins were more unstable and the AuNP were observed to begin aggregating after approximately 6 hours after adding the fibrinogen.

The protein:AuNP molar ratios necessary for each different assay performed in the present work were varied and are indicated in the corresponding sections pertaining to the results and discussion.

For the colloidal stability assays or studies involving the protein corona, conjugates samples were centrifuged at 9520 *g* for 10 minutes, which removes the loosely bound outer protein layers collectively known as the soft corona.[59,61] Additionally, in the agarose gel electrophoretic assays, centrifugation was employed to concentrate the samples prior to loading into the gels, in order to have visible bands. Note that centrifugation tends to induce the aggregation of AuNP-fibrinogen conjugates, since these proteins coagulate from steric proximity in the pellet.

3.6 Molecular visualisation

The PDB files 3V03 (BSA), 1AO6 (HSA), 1DEQ (BPF) and 3GHG (HPF) were utilised for the calculation of electrostatic surface potential and solvent accessibility using various software, rendering three-dimensional simulated protein surface projections onto which regions of different surface charges or accessibility to specific solvent molecules, respectively, were mapped in different colour gradients, thus providing invaluable insight on the structural behaviour of these proteins when interacting with the negatively charged AuNP.

In order to calculate the electrostatic surface potential, the PDB files were first converted to PQR files, in which the temperature and occupancy columns are replaced with information regarding partial charge (Q) and electrostatic radius (R) for each atom; through the PDB2PQR (version 2.1.1) web server (http://nbcr-222.ucsd.edu/pdb2pqr_2.1.1/), using the PARSE force field and the PROPKA (version 3.1) web server (hosted at the PDB2PQR web site) to predict residue pKa and whole protein pI based on the three-dimensional structure and assign protonation states at any given medium pH. Amongst the output PQR files generated, an APBS input file was opened with the PyMOL software (version 2.3.2) through its built-in APBS plug-in, which applies the Poisson-Boltzmann equation to calculate the electrostatic interactions in the provided molecule and colours regions of its three-dimensional simulated surface projection in accordance to the charge distribution (red is more negative; blue is more positive).[75]

For the solvent accessibility visualisation, the PDB files were opened with the Swiss PDB Viewer software (version 4.1.0), which evaluates the accessibility of each residue to a specific solvent molecule and colours these differentially (red is more accessible; blue is less accessible).

3.7 UV-Vis spectroscopy

All UV-Vis measurements were acquired with a Varian Cary 50 Bio UV-Vis spectrophotometer for a 750-350 nm wavelength range at 600 nm/min and at room temperature (25 ºC), with samples prepared in triplicates and placed in a Hellma quartz cuvette of 10 mm path length.

For studies of colloidal stability with varying ionic strength, all samples were prepared with different concentrations of NaCl (0 to 100 mM in intervals of 10 mM, then 100 to 500 mM in intervals of 100 mM) to a final volume of 500 µL and incubated for 30 minutes prior to measurement, which was the time necessary for the aggregation effect to stabilise, as determined by David Peitinho, MSc[22].

The colloidal stability assays with pH variation were performed in a pH range of 2.0 to 8.0 in intervals of 0.5, with pH being adjusted with solutions of HCl 0.1 M and NaOH 0.1 M and measured with a Crison pH meter Basic 20+.

3.8 Circular dichroism spectroscopy

CD studies were conducted on samples containing a protein concentration of 0.05 mg/mL, using a Hellma quartz cuvette of 1 mm path length, which was cleaned between measurements with a mixture of 30% HCl and 70% ethanol and thoroughly rinsed with ethanol before being blown dry with nitrogen. Before beginning data acquisition, a no cell baseline was performed, followed by a blank baseline only with potassium phosphate buffer 5 mM, pH = 7.4. Triplicate CD spectra were acquired from a Chirascan qCD spectrometer for a 260-195 nm wavelength range at 20 nm/min and at room temperature (25 ºC). Data was analysed using the BeStSel (Beta Structure Selection) web server.

3.9 Dynamic light scattering

DLS samples were prepared to a AuNP concentration of 2 nM and placed in Sarstedt PMMS cuvettes of four openings. Data was acquired from a HORIBA SZ-100 nanopartica analyser, equipped with a 532 nm green laser, in triplicate measurements of 30 seconds each and with the detection angle set to 90º. The instrument software automatically handled hydrodynamic diameter calculations through the Stokes-Einstein equation, with results expressed based on scattered light intensity.[51]

3.10 Gel electrophoresis

All electrophoretic assays were performed with a Bio-Rad PowerPac Basic Power Supply, which automatically modulates the current intensity in order to maintain constant the voltage.

3.10.1 SDS-PAGE

A “stacking gel” (4% acrylamide) and a “resolving gel” (12% acrylamide) were hand casted as per the following table:

Table 3.1. Table of reagents for the preparation of a stacking gel (4%) and a resolving gel (12%), according to the protocol for SDS-PAGE by Bio-Rad Laboratories, Inc.

Reagents	Stacking gel (4%)	Resolving gel (12%)
30% Acrylamide/Bis	1.98 mL	6.00 mL
0.5 M Tris-HCl, pH = 6.8	3.78 mL	-
1.5 M Tris-HCl, pH = 8.8	-	3.75 mL
10% SDS	150 µL	150 µL
Milli-Q H_2O	9.00 mL	5.03 mL
TEMED	15 µL	7.5 µL
10% APS	75 µL	75 µL
Total volume	15 mL	15 mL

The two final reagents listed, tetramethylethylenediamine (TEMED) and ammonium persulfate (APS), trigger the polymerisation reaction, hence these were added last and immediately before casting the gels, with the resolving gel being placed first in the glass cast and left to polymerise for 1 hour, after which the stacking gel was added on top of the former and left to polymerise for another hour, with the resulting interface between both gels being important for an increased band resolution in the resolving gel, as the samples concentrate here, after quickly descending the high-porosity stacking gel.

The glass cast with both gels encased was then inserted into a Bio-Rad Mini-PROTEAN Tetra Electrode Assembly, which was subsequently placed inside a Bio-Rad Mini-PROTEAN Tetra Vertical Electrophoresis Cell. The former was entirely filled with "running buffer" (0.192 M glycine, 0.025 M Tris and 0.1% SDS), whilst the latter was only filled to the marked level.

All protein samples and marker solution (Bio-Rad Unstained Low Range SDS-PAGE Standard) were submitted to a denaturing treatment through both a chemical and a physical process, in which to 20 µL of the former and 3 µL of the latter were added 10 and 5 µL, respectively, of a "sample buffer" (1% (w/v) bromophenol blue, 10% (w/v) SDS, 10% (v/v) glycerol 87%, 0.5 M Tris-HCl, pH = 6.8; and 715 mM β-mercaptoethanol, which is a denaturing agent and should be added immediately prior to use) and an additional 2 µL of Milli-Q water to the latter, before placing samples and marker in a water bath at 100 ºC for 10 minutes and subsequently centrifuging these at 13000 g for 2 minutes.

15 µL of each protein sample and 3µL of marker solution were loaded into the stacking gel and the power supply was set to apply 150 V for 1 hour, until the sample buffer blue line reached near the opposite extremity of the resolving gel, after which both gels were removed from the glass cast whilst submerged in Milli-Q water and placed in a plastic container filled with a "staining solution" (10% (v/v) glacial acetic acid, 2% (w/v) Coomassie Brilliant Blue R-250 Dye and 35% methanol) overnight and then rinsed in successive cycles with a "distaining solution" (50% (v/v) absolute ethanol and 10% (v/v) glacial acetic acid) until the bands could be discerned from the background.

3.10.2 Agarose gel electrophoresis

All AGE assays were conducted on 0.5% (w/v) agarose gels, which were prepared by weighting 0.225 g of agarose and solubilising it in 45 mL of a 1:400 dilution of a stock TAE buffer (24.2% (w/v) Tris, 5.71% (v/v) glacial acetic acid and 10% (v/v) 0.5 M EDTA) under constant heating and magnetic stirring, after which it was cooled down at room temperature (25 ºC) for approximately 15 minutes and placed in the cast. Note that it is important to allow the heated agarose solution to cool down for some time before the gelation reaction begins, as pouring it too hot on the cast can damage it. Once solid, the cast was inserted into a Bio-Rad Mini-Sub Cell GT, which was filled with the 1:400 dilution of stock TAE buffer to the marked level. Note that the high dilution factor of the TAE buffer was to minimise the risk of ionic-strength-induced aggregation of AuNP in the samples; however, this also increases the electrical resistance and, consequently, temperature, causing anomalies in the gel, which was subsided by having the agarose gel and TAE buffer cooled down to 4 ºC prior to use.

AuNP-protein conjugates samples for AGE were prepared with an initial AuNP concentration of 1-2 nM for the smaller AuNP and 0.1 nM for the larger ones, to which the amount of protein required for the intended molar ratios was added, followed by a conjugation procedure as described above, after which all samples were centrifuged at 9520 *g* for 10 minutes, the supernatant discarded and the pellets resuspended in 13.5 µL potassium phosphate buffer 5 mM, pH = 7.4 and 1.5 µL glycerol immediately before loading into the agarose gel. Alternatively, the pellets can be resuspended in 15 µL of potassium phosphate buffer 5 mM, pH = 7.4; as AuNP are dense enough to deposit in the wells without glycerol.

15 µL of each sample were loaded into the agarose gel and the power supply was set to apply 150 V (E = 1042 V/m) for 20-30 minutes, depending on the assay performed, after which the gel was removed from the cast to be photographed.

3.10.3 Gel image analysis

Digital electrophoresis gel images were processed in the free and open source software, eReuss (version 0.01) (https://github.com/lkrippahl/eReuss), created and developed by Prof. Ludwig Krippahl, which requires Python 2.7 and the libraries Scipy, Numpy, Scikit-image and Matplotlib, all included in the Anaconda package distributed by Continuum Analytics (https://www.anaconda.com/distribution/).

Upon initiating the eReuss server, a loop-back address was opened on a web browser by typing 127.0.0.1:8081 on the address bar, which connects to the eReuss server running on the background and provides a graphical user interface to the software.

The electrophoresis gel image to be processed was uploaded in the first page and then prepared for automated analysis in the following pages (note that, as of version 0.01, eReuss only recognises gel images oriented vertically, with band migration from top to bottom; and does not have a rotation option, hence all images were rotated, if necessary, externally and prior to upload).

In “Image preprocessing”, the band colour was specified on the respective drop-down list (red for AGE AuNP conjugates samples and blue for Coomassie-stained SDS-PAGE), which allows eReuss to ignore that RGB channel in the background, thus improving contrast between the gel and the bands. Additionally, the colours were inverted so that the bands appeared bright on a dark background, as the software measures band colour intensity by pixel brightness.

In “Clipping”, all gel dimensions (comb length, in cm, measured between the beginnings of the first and last teeth; number of comb teeth and number of used wells only) were inserted in the respective boxes, which eReuss uses to calculate band migration distances through a pixel to centimetre conversion and to establish the number of lanes to be processed. Moreover, a region of interest (ROI) for the image was defined, as shown in figure 3.2.

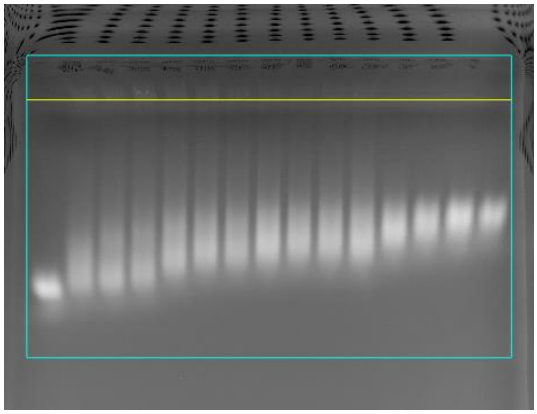

Figure 3.2. Delimitation of the ROI in an agarose gel containing AuNP conjugates samples with the cyan rectangle outline and a yellow horizontal line placed above the wells, which marks the starting point of migration.

In “Lane identification”, eReuss automatically assigned the band colour intensity profiles to the established vertical lanes for each band (note that a manual tuning of this alignment is possible in this page, if necessary), generating the graph in figure 3.

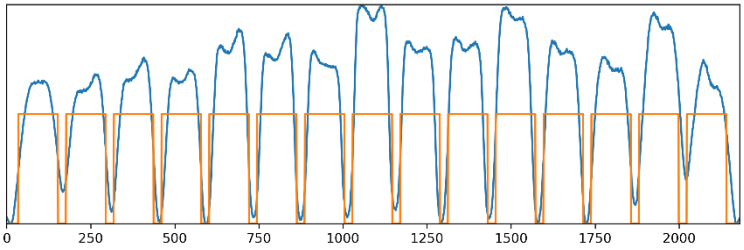

Figure 3.3. In the lane identification graph, the band colour intensity profiles (in blue) are aligned with the lanes the software recognised (in yellow, where the gaps represent the spaces between each lane).

In “Profiling”, eReuss measures the colour intensity profile in each lane and identifies the peaks by iteratively fitting a Gaussian distribution to the maximum value in each curve and subtracting that distribution repeatedly until either the set number of Gaussians was reached or the maximum value falls below the set minimum height, which is the percentage of the image brightness range. These parameters, along with smoothing the lane profiles and the polynomial degree for the baseline, were left at default values, although manual tuning was possible, if necessary.

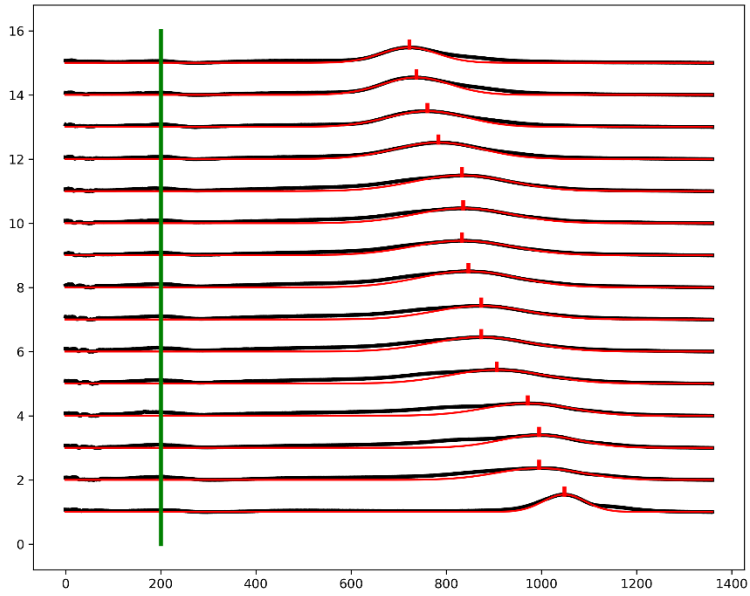

Figure 3.4. Rendering of a band migration profile graph, where the green vertical line marks the start of migration (where the wells are located) and the black horizontal plots represent the migration profile for each lane, with the overlaying red lines fitting Gaussian curves at the colour intensity peak position (also marked in red) of each band.

In "Final report", results were summarised and a ZIP file exported, containing the PNG files of the pre-processed and clipped gel image and the band migration profile graph, an XML file of detailed data on band migration profiles and a CSV file in which a table of peak positions, heights and areas, in centimetres, can be found.

With the migration distance of each band and knowing the electric potential difference and run time, it was possible to calculate the electrophoretic mobility (μ; $m^2V^{-1}s^{-1}$) of each sample. For the AGE assays, since the band mobility decreased as the protein:AuNP molar ratio increased, the electrophoretic mobility difference between the unconjugated and each of the conjugated samples was plotted against the protein concentration (using the OriginPro 2018 software), resulting in a curve which could be fitted to a Hill-Langmuir equation:

$$\Delta\mu = \Delta\mu_{max}\frac{c^n}{\left(\frac{1}{K_a}\right)^n + c^n} \qquad \text{Equation 3.6}$$

$\Delta\mu$ is the electrophoretic mobility difference, $\Delta\mu_{max}$ the maximum value it tends to, c the initial protein concentration, n the Hill coefficient and K_a the binding constant. The Hill coefficient designates the binding cooperativity, which is negative if $n < 1$, positive if $n > 1$ or uncooperative if $n = 1$, the latter being formally equivalent to the Langmuir adsorption model. The binding constant is the inverse of the dissociation constant, K_d, or the protein concentration at which half of all AuNP have protein adsorbed to its surface.

4 Results and discussion

4.1 Gold nanoparticles – from synthesis to conjugation

In the inverse Turkevich method, quality assessment during AuNP synthesis was performed by naked eye observation of successive colour changes in the boiling sodium citrate solution upon adding the chloroauric acid, which starts yellow from the latter and immediately becomes colourless as a consequence of being reduced to Au^0 by the sodium citrate, initiating nucleation and from which AuNP growth ensues, indicated by a quick change to a dark colour, gradually stabilising to dark red.

Figure 4.1. 13 nm AuNP-citrate colloidal suspension diluted to 10 nM from the as-synthesised concentration of 11 nM.

Once the reaction was stopped and the AuNP-citrate colloidal suspension was cooled down and subsequently filtered in order to remove larger formations and ensure a low polydispersity, triplicate samples were taken for UV-Vis spectroscopy characterisation of diameter and concentration.

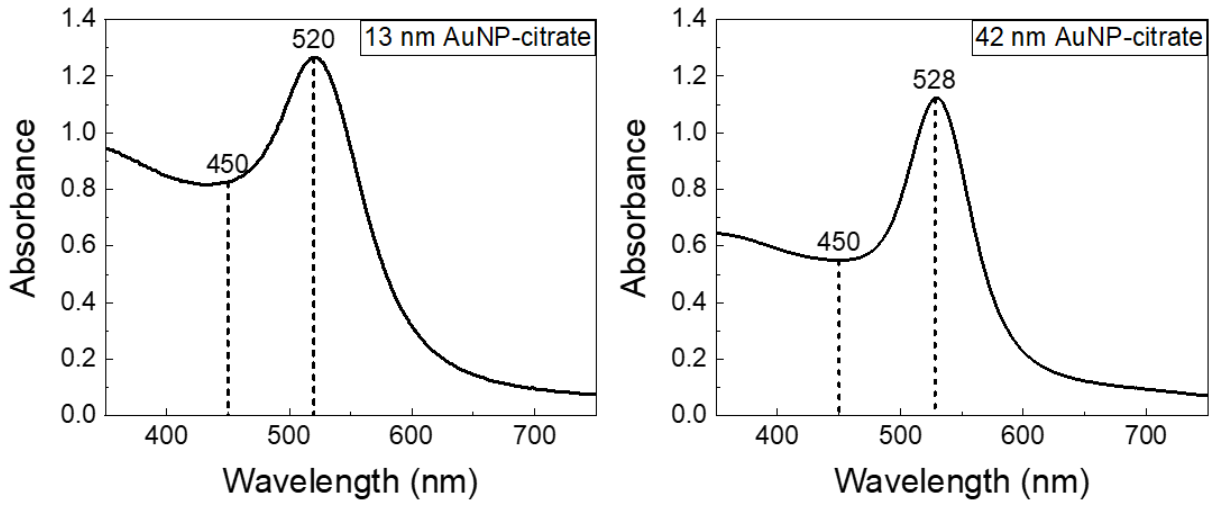

Figure 4.2. UV-Vis absorbance spectra of 1:2 dilutions of 13 nm and 42 nm AuNP-citrate. For AuNP with ca. 13 nm in diameter (left panel), the absorbance values at 450 nm and at the LSPR peak, 520 nm are used to calculate the diameter of AuNP and concentration of the AuNP colloidal suspension. For AuNP with ca. 42 nm in diameter (right panel), this calculation requires the absorbance value at 450 nm and the value of the wavelength at the LSPR peak, 528 nm.

The method used for the synthesis of smaller AuNP yielded diameters of 10-15 nm in different synthesis, with low polydispersity for each lot; and concentrations of 7-21 nM, inversely proportional to the diameter, since larger AuNP take up more Au^0 atoms, thus reducing the overall number of AuNP. Likewise, the method used for the synthesis of larger AuNP yielded diameters of 40-45 nm in different synthesis, with low polydispersity for each lot; and concentrations of 0.1-0.5 nM, inversely proportional to the diameter. The discrepancy between the concentrations obtained for smaller and larger AuNP can also be explained by the aforementioned fact.

Table 4.1. Diameter and concentration calculated for AuNP synthesised in the present work.

Diameter (nm)	**Concentration (nM)**
12.10	13.76
13.02	11.18
14.78	6.80
15.56	4.60
41.66	0.22

Post-synthesis quality assessment could be observed from the single peak in the UV-Vis spectra, whose narrow width indicates low polydispersity and the low absorbance at 750-600 nm the absence of extensive AuNP aggregation.

The LSPR peak suffers a red-shift with the increase of particle size, hence the 8 nm difference between the UV-Vis spectra for 13 and 42 nm AuNP. Because of this reason, a red-shift also occurs as AuNP aggregate, which can be exploited to detect the formation of aggregates.

A slight red-shift can indicate functionalization success with a larger capping agent molecule, such as MUA, or conjugation success with protein, all of which contribute to a different refractive index at the surface of the AuNP.

In order to determine the amount of MUA necessary to cover the entire surface of AuNP, an AGE assay was performed for each AuNP size with increasing MUA:AuNP molar ratios. Due to possible interactions between citrate and agarose, which would leave the AuNP uncovered to aggregate, an insufficient amount of MUA can be observed by the formation of aggregates in the wells and smearing along the gel (figures 4.3 and 4.4).

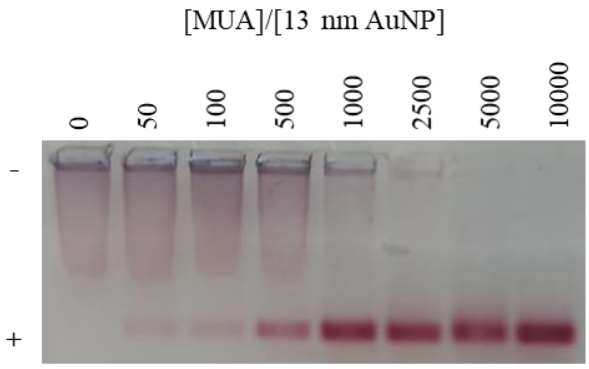

Figure 4.3. Agarose gel (0.5%) electrophoresis of 13 nm AuNP-citrate with increasing MUA:AuNP ratios.

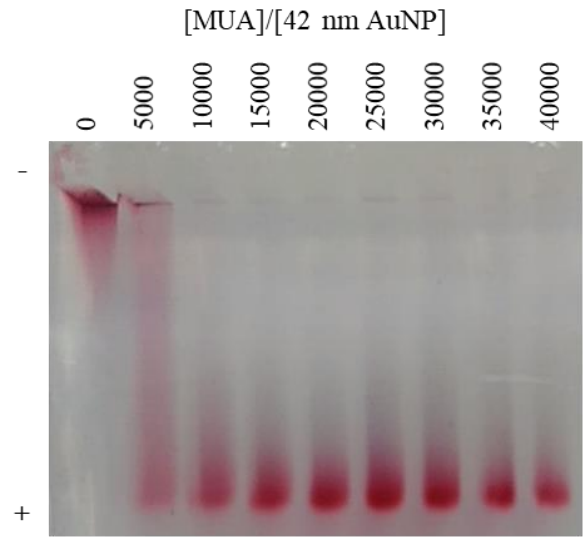

Figure 4.4. Agarose gel (0.5%) electrophoresis of 42 nm AuNP-citrate with increasing MUA:AuNP ratios.

From these results, the MUA:AuNP molar ratios of 5000 and 15000 for AuNP of 13 and 42 nm, respectively, were selected as the ideal amounts of MUA at which no aggregates were detected in the wells and band smearing was minimum.

After the functionalization procedure, any excess MUA was removed through centrifugation. In order to validate functionalization success, with absent signs of aggregation, triplicate samples were taken for UV-Vis spectra comparison with the respective AuNP-citrate samples (figure 4.5).

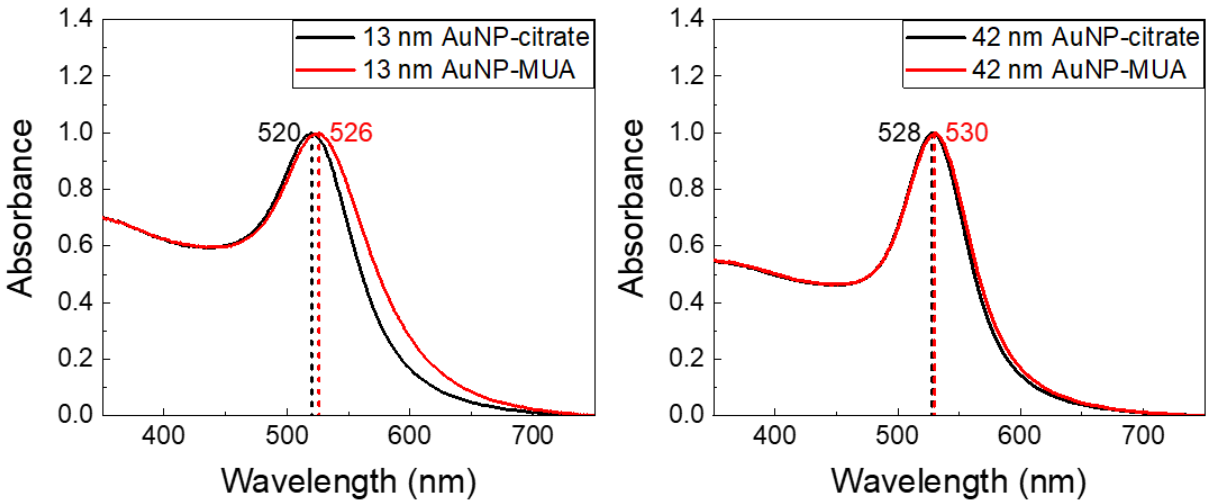

Figure 4.5. Comparison between the normalized UV-Vis absorbance spectra of unfunctionalized AuNP, in black; and functionalized with MUA, in red; for AuNP of 13 nm (left) and 42 nm (right).

The slight red-shifts confirm a successful functionalization, with 6 nm for the 13 nm AuNP and 2 nm for the 42 nm AuNP. Note that the smaller red-shift for the larger AuNP is expected, since the difference in refractive index at the AuNP surface is more subtle, with no observable aggregation, as indicated by the low absorbance at 750-600 nm.

Conjugation with protein was also evaluated through UV-Vis spectroscopy prior to assays using AuNP-protein conjugates samples, based on the same principle. For example, a red-shift of 7 nm was measured for 13 nm AuNP-MUA upon conjugation with bovine serum albumin (BSA) (figure 4.6).

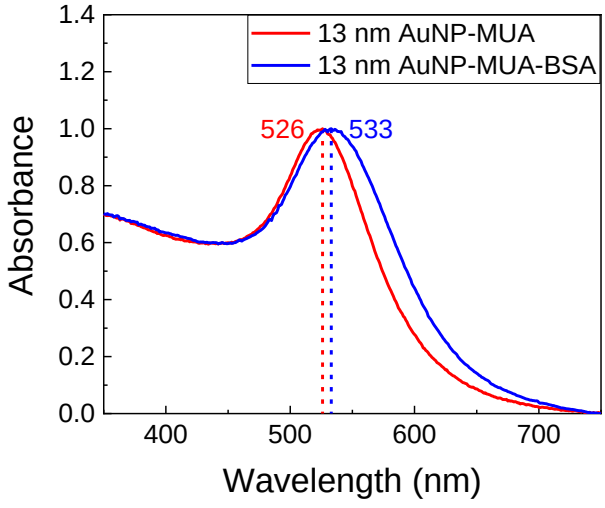

Figure 4.6. Comparison between the normalized UV-Vis absorbance spectra of unconjugated 13 nm AuNP-MUA, in red; and conjugated with BSA, in blue.

4.2 Protein quantitative and qualitative characterisation

A bicinchoninic acid (BCA) assay was performed for all protein solutions prepared, in order to quantitate protein concentration, whilst SDS-PAGE allowed for the evaluation of both stock protein quality and molecular weights, given the sequential and structural differences between the studies proteins (BSA, HSA, BPF and HPF).

4.2.1 Bicinchoninic acid assay

A calibration curve was obtained from a BSA standard and used for all studied proteins. The studied proteins present a different number of residues which are known to directly influence colour formation, namely Cys, Tyr and Trp (table 2).[74,76,77] This is especially evident for plasma fibrinogen, yet this discrepancy is minimised by different residue accessibilities and the fact that the universal peptide backbone also contributes to colour formation.[76,77]

Table 4.2. Number of cysteine, tyrosine and tryptophan residues in BSA, HSA, BPF and HPF.

No. of residues	BSA	HSA	BPF	HPF
Cysteine	35	35	54	58
Tyrosine	20	18	92	96
Tryptophan	2	1	66	66
Total	57	54	212	220

This is important to consider, since some proteins reduce different amounts of Cu^{2+} than BSA, therefore resulting in a different absorbance at 562 nm of the BCA-Cu^{+} complexes formed for the same protein concentration.[76]

However, good correlations were found between the theoretical protein concentration (mg/mL) calculated from the amount of protein weighted (mg; purity was considered) and volume of buffer (mL); and the protein concentration determined by the BCA assay, for serum albumins and fibrinogens alike (table 4.3).

Table 4.3. Correlation between the theoretical concentration of each protein solution and respective concentration determined by the BCA assay

Protein	Theoretical concentration (mg/mL)	Concentration as per the BCA assay (mg/mL)	Correlation (%)
BSA	0.5	0.492	98.4
HSA	0.5	0.501	99.8
BPF	0.5	0.447	89.4
HPF	0.5	0.493	98.6

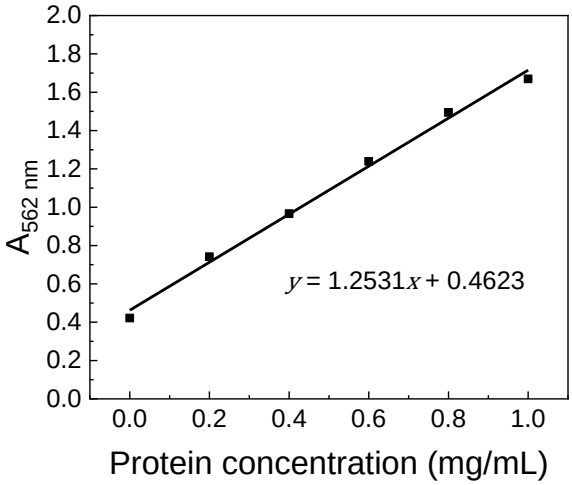

Figure 4.7. BSA standard calibration curve for the BCA assay and respective equation, fitted with an $R^2 = 0.994$.

4.2.2 SDS-PAGE

In order to evaluate stock protein quality for each studied protein (BSA, HSA, BPF and HPF) and compare the monomeric molecular weights between respective bovine and human counterparts, an SDS-PAGE was performed.

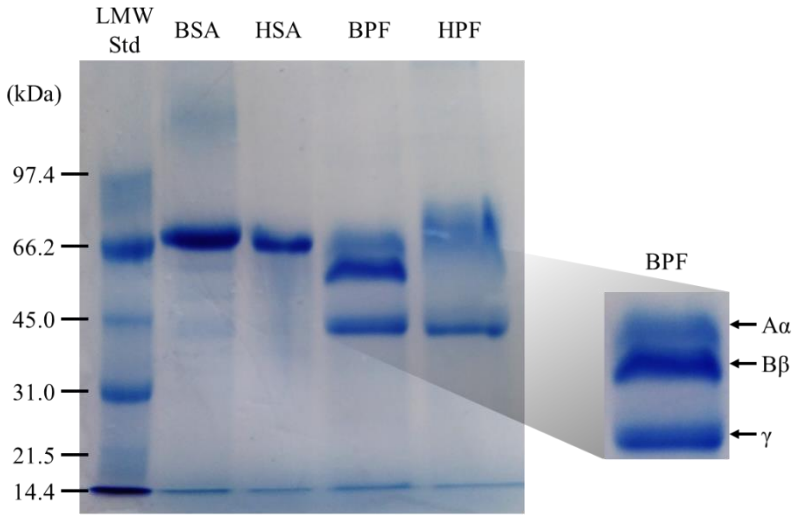

Figure 4.8. SDS-PAGE with bovine and human counterparts of serum albumin (BSA and HSA, respectively) and of plasma fibrinogen (BPF and HPF, respectively), using a low molecular weight standard (LMW std).

This SDS-PAGE image was processed through the eReuss software, set to detect six peaks of band colour intensity – assigning a Gaussian curve to each one – per the six standard bands, which were subsequently used to calculate a calibration curve through which the monomeric molecular weights for each studied protein were estimated in function of electrophoretic mobility of respective band or bands (the one with the highest colour intensity for both serum albumins and the three highest for fibrinogens).

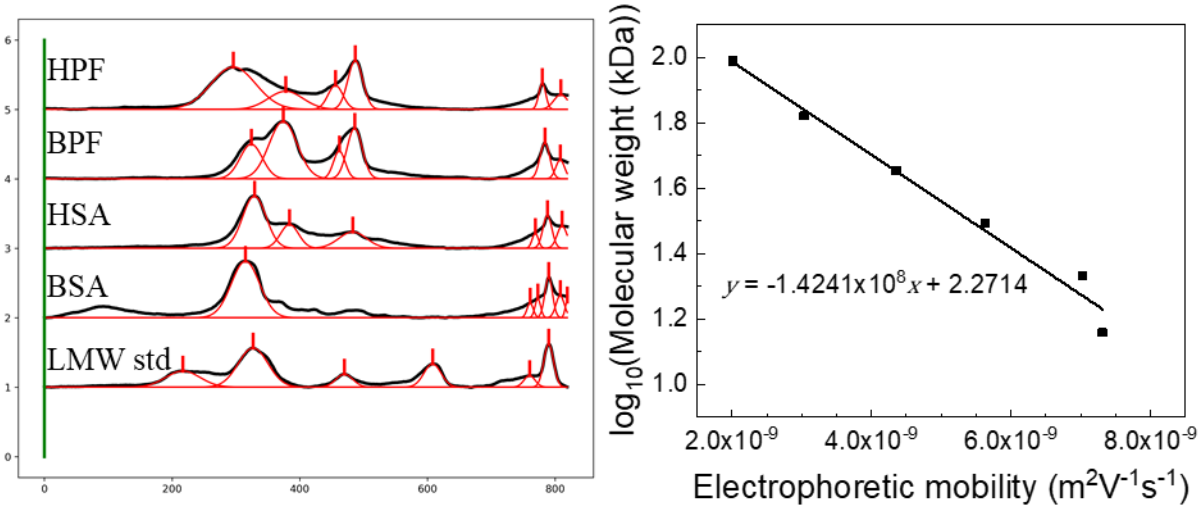

Figure 4.9. eReuss SDS-PAGE band migration profile (left), through which a molecular weight calibration curve in dependence of electrophoretic mobility (right) and respective equation ($R^2 = 0.979$) were obtained from the low molecular weight standard (LMW std) profile.

Table 4.4. Comparison between the monomeric molecular weights obtained from the eReuss SDS-PAGE analysis and those found in literature.

Protein	**Chains**	**Literature MW (kDa)**		**Estimated MW (kDa)**	
BSA	(Monomer)	69[12,13]		71.9	
HSA	(Monomer)	69[14]		68.8	
BPF	Aα	63.5[18]	**Total** 340-342[18]	69.9	**Total** 351.4
	Bβ	56[18]		59.9	
	γ	47[18]		45.9	
HPF	Aα	64-70[19,20]	**Total** 342-383[19,20]	76	**Total** 364.2
	Bβ	57-58[19,20]		59.3	
	γ	48-49[19,20]		46.8	

From a naked eye analysis of the gel image, both BSA and HSA appeared quite identical and in agreement with the molecular weights found in literature[12–14]; although, for the fibrinogens, only BPF distinctly exhibited the expected three bands respective to its Aα, Bβ and γ chains (in descending order of molecular weight)[18–20], whereas HPF corresponded only in the γ chains, whilst Aα and Bβ were more difficult to differentiate and blended into a smear of an apparent higher molecular weight; however, this was resolved after the image was analysed with eReuss and the estimated monomeric molecular weights matched the reference ones, albeit with some overestimation for BSA and both fibrinogens.

4.2.3 Molecular visualisation

Sequence and structural comparison between the bovine and human counterparts of the studied proteins had already been done by David Peitinho, MSc[22], using the same PDB files – 3V03, 1AO6, 1DEQ and 3GHG for BSA, HSA, BPF and HPF, respectively – and performing both a global and local sequence alignment through the Needleman-Wunsch and blastp algorithms, respectively; utilising the BLAST 2 Sequences software.[78] Additionally, a rigid and flexible structural alignment were conducted through the jFatCat algorithm, tool available at a RCSB PDB web server.[79]

Table 4.5. Sequence alignment between the bovine and human counterparts of serum albumin and fibrinogen.

Proteins		**Bovine and human sequence alignment**					
		Global			**Local**		
		Identity	Similarity	Gaps	Identity	Similarity	Gaps
Serum albumins		76%	88%	0%	76%	88%	0%
Fibrinogens	Aα	44%	51%	31%	58%	68%	10%
	Bβ	77%	85%	4%	82%	91%	0%
	γ	80%	88%	2%	81%	90%	1%

Table 4.6. Structural alignment between the bovine and human counterparts of serum albumin and fibrinogen.

Proteins		**Bovine and human structural alignment**			
		Rigid		**Flexible**	
		Similarity	Gaps	Similarity	Gaps
Serum albumins		88%	0%	88%	0%
Fibrinogens	Aα	82%	3%	82%	0%
	Bβ	91%	6%	93%	0%
	γ	91%	2%	91%	0%

Overall, both bovine and human counterparts of each studied protein exhibited a high sequence and structural homology (> 60%), with the exception being the Aα chains of fibrinogens, which scored poorly in the global sequence alignment, although, in the local alignment, these scored slightly higher due to the detection of conserved domains. This could be explained by the high incompletion of these chains in the PDB files, as verified by comparing the number of residues with the respective and more complete UniProt files (table 4.7).

Table 4.7. Comparison between the number of residues of BSA, HSA, BPF and HPF found in the respective PDB and UniProt files.

Files	**BSA**	**HSA**	**BPF**			**HPF**		
			Aα	**Bβ**	**γ**	**Aα**	**Bβ**	**γ**
PDB	583	585	390	408	411	562	461	411
UniProt	617	619	615	468	444	866	491	453

In order to further evaluate the structural similarities between the corresponding studied protein counterparts, the electrostatic surface potentials were mapped onto computer generated representations of each protein at different pH, defined when converting the PDB files to PQR files using the PDB2PQR web server. This also served to understand how pH alters the electronegativity at the surface of these proteins and how the adsorption to the negatively charged AuNP is affected. Due to the high sequential incompletion in the PDB file for BPF, the software could not process it for molecular visualisation.

The surface protonation patterns of both serum albumins (figures 4.10 and 4.11) appeared quite similar at the different pH simulated, revealing a prominent negative region pertaining to domain I – particularly above the pI of these proteins (5.41 for BSA; 5.47 for HSA) – and a positive site focused on a central, interior region, which could be a potential binding point to the AuNP, therefore conformational alterations upon adsorption are expected. Moreover, this positive site appears to expand to nearly cover the entire protein surface once the pH drops below the pIs. This could induce the aggregation of AuNP, since more than one negatively charged AuNP can bind to a protein surface with a predominantly positive charge.

For HPF (figure 4.12), given the size and shape of the fibrinogen molecule, the location of potential binding points to the AuNP suggest it can either adsorb to more than one AuNP, or bend to adsorb to the same nanoparticle at different points.

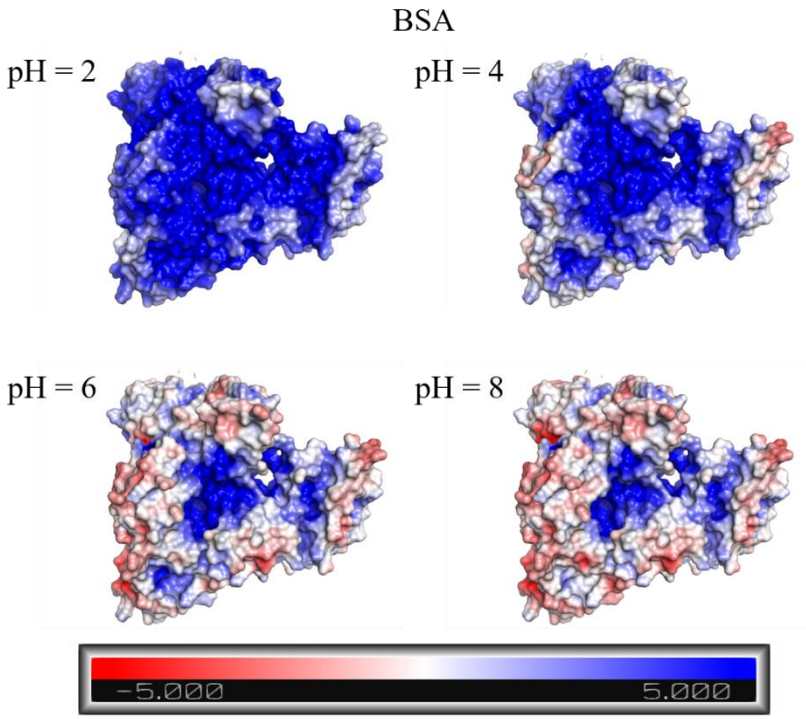

Figure 4.10. Electrostatic potential mapped onto a surface projection of BSA (PDB 3V03) at pH 2, 4, 6 and 8 in a colour gradient (red is negative, white neutral and blue positive) ranging from -5.0 to 5.0 kb T e_c^{-1}.

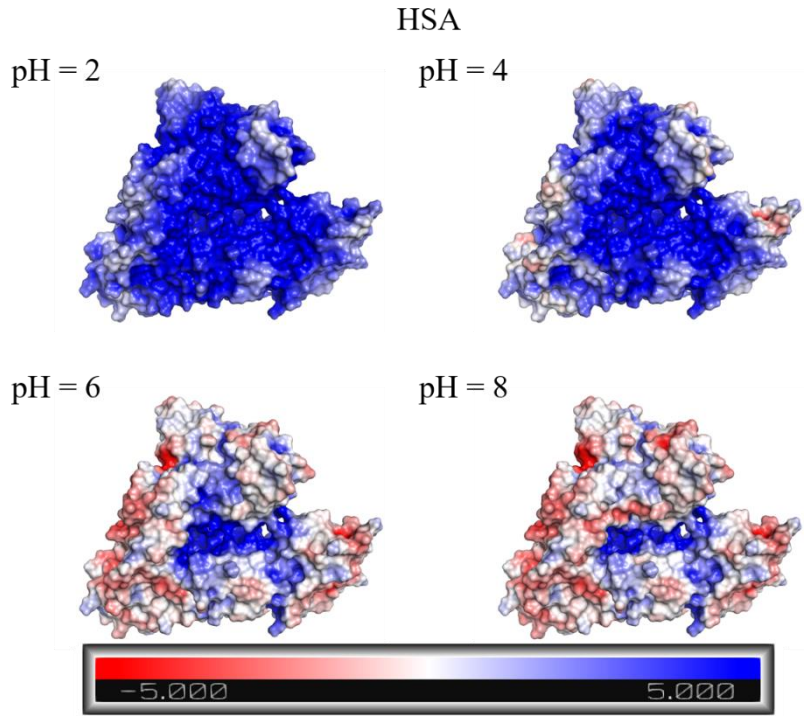

Figure 4.11. Electrostatic potential mapped onto a surface projection of HSA (PDB 1AO6) at pH 2, 4, 6 and 8 in a colour gradient (red is negative, white neutral and blue positive) ranging from -5.0 to 5.0 kb T e_c^{-1}.

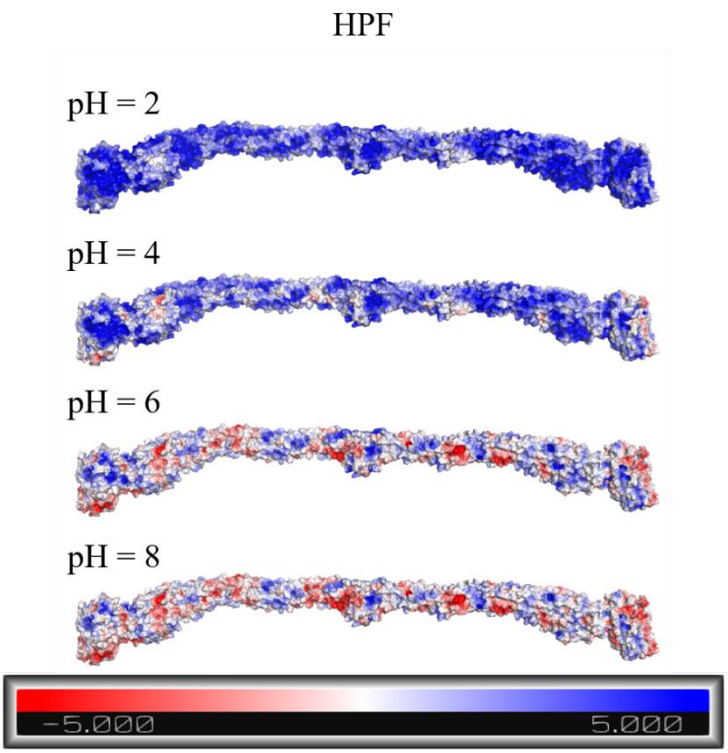

Figure 4.12. Electrostatic potential mapped onto a surface projection of HPF (PDB 3GHG) at pH 2, 4, 6 and 8 in a colour gradient (red is negative, white neutral and blue positive) ranging from -5.0 to 5.0 kb T e_c^{-1}.

Furthermore, the studied proteins were structurally compared between respective counterparts and studied for the solvent accessibility of each amino acid. This parameter is typically reported as the percentage of the accessible surface of each residue relative to that for the model pentapeptide GGXGG in its extended conformation. An entirely exposed residue would score a solvent accessibility of 100%, whereas those completely buried possess a solvent accessibility of 0%.[80] Thus, solvent accessibility was mapped onto every single amino acid of the studied proteins in a simulated projection, as well as onto all cystine residues only in another. Cysteines are important because of their thiol group, which – given the strength of the Au-S covalent bond – contribute to the stabilisation of the AuNP conjugates, despite not affecting the initial binding or the overall kinetics of the adsorption mechanism.[81,82] Paired with the electrostatic surface potential data, this also allowed to predict potential conformational alterations to the structure of these proteins upon adsorbing to the surface of AuNP, considering the accessibility of the amino acids which constitute binding points.

From the electrostatic surface potential data, the central, internal region of both serum albumins (figures 4.13 and 4.14) and the extremities and central region of HPF (figure 4.15) constitute the most probable AuNP contact points. These regions, from the solvent accessibility data, also reveal very low accessibility. This is also the case for cysteine residues, further suggesting conformational alterations are expected for these proteins upon AuNP adsorption.

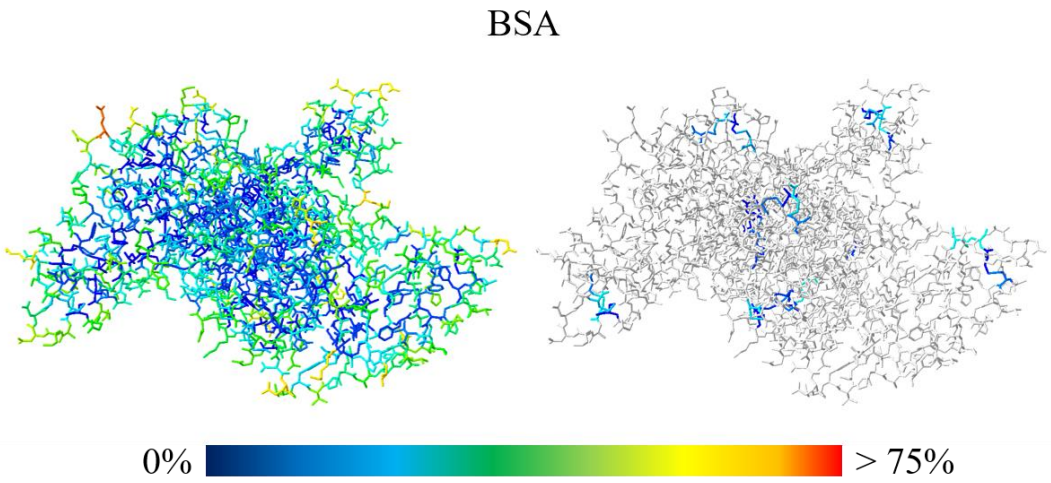

Figure 4.13. Solvent accessibility mapped onto each amino acid (left) and onto all cysteine residues only (right) of BSA (PDB 3V03) relative to a reference 100% accessibility computed for the model pentapeptide GGXGG, represented in the inset colour gradient.

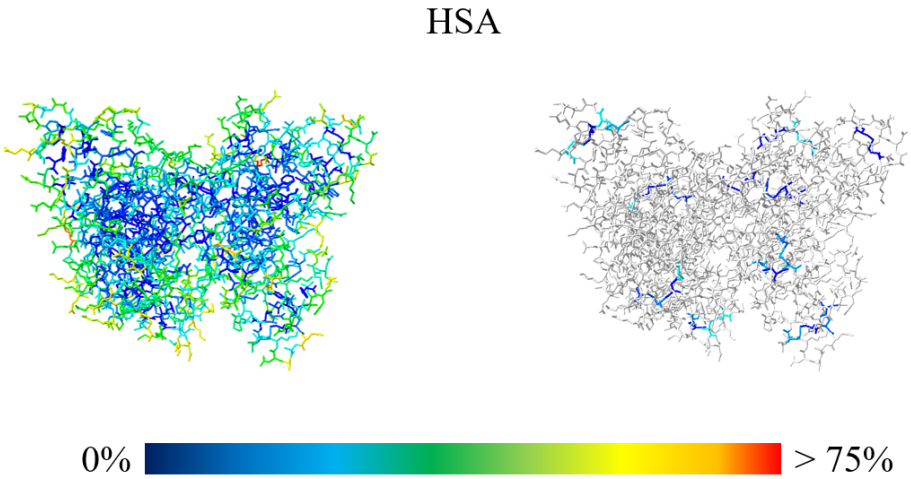

Figure 4.14. Solvent accessibility mapped onto each amino acid (left) and onto all cysteine residues only (right) of HSA (PDB 1AO6) relative to a reference 100% accessibility computed for the model pentapeptide GGXGG, represented in the inset colour gradient.

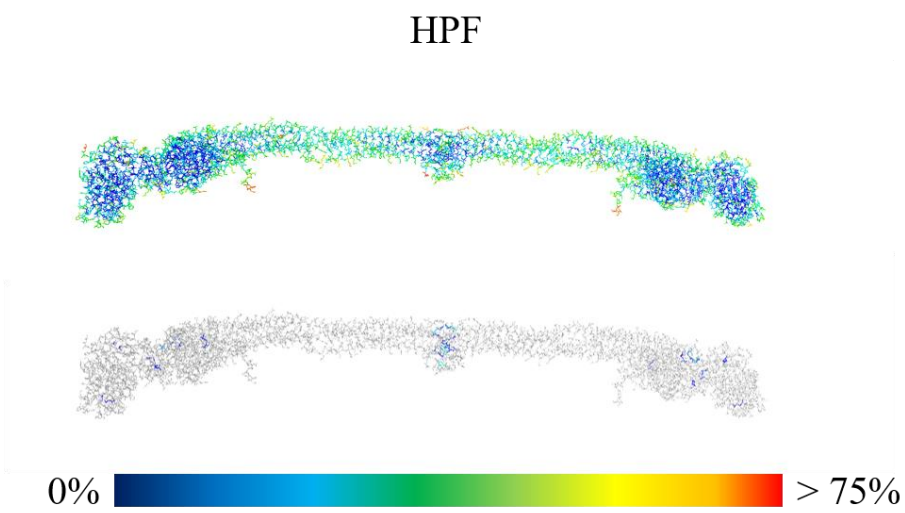

Figure 4.15. Solvent accessibility mapped onto each amino acid (left) and onto all cysteine residues only (right) of HPF (PDB 3GHG) relative to a reference 100% accessibility computed for the model pentapeptide GGXGG, represented in the inset colour gradient.

4.3 Colloidal stability assays

UV-Vis spectroscopy was employed in the comparative study of the colloidal stability of unfunctionalized 13 nm AuNP-citrate, MUA-functionalized AuNP and these AuNP-MUA conjugated with each of the studied proteins. These studies allowed to establish aggregation profiles with varying ionic strength and pH in order to further understand the colloidal behaviour of these nanoparticles and their conjugates. Moreover, complementarily to the previous assessment of protein electrostatic surface potential and solvent accessibility, these studies also allowed to characterise the surface protonation patterns for BSA, HSA, BPF and HPF, thus inferring how these proteins adsorb to the AuNP surface.

Conjugates were prepared in specific protein:AuNP molar ratios determined by AGE assays to ensure a complete coverage of the surface of AuNP with minimal excess (70:1 for both serum albumins; 8:1 for both fibrinogens). Further information on these AGE assays is detailed in the following section regarding AGE assays results.

Considering the LSPR absorbance peak of aggregated AuNP undergoes a red-shift in relation to the non-aggregated LSPR to approximately 600 nm, that wavelength was assumed as the “aggregation peak” for the aggregation quantification of AuNP and AuNP conjugates, in which the absorbance at 600 nm was divided by the absorbance at the LSPR peak of blank samples.

Figure 4.16. Unaggregated AuNP conjugate sample (left) with a highly aggregated one (right).

The aggregation profiles obtained from the $A_{600\ nm}/A_{LSPR}$ quotient produced sigmoidal curves to which the logistical dose response function could be fitted in order to find the inflection point, which represents the critical coagulation concentration (CCC), or the minimum concentration of counterions necessary to aggregate the AuNP[49,50]:

$$\frac{A_{600\,nm}}{A_{LSPR}} = \frac{A_1 - A_2}{1 + \left(\frac{x}{x_0}\right)^p} + A_2 \qquad \text{Equation 4.1}$$

A_1 and A_2 are the initial and final values, respectively, of the sigmoidal curve, x_0 its centre – the salt concentration or the pH at the inflection point – and p a power computed for the best fitting possible of the function to the curve.

4.3.1 Ionic strength

A monovalent salt, NaCl was used to increase the ionic strength in the medium of AuNP and AuNP conjugates with each of the different studied proteins, whilst maintaining a constant pH.

The calculation of the CCC for unfunctionalized AuNP-citrate and functionalized AuNP-MUA had already been done by David Peitinho, MSc[22], namely 28 nM of NaCl for the former and 277 nM for the latter.

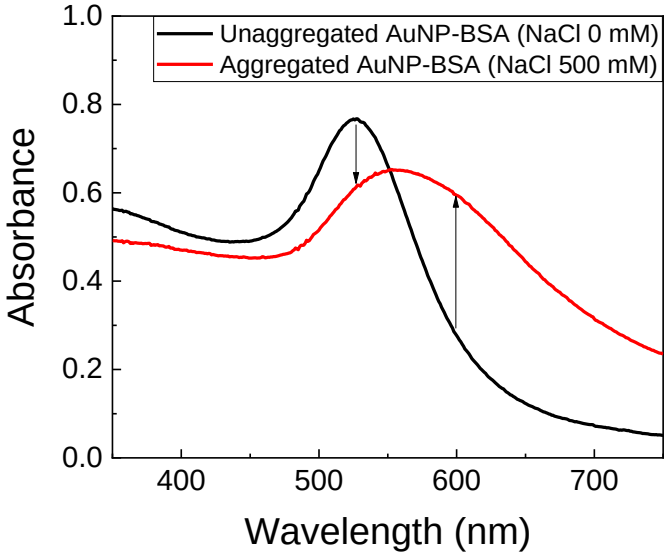

Figure 4.17. Comparison between the UV-Vis absorbance spectra of a blank, unaggregated AuNP-BSA sample (no NaCl) and one highly aggregated with 500 mM of NaCl, incubated for 30 minutes prior to measurement.

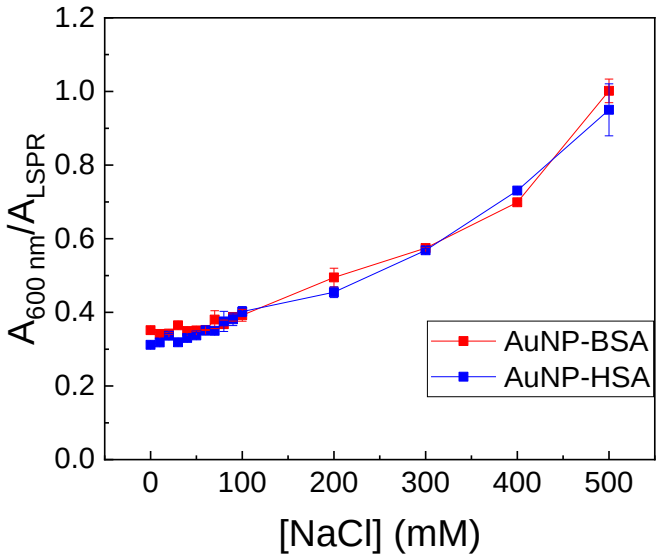

Figure 4.18. Colloidal stability profiles of 13 nm AuNP-MUA conjugated with BSA and HSA with increasing ionic strength through increment of NaCl concentration.

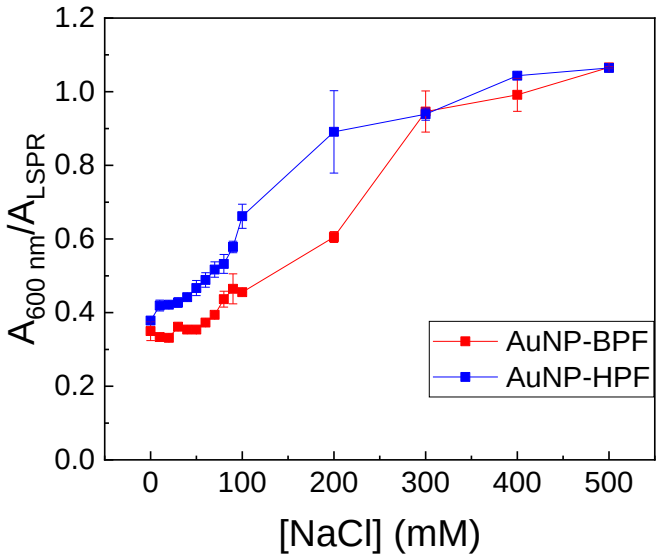

Figure 4.19. Colloidal stability profiles of 13 nm AuNP-MUA conjugated with BPF and HPF with increasing ionic strength through increment of NaCl concentration.

AuNP conjugates of either serum albumin counterpart exhibited identical aggregation profiles with the increasing ionic strength, yet it was not possible to estimate the CCC due to the inflection point not being reached with the NaCl concentration range used.

In the case of the fibrinogens, however, the aggregation profiles suggested a great difference in the colloidal stability of both AuNP conjugates relative to the unconjugated AuNP. This is corroborated by the calculated CCC of 165 and 172 nM of NaCl for the bovine and human counterpart, respectively. The values are similar and below the CCC for the unconjugated AuNP (277 nM), indicating that AuNP conjugates with BPF or HPF are more unstable than the unconjugated AuNP.

4.3.2 pH effect

AuNP and AuNP conjugates samples were adjusted to pH in a range from 2.0 to 8.0 in intervals of 0.5 with HCl or NaOH, as negatively charged AuNP are more unstable at acidic pH than basic. Care was taken so that both HCl and NaOH were never added to the same sample, as the resulting NaCl salt would overestimate the results through ionic-strength-induced aggregation.

The CCC for unfunctionalized AuNP-citrate and functionalized AuNP-MUA had already been estimated by David Peitinho, MSc,[22] as 2.7 and 3.9, respectively, which were similar to the respective reference pKa of citrate and MUA, 3.1 and 4.5.[73,83]

Although the colloidal stability profile of AuNP-BSA conjugates displayed an apparent slightly poorer efficiency in shielding the AuNP from protonation than HSA, the calculated CCC for both counterparts were similar, at 5.3 and 5.2, respectively, which were good approximations to the pI of these proteins (5.41 for BSA; 5.47 for HSA) (figure 4.20).

Conversely, the AuNP-fibrinogen conjugates presented an identical estimated CCC of 5.6, albeit more contrasting with the pI of these proteins (6.48 for BPF; 6.12 for HPF) (figure 4.21). This difference can be explained by the size, shape and location of the several potential AuNP contact points throughout the surface of fibrinogens, as observed in the electrostatic surface potential visualisation, resulting in conformational alterations in which the protein is still bound to the surface of AuNP, up to a certain protonation level, in such a way it protects the latter from aggregation.

Moreover, all protein conjugates exhibited an apparent reduced aggregation or disaggregation profile at the lowest pH measured (approximately between 2.0 and 3.0), even lower than the point of maximum aggregation for each conjugate. One possible explanation is that, considering the proteins possess a mostly positive surface charge at these pH – as shown in the electrostatic surface potential – and since the AuNP are entirely covered by protein, the electrostatic repulsions between the positively charged protein coatings of the AuNP impede these from aggregating.

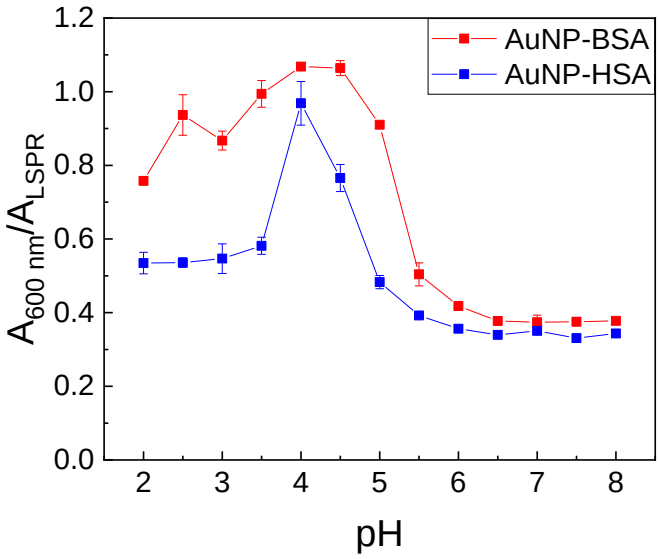

Figure 4.20. Colloidal stability profiles of 13 nm AuNP-MUA conjugated with BSA and HSA with different pH.

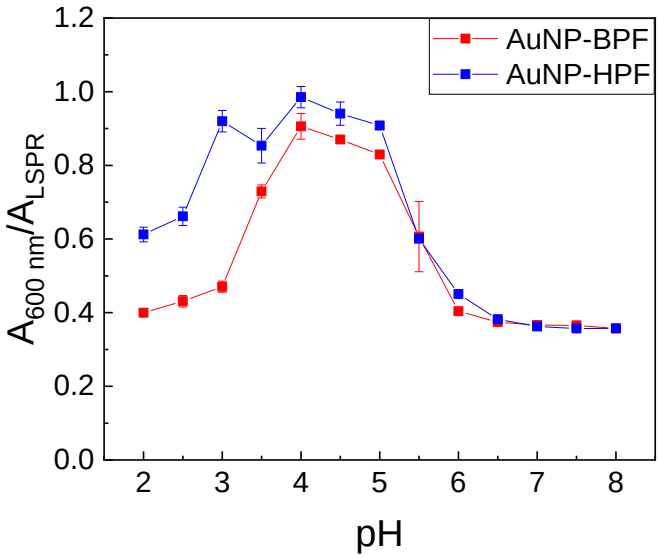

Figure 4.21. Colloidal stability profiles of 13 nm AuNP-MUA conjugated with BPF and HPF with different pH.

4.4 Circular dichroism analysis of the secondary structure of conjugated proteins

Conformational alterations on the secondary structure of the studied proteins upon adsorption to the surface of AuNP and consequent integration at the different protein coronas were assessed through CD spectroscopy at a 260-195 nm wavelength range, in which unaggregated AuNP produce no signal.[84] This was performed by comparing the CD spectra of the free proteins with those of conjugates samples in increasing protein:AuNP ratios. The values for these ratios were selected to include the conjugation curve observed in AGE assays, corresponding to the first protein monolayer (hard corona) formation. Further information on these AGE assays is detailed in the following section.

In order to ensure good CD data quality, the absorbance and high-tension voltage being applied to the photomultiplier were monitored during measurements, which should never surpass 1 and 700 V, respectively, otherwise the detector would be saturated.[85] As the protein concentrations were maintained at an optimal 757.6 nM for both serum albumins and 147.1 nM for both fibrinogens, much higher AuNP concentrations were required for the intended protein:AuNP ratios, which also caused an intensification of the absorbance and high-tension voltage on the photomultiplier. A good compromise was found for the serum albumin conjugates, but not for the fibrinogen ones, as either the protein concentration would have to be too low to acquire data of an acceptable quality, or the required high AuNP concentrations would increase the absorbance and high-tension voltage on the photomultiplier above the respective maximum thresholds, hence CD studies could not be conducted on AuNP conjugates with fibrinogens.

The CD spectra of both unbound serum albumin counterparts present the aspect characteristic to proteins predominantly comprised of α-helices, which is in agreement with the literature. Interestingly, the density of this secondary structure motif slightly decreases approximately 10.4% and 8.6% for BSA and HSA, respectively, as these proteins adsorb to AuNP. This validates the conformational alterations predicted from the previous electrostatic surface potential and solvent accessibility data, which showed the positively charged regions at the working pH (7.4) are mainly located centrally and internally in the proteins, as are the residues constituting binding points to the AuNP mostly buried, hence these proteins were expected to change structurally in order to expose these positive regions and binding points to the AuNP surface.

The calculated loss of α-helices for serum albumins in the present work corroborates the findings of Wang et al.[86], who also demonstrated the AuNP surface composition affects differently the secondary structure changes suffered by BSA, although AuNP-MUA was not studied. However, some proteins do not undergo drastic conformational alterations upon adsorption to AuNP, as Gomes et al.[87] verified with cytochrome c, which can be explained by the fact the binding points of this protein to the AuNP surface are located more externally and that it possesses two faces of a distinct electrostatic surface charge, one of which with a predominantly positive and easily accessible to the negatively charged AuNP, therefore not requiring considerable structural changes in order to expose its binding points.

Furthermore, a minor recovery of the original secondary structure of an estimated 1.6% and 0.9% for BSA and HSA, respectively, was observed as the protein:AuNP ratio increases and more protein layers are formed. Since this technique measures the secondary structure of the outermost surface layer of conjugates, this could indicate that the greater the distance between these proteins and the AuNP, the less conformational alterations the former suffer.

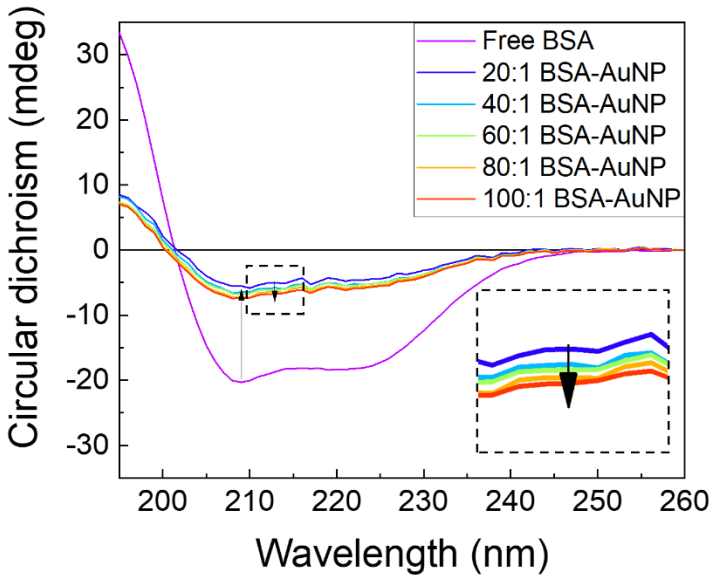

Figure 4.22. Comparison between the CD spectra in a wavelength range of 260-195 nm of free, unbound BSA and bound to 13 nm AuNP-MUA in increasing protein:AuNP molar ratios.

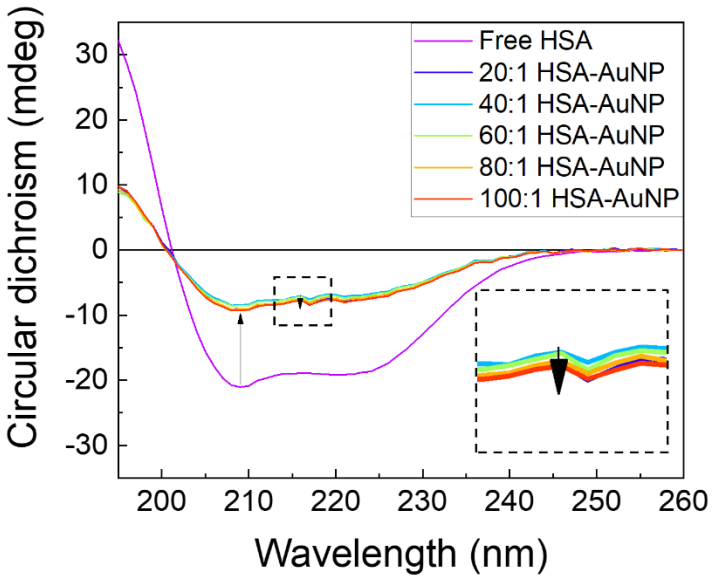

Figure 4.23. Comparison between the CD spectra in a wavelength range of 260-195 nm of free, unbound HSA and bound to 13 nm AuNP-MUA in increasing protein:AuNP molar ratios.

4.5 Dynamic light scattering analysis of the protein corona hydrodynamic diameter

Some literature[7,8,59,61] claims centrifugation can effectively remove the loosely bound outer layers of a protein corona (collectively known as the soft corona) by disrupting the protein-protein interactions, which are comparatively weaker than those established at the AuNP surface. Since these AuNP-protein interactions can withstand the high centrifugal force, the innermost protein monolayer (hard corona) is preserved after centrifugation. Thus, the centrifugation of AuNP conjugates was the method employed to obtain samples of AuNP bearing only the innermost hard corona monolayer.

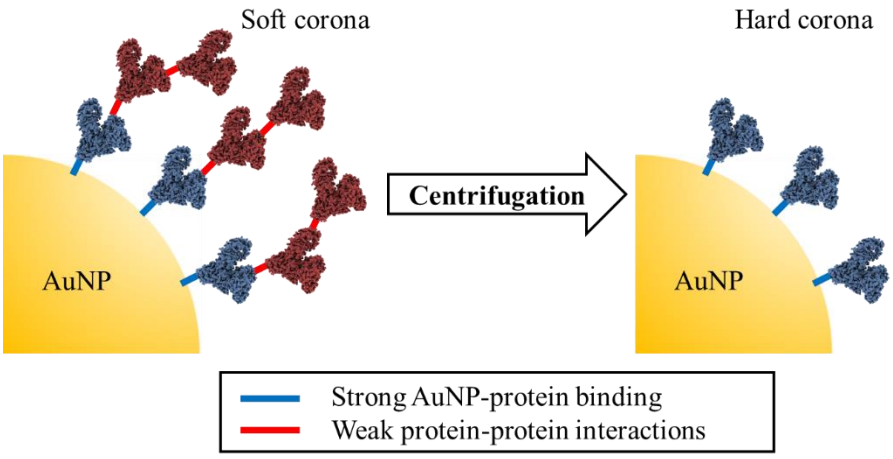

Figure 4.24. Centrifugation can break the weaker protein-protein interactions, allowing for the removal of the soft corona.

An approach to characterise the protein corona formed on AuNP with each of the studied proteins was the comparative measurement of the hydrodynamic diameters, through DLS, of conjugates samples with both coronas intact and with the hard corona only, the latter obtained after sample centrifugation.

First, the hydrodynamic diameters of unfunctionalized 13 nm AuNP-citrate, of the same AuNP functionalized with MUA and of AuNP-MUA conjugated with a monolayer of BSA were measured, as in theory these should increase in this order, since MUA is a longer molecule than citrate and the protein monolayers add to the overall size of the conjugates.

The results were favourable to theory, as a clear and consistent hydrodynamic diameter increment was observed as citrate is replaced with the longer MUA and again as BSA is adsorbed to AuNP. The difference in hydrodynamic diameter between AuNP-citrate and AuNP-MUA of approximately 2.4 nm is in agreement with the same findings by Ansar et al.[88], who calculated a difference of 2.0 nm. Despite this, it should also be noted that the polydispersity index also increases greatly, not to mention the width of all three peaks indicates some colloid size polydispersity, yet independent of the presence of protein, as evidenced by how identical the peaks appear otherwise.

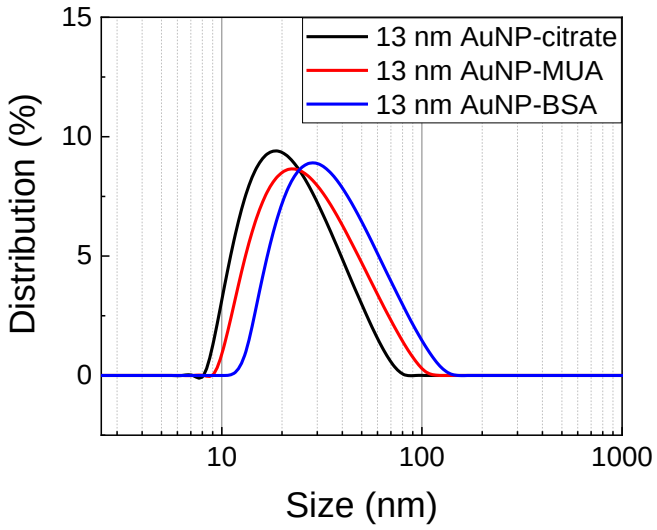

Figure 4.25. Size distribution of unfunctionalized 13 nm AuNP samples, in black; functionalized with MUA, in red; and bearing a hard corona of BSA, in blue. The peak modes for AuNP-citrate, AuNP-MUA and AuNP- BSA were 17.9, 20.3 and 25.9 nm, with z-averages of 19.4, 25.9 and 26.9 nm and polydispersity index values of 0.154, 0.373 and 0.409, respectively.

Thus, the hydrodynamic diameters were determined for AuNP of 13 and 42 nm, conjugated with purposely excessive amounts of BSA, HSA, BPF or HPF to ensure a full surface coverage (10000:1 for the serum albumins; 200:1 for fibrinogens); and with the respective hard corona samples centrifuged.

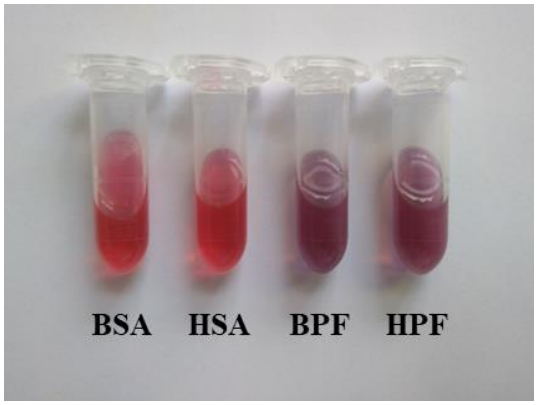

Figure 4.26. Samples of 42 nm AuNP-MUA 2 nM conjugated with BSA and HSA in a 10000:1 protein:AuNP ratio and with BPF and HPF in a 200:1 protein:AuNP ratio.

Centrifugation was verified to induce AuNP aggregation with a higher probability for conjugates samples presenting some instability, such as the fibrinogen ones, particularly for higher protein:AuNP molar ratios, which were beginning to shift to a bluer hue after the conjugation procedure. However, it should also be considered that denser aggregates amidst the colloidal suspension precipitate, whereas unaggregated particles remain suspended and in the laser path, albeit the sample concentration decreases with the formation of precipitates. This is not be a problem, however, since DLS is a sensitive technique which can measure highly diluted samples.[51]

Interestingly, a decrease in hydrodynamic diameter for the centrifuged samples, as theoretically expected, was observed in the smaller, 13 nm AuNP conjugated with either serum albumin; and in the larger, 42 nm AuNP with either fibrinogen counterparts (figures 4.27 to 4.31). Supplemental data with z-average and polydispersity index values can be found in Appendix IV, table IV.1.

One possible explanation for the high discrepancy found between the sizes of uncentrifuged and centrifuged 13 nm AuNP conjugated with fibrinogen is that, given to the structural shape and tendency to coagulate characteristic to this protein, as well as being much larger than the AuNP, it could adsorb to more than one nanoparticle with higher probability due to steric proximity when compressed into a pellet, as a consequence of centrifugation.

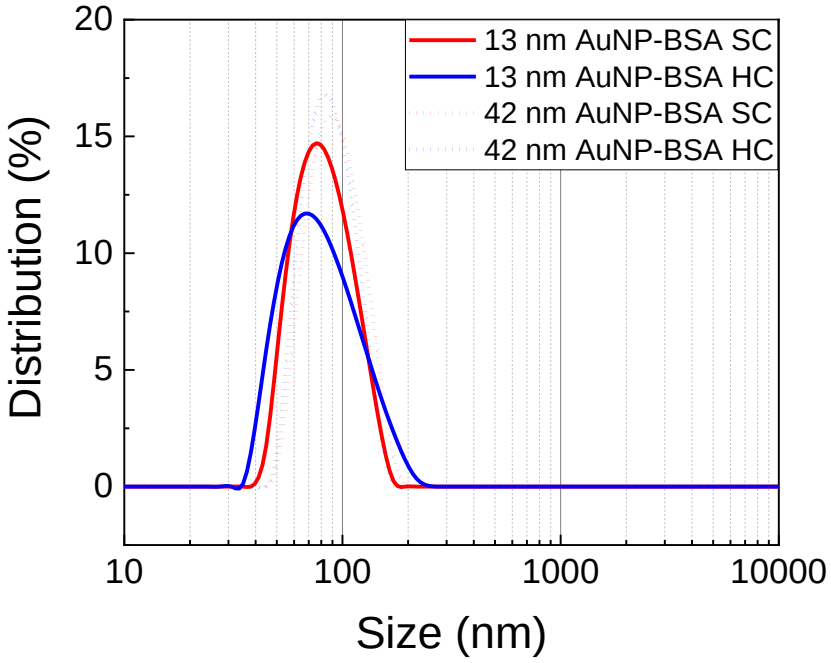

Figure 4.27. Size distribution of 13 and 42 nm AuNP-MUA conjugated with BSA in a protein:AuNP molar ratio of 10000:1, uncentrifuged to bear the soft corona (SC) and centrifuged to expose the hard corona (HC).

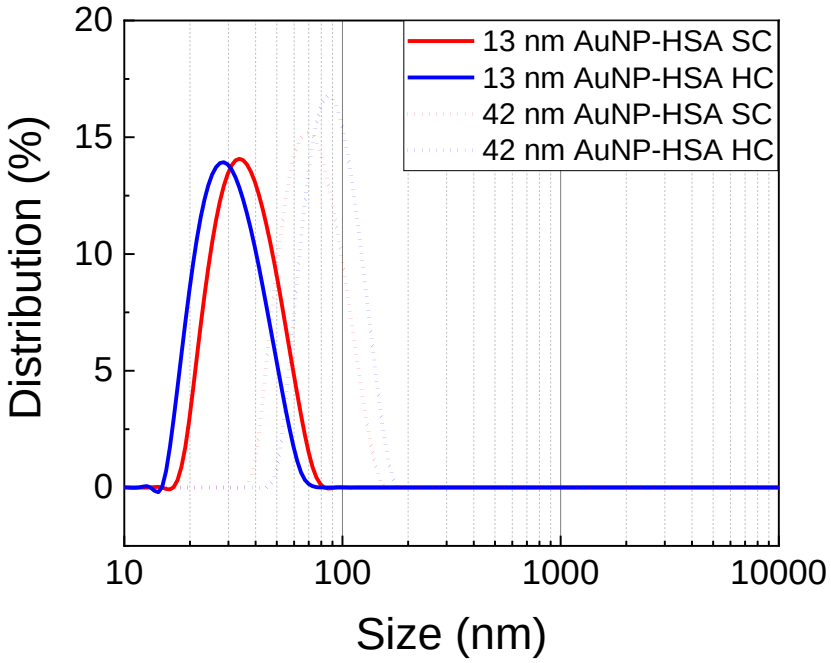

Figure 4.28. Size distribution of 13 and 42 nm AuNP-MUA conjugated with HSA in a protein:AuNP molar ratio of 10000:1, uncentrifuged to bear the soft corona (SC) and centrifuged to expose the hard corona (HC).

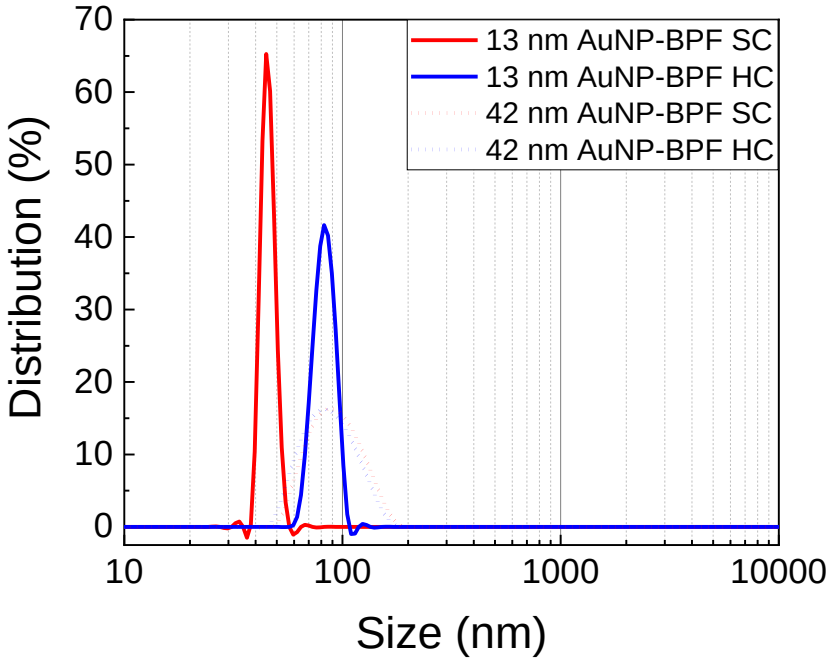

Figure 4.29. Size distribution of 13 and 42 nm AuNP-MUA conjugated with BPF in a protein:AuNP molar ratio of 200:1, uncentrifuged to bear the soft corona (SC) and centrifuged to expose the hard corona (HC).

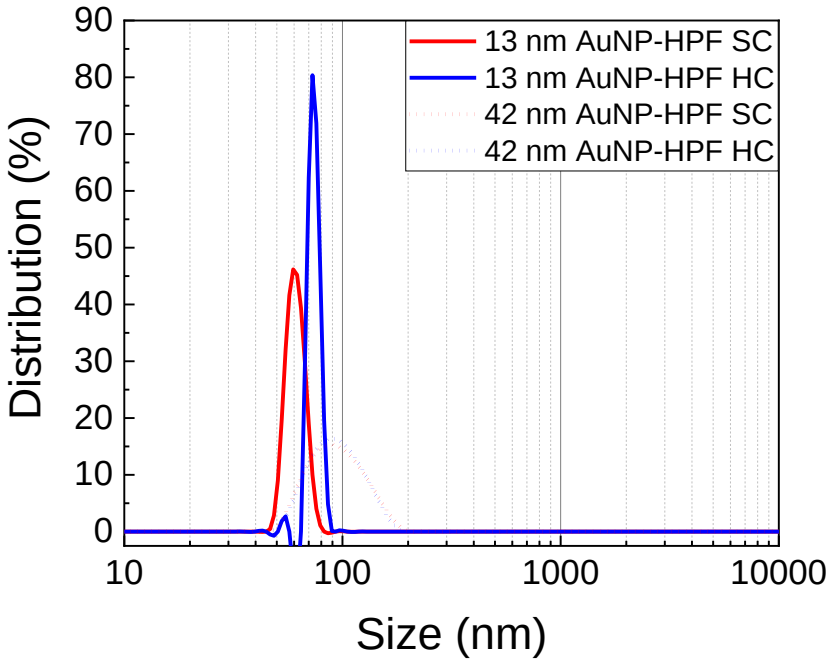

Figure 4.30. Size distribution of 13 and 42 nm AuNP-MUA conjugated with HPF in a protein:AuNP molar ratio of 200:1, uncentrifuged to bear the soft corona (SC) and centrifuged to expose the hard corona (HC).

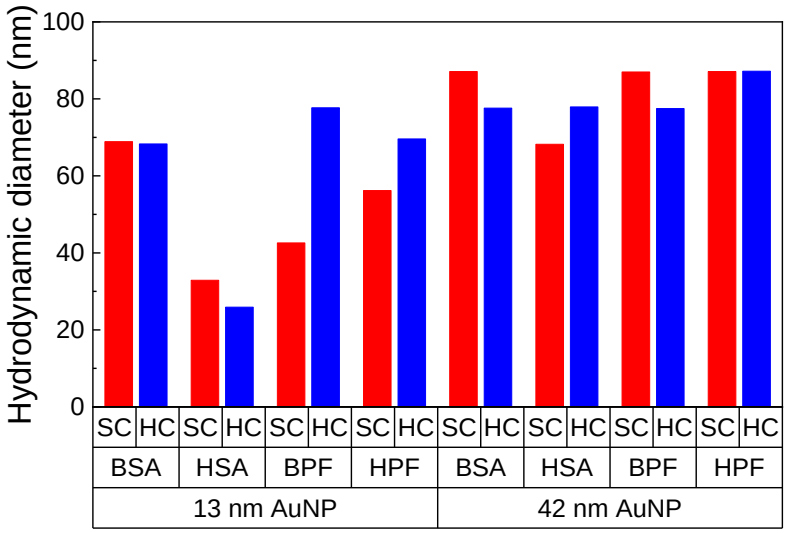

Figure 4.31. Soft corona (SC) and hard corona (HC) hydrodynamic diameter comparison between 13 and 42 nm AuNP-MUA samples conjugated with a purposely excessive amount of BSA, HSA, BPF and HPF.

This study was furthered for these conjugates with different protein:AuNP ratios and the 42 nm AuNP, as these not only produced better results with both fibrinogens, but also generated sharper curves with lower polydispersity for both serum albumins.

Only the BPF conjugates exhibited the theoretically expected profile (figures 4.32 to 4.36), with the hydrodynamic diameter increasing after centrifugation merely for the conjugate sample with the lowest protein:AuNP ratio of 2:1, which could be explained by an incomplete coverage of the surface of AuNP, thus rendering these prone to aggregation during centrifugation; whereas it decreased as more protein was added, allowing the full formation of the innermost hard corona, before the soft corona can begin to assemble. As for the conjugates with the other proteins, it is still unclear why the hydrodynamic diameters systematically increased after centrifugation, other than due to aggregation. Another possible explanation is that a hard corona is actually impossible to achieve with MUA-functionalized AuNP due to proteins not binding strongly enough with the negatively charge surface as with a positively charged surface.[68] In this case, only a soft corona would be formed, which centrifugation removed to expose the bare AuNP, more prone to centrifugation-induced aggregation.

The graphs shown in figures 4.32 to 4.35 were generated through a Python script created by Prof. Ludwig Krippahl.

Supplemental data with z-average and polydispersity index values can be found in Appendix IV, table IV.2.

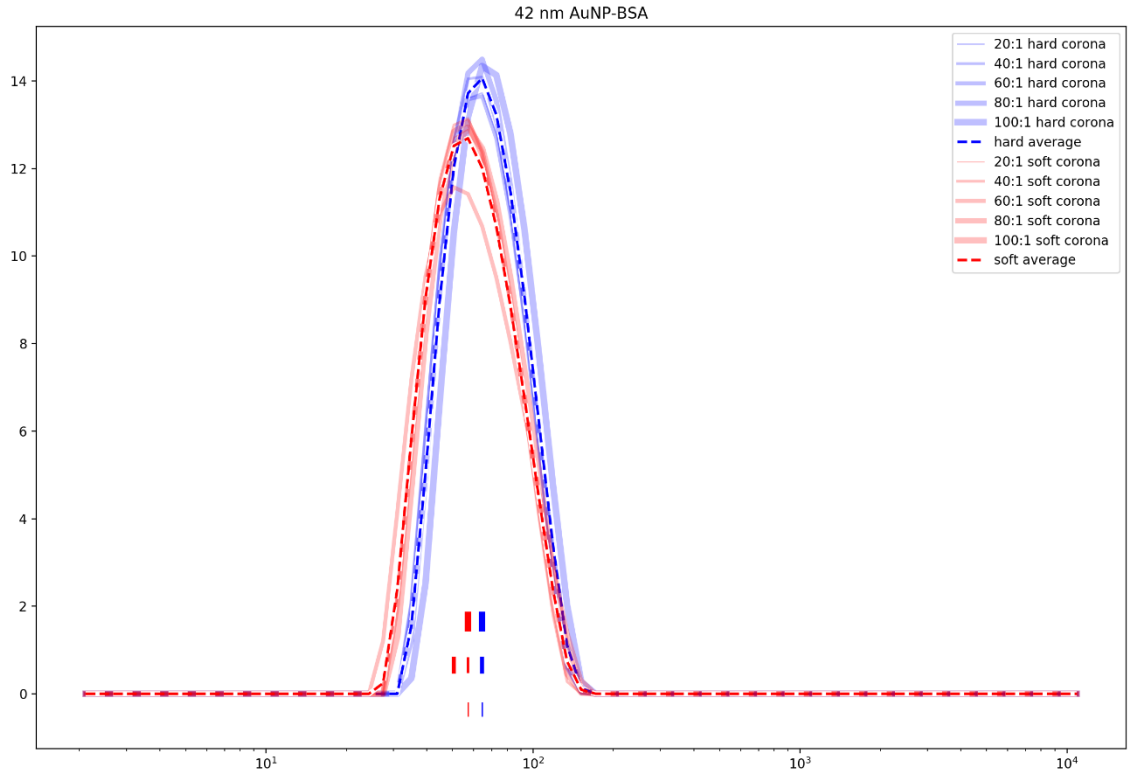

Figure 4.32. Size distribution of 42 nm AuNP-MUA conjugated with BSA in the increasing protein:AuNP ratios of 20:1, 40:1, 60:1, 80:1 and 100:1; of soft corona and hard corona.

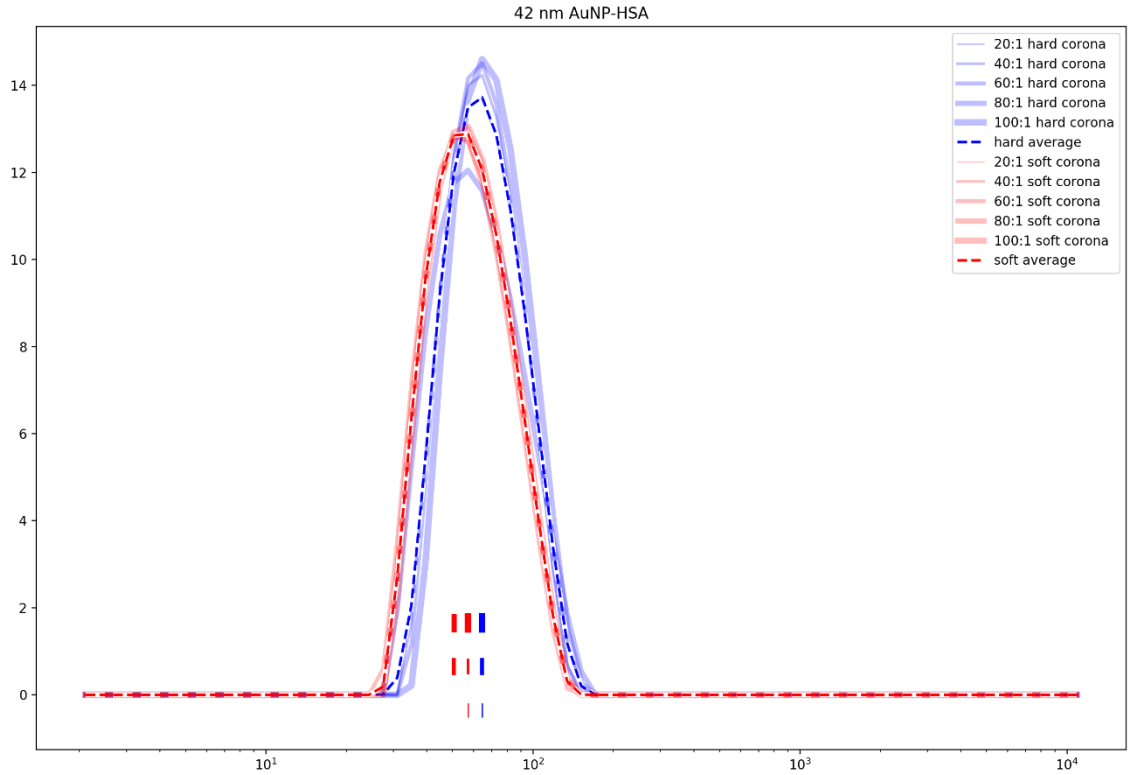

Figure 4.33. Size distribution of 42 nm AuNP-MUA conjugated with HSA in the increasing protein:AuNP ratios of 20:1, 40:1, 60:1, 80:1 and 100:1; of soft corona and hard corona.

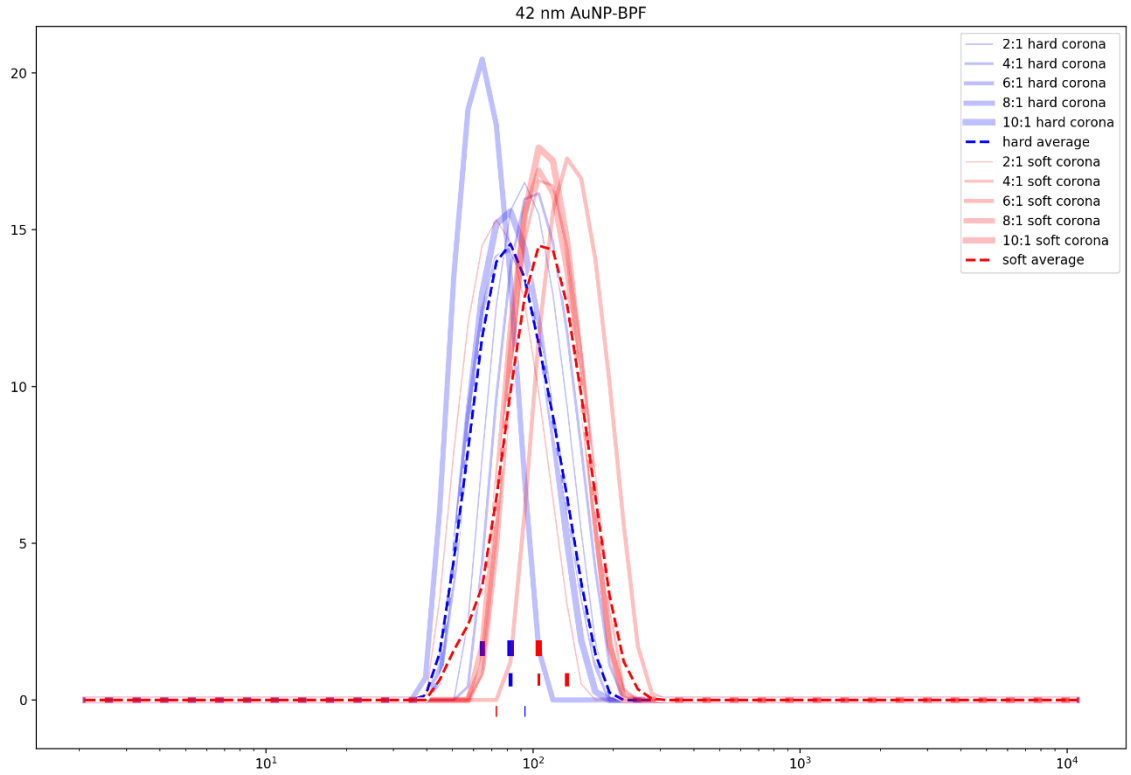

Figure 4.34. Size distribution of 42 nm AuNP-MUA conjugated with BPF in the increasing protein:AuNP ratios of 2:1, 4:1, 6:1, 8:1 and 10:1; of soft corona and hard corona.

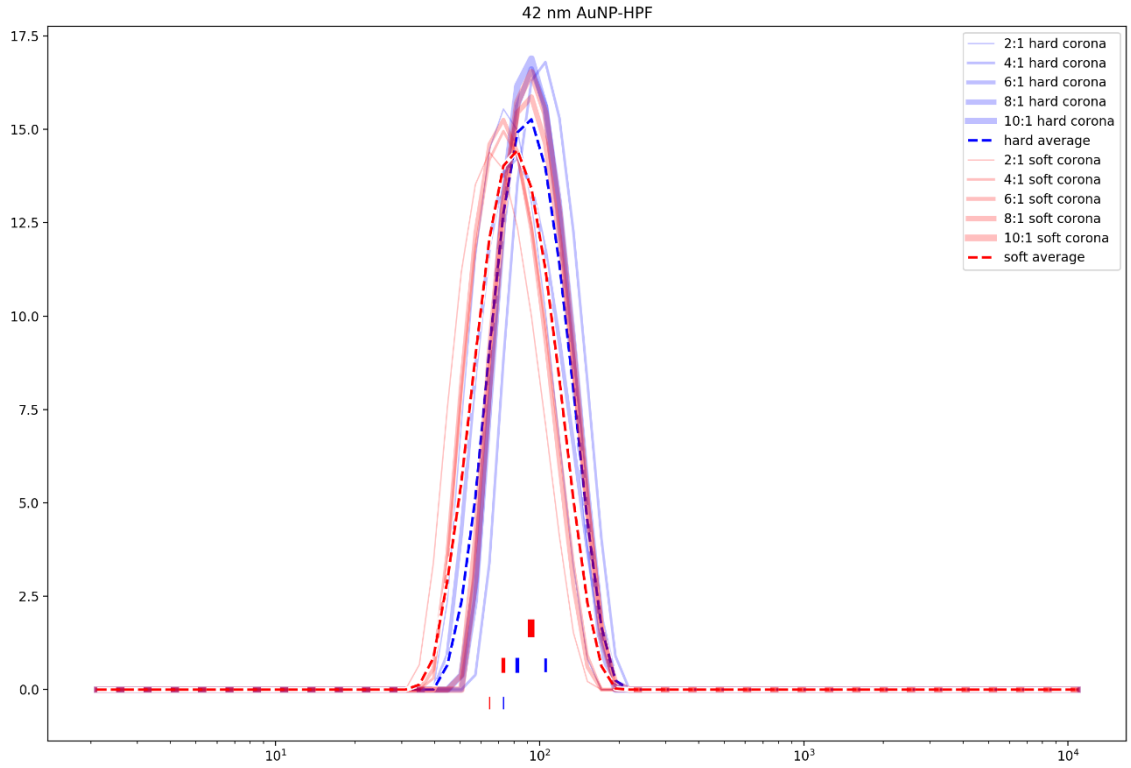

Figure 4.35. Size distribution of 42 nm AuNP-MUA conjugated with HPF in the increasing protein:AuNP ratios of 2:1, 4:1, 6:1, 8:1 and 10:1; of soft corona and hard corona.

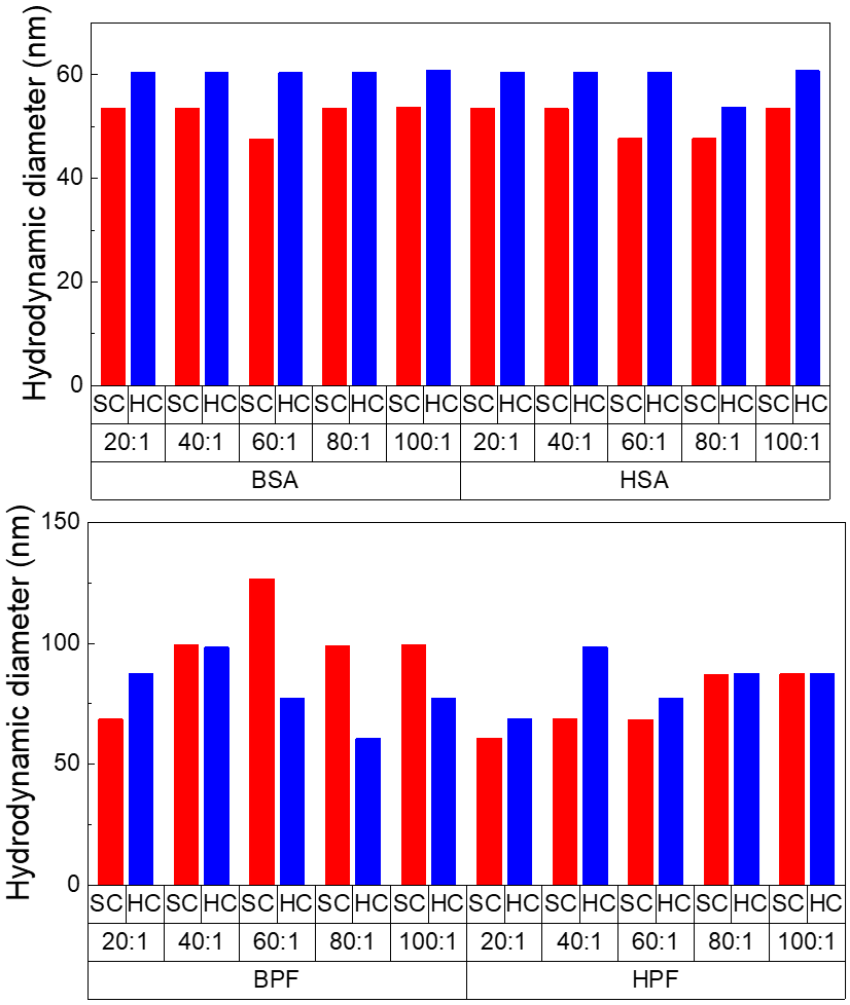

Figure 4.36. Soft corona (SC) and hard corona (HC) hydrodynamic diameter comparison of 42 nm AuNP-MUA samples conjugated with BSA, HSA, BPF and HPF in increasing protein:AuNP ratios.

4.6 Agarose gel electrophoretic assays

Electrophoretic mobility profiling was useful for a detailed characterisation of AuNP conjugates with the different studied proteins, as through AGE assays with samples of an increasing protein:AuNP molar ratio it was possible to not only perceive the amount of each protein required for a full coverage of the surface of AuNP from the resulting conjugation curve, but also estimate the binding constant of these to the functionalized AuNP-MUA.

First, an AGE assay was performed for AuNP conjugates with BSA in the protein:AuNP molar ratios of 10:1 to 100:1 in intervals of 10:1; and then until 500:1 in intervals of 100:1. Electrophoresis run times varied between 20 or 30 minutes, in order to achieve the maximum possible gel image quality, as shorter runs resulted in more imperceptible band mobility differences, but longer runs increased band smearing. For this assay, a run of 20 minutes was sufficient for the intended purpose (figure 4.37).

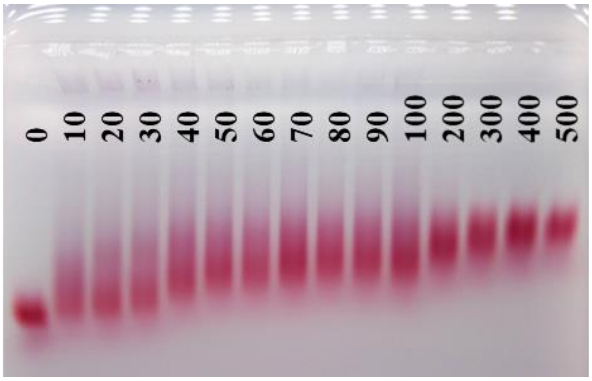

Figure 4.37. AGE bands of 13 nm AuNP-MUA at 2 nM conjugated with BSA in different protein:AuNP molar ratios, after a run of 20 minutes.

This agarose gel image was subsequently processed through the eReuss software, which allowed for an accurate measurement of the distance travelled by each band through the gel and, from this data, the difference in electrophoretic mobility relative to the unconjugated AuNP-MUA was calculated and plotted against the BSA concentration in each sample (figure 4.38). The Hill-Langmuir equation could be fitted to the resulting curve, with an $R^2 = 0.979$, which yielded a maximum electrophoretic mobility difference, $\Delta\mu_{max} = 6.96 \times 10^{-9}\ m^2V^{-1}s^{-1}$ and a binding constant, $K_a = 9.01 \times 10^{-3}$. It should be noted that, despite the Langmuir adsorption model having the best fitting to the electrophoretic mobility difference profiles, it assumes the initial protein concentration as the free protein concentration over time and that the loss of electrophoretic mobility is linearly proportional to AuNP surface occupancy. These are both inaccurate assumptions and, therefore, translate into some degree of error for the approximated binding constants. For this same reason, approximation artefacts affect the Hill coefficient calculation to an even greater extent, thus leading to erroneous assumptions of the degree of binding cooperativity.

Moreover, the BSA:AuNP ratio of 70:1 appeared to be the first point in a scaffold towards which the conjugation curve developed, possibly marking the BSA:AuNP ratio at which the surface of AuNP is entirely covered with the protein, meaning more BSA added beyond this point would form secondary protein layers (soft corona) above the innermost monolayer (hard corona).

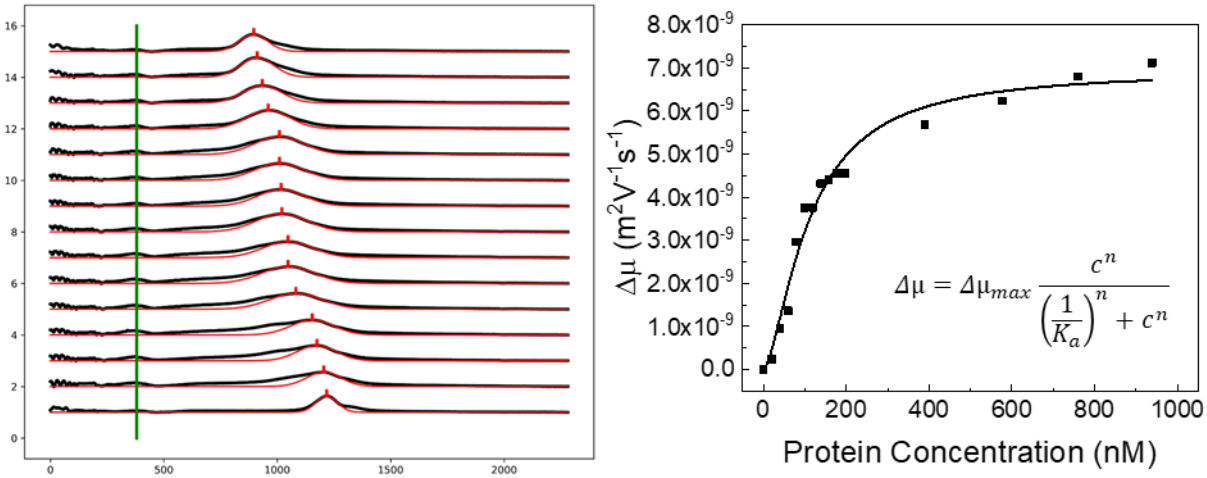

Figure 4.38. eReuss rendering of the band migration profiles for the above AGE image of a AuNP-BSA conjugates run of 20 minutes (left) and respective plot of the electrophoretic mobility difference relative to the unconjugated sample in dependence of protein concentration (right), fitted to a Hill-Langmuir equation.

The same procedure was repeated for AuNP conjugates with the other studied proteins. As HSA exhibited great structural and chemical similarities to its bovine counterpart in the previous studies, the same protein:AuNP molar ratios were used and an electrophoretic run of 20 minutes was also sufficient for a good image quality (figure 4.39).

A Hill-Langmuir fitting (figure 4.40), with an $R^2 = 0.979$, resulted in a maximum electrophoretic mobility difference, $\Delta\mu_{max} = 2.45 \times 10^{-9}$ $m^2V^{-1}s^{-1}$ and a binding constant, $K_a = 7.76 \times 10^{-2}$. Interestingly, despite the similarities found between both serum albumin counterparts in the preceding studies, AuNP conjugates with either protein exhibited different electrophoretic mobility profiles, namely the fact that a lower amount of HSA was required for completing the hard corona, with the first point of the scaffold at a HSA:AuNP ratio of 20:1; and that the binding constant calculated for HSA was higher than BSA.

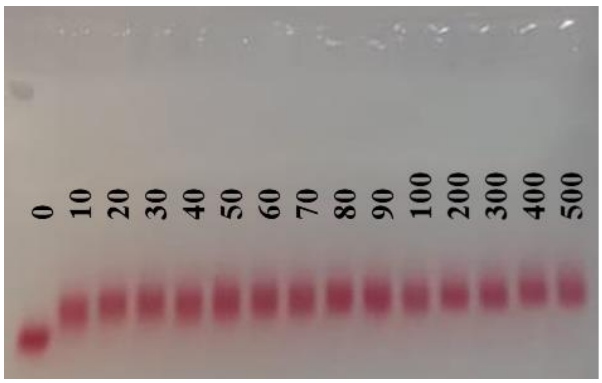

Figure 4.39. AGE bands of 13 nm AuNP-MUA at 2 nM conjugated with HSA in different protein:AuNP molar ratios, after a run of 20 minutes.

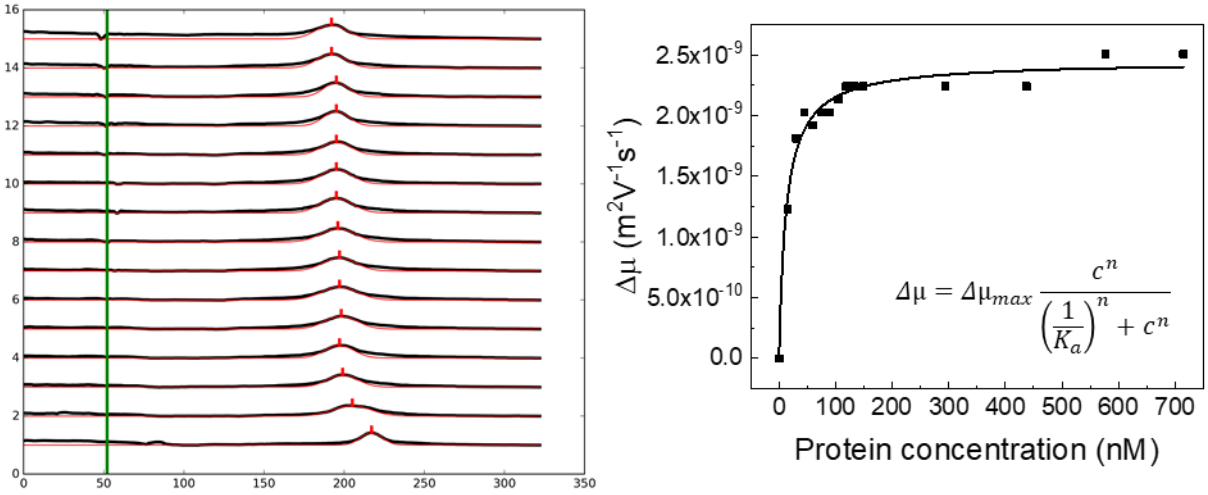

Figure 4.40. eReuss rendering of the band migration profiles for the above AGE image of a AuNP-HSA conjugates run of 20 minutes (left) and respective plot of the electrophoretic mobility difference relative to the unconjugated sample in dependence of protein concentration (right), fitted to a Hill-Langmuir equation.

As fibrinogens are much larger proteins than serum albumins, a conjugation curve was expected at a lower protein:AuNP ratio range. An AGE assay was conducted for AuNP-BPF conjugates in ratios from 2:1 to 10:1 in intervals of 2:1, then 20:1 and 300:1, the latter used to test the profile of a sample saturated with fibrinogen; and performed on the same gel, side by side, with AuNP-BSA conjugates for a conjugation curve reference (figure 4.41).

Contrary to BSA or HSA, BPF displayed three bands per lane on the lowest protein:AuNP ratios, which appear to blend with the topmost band as more protein is added – evidenced by the eReuss graph detecting dimmer band colour intensity peaks shifting to the top position (figure 4.42). One possible explanation to this phenomenon is that, at lower protein:AuNP ratios, in which the amount of protein is insufficient to completely cover the surface of all AuNP present, several populations of AuNP with a different number of adsorbed proteins form – only the difference in electrophoretic mobility imparted by one more or one less serum albumin to the AuNP is so negligible that these populations blend in a single band. However, for BPF, because of its larger dimensions, this difference in the electrophoretic mobility imparted by a difference of one protein to the AuNP is much more noticeable, hence the greater number of bands.

The Hill-Langmuir equation could only be fitted to the topmost bands, with an $R^2 = 0.993$, which resulted in a $\Delta\mu_{max} = 1.43 \times 10^{-8}$ $m^2V^{-1}s^{-1}$ and a binding constant, $K_a = 3.48$.

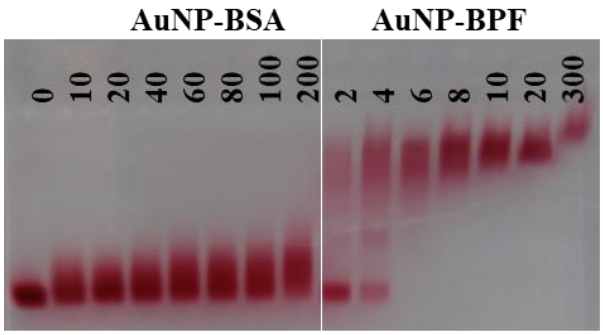

Figure 4.41. AGE bands corresponding to 13 nm AuNP-MUA 2 nM conjugated with BSA (left) and BPF (right) in different protein:AuNP molar ratios, after a run of 20 minutes.

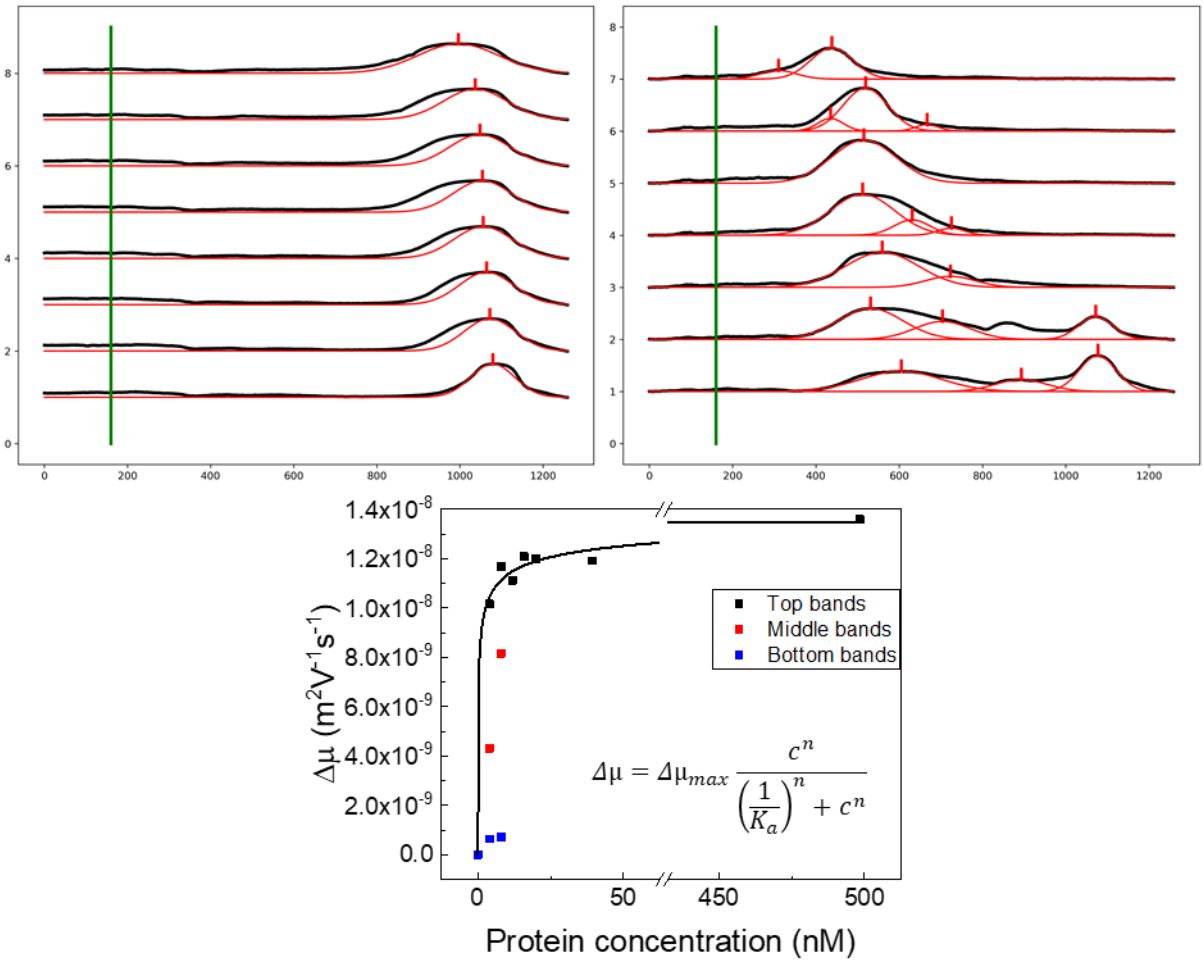

Figure 4.42. Band migration profiles for the above AGE image of a AuNP-BSA (top left) and AuNP-BPF (top right) conjugates run of 20 minutes and plotted electrophoretic mobility difference relative to the unconjugated sample against protein concentration for the BPF conjugates (bottom), with a Hill-Langmuir fitting to the top bands.

An AGE assay was performed for AuNP conjugates with HPF in a narrower protein:AuNP ratio range of 1:1 to 10:1 in intervals of 1:1, then to 25:1 in intervals of 5:1 (figure 4.43).

Similarly to its bovine counterpart, three bands were observed for HPF (figure 4.44), albeit the two lowermost rows of bands were still quite visible for the highest protein:AuNP ratios, which was not true in the BPF AGE assay. This allowed to detect another phenomenon, as the colour intensity of the lowermost bands appears to gradually decrease, whilst that of the topmost bands increases, which suggests a theoretically expected shift in the population number of AuNP bound to more proteins as more of the latter are added.

The Hill-Langmuir equation could only be fitted to the two lowermost rows of bands.

The fitting for the middle bands, with an $R^2 = 0.998$, yielded a $\Delta\mu_{max} = 9.35 \times 10^{-9}$ $m^2V^{-1}s^{-1}$ and a binding constant, $K_a = 335.95$.

The fitting for the bottom bands, with an $R^2 = 0.902$, yielded a $\Delta\mu_{max} = 5.43 \times 10^{-10}$ $m^2V^{-1}s^{-1}$ and a binding constant, $K_a = 2.34 \times 10^{-1}$.

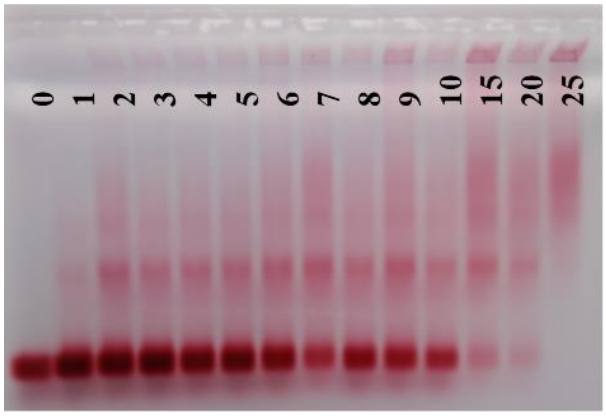

Figure 4.43. AGE bands corresponding to 13 nm AuNP-MUA 2 nM conjugated with HPF in different protein:AuNP molar ratios, after a run of 20 minutes.

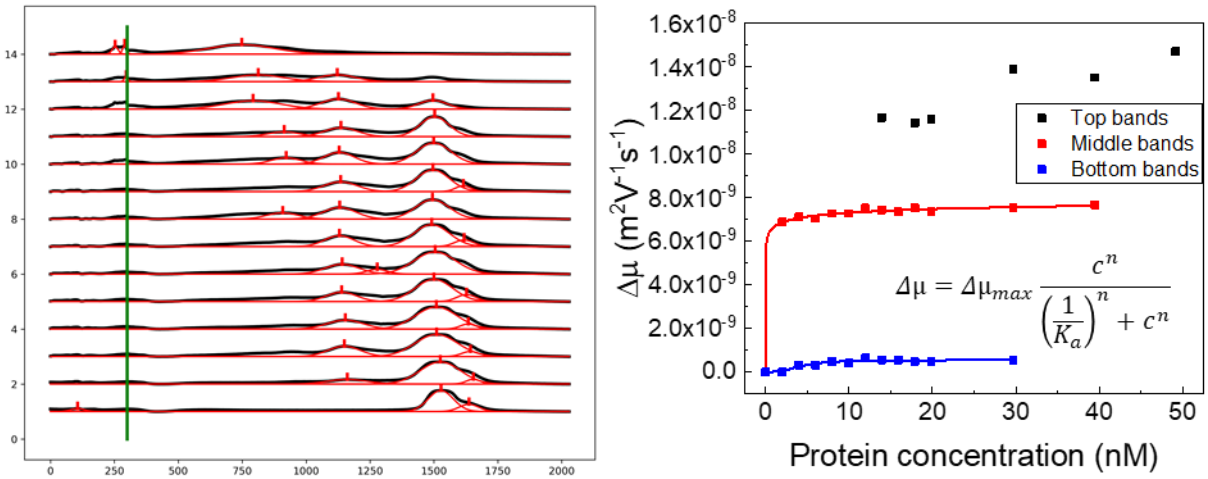

Figure 4.44. eReuss rendering of the band migration profiles for the above AGE image of a AuNP-HPF conjugates run of 20 minutes (left) and respective plot of the electrophoretic mobility difference relative to the unconjugated sample in dependence of protein concentration (right), fitted to a Hill-Langmuir equation.

The differences in the electrophoretic mobility profiles and binding constants between conjugates of smaller, 13 nm AuNP and larger, 40 nm AuNP were evaluated using BSA conjugates as a reference, which required higher protein:AuNP ratios in order to cover the entire surface of these AuNP, given the greater surface area. For this, a stock of 40 nm AuNP-MUA was kindly provided by Miguel Peixoto de Almeida, PhD. These larger conjugates migrate more slowly in the agarose gel, thus an electrophoretic run of 30 minutes was necessary for obtaining a better image with discernible band mobility differences (figure 4.45).

With an $R^2 = 0.957$, a Hill-Langmuir fitting (figure 4.46) yielded a $\Delta\mu_{max} = 6.66 \times 10^{-9}$ $m^2V^{-1}s^{-1}$, which is highly similar to that estimated for the smaller 13 nm AuNP conjugates (6.96×10^{-9} $m^2V^{-1}s^{-1}$); and a binding constant of 3.77×10^{-3}, lower than that of the 13 nm AuNP conjugates (9.01×10^{-3}).

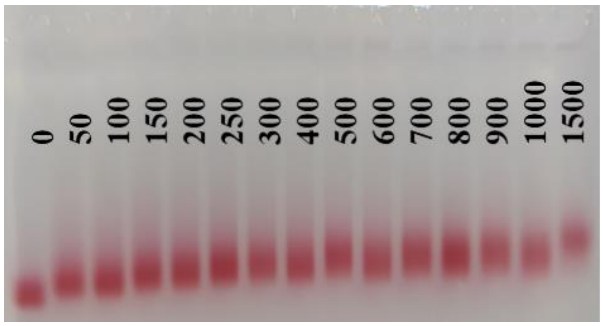

Figure 4.45. AGE bands corresponding to 40 nm AuNP-MUA 0.1 nM conjugated with different BSA:AuNP ratios, after a run of 30 minutes.

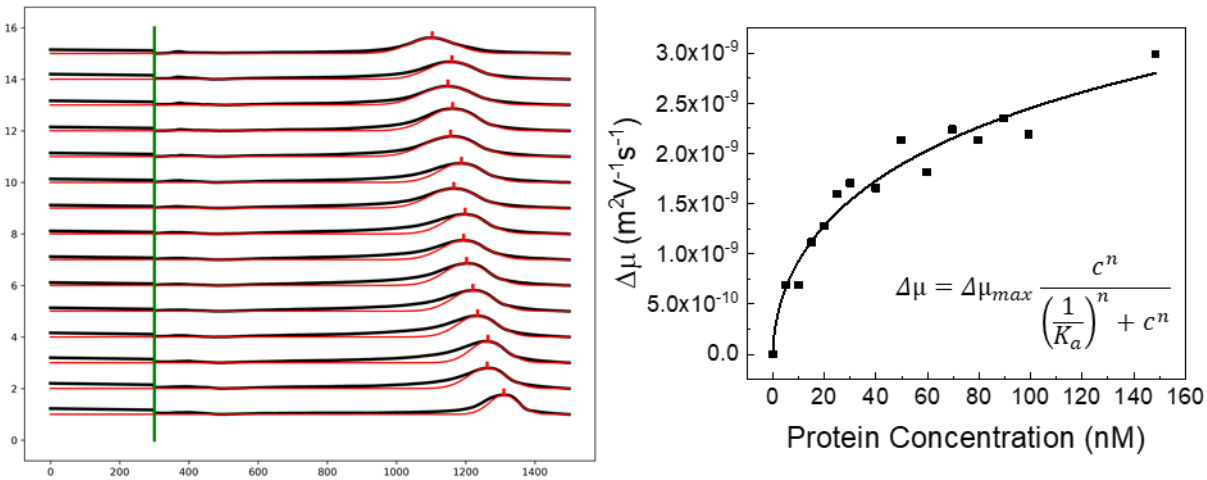

Figure 4.46. eReuss band migration profiles for the above AGE image of 40 nm AuNP conjugates with increasing BSA:AuNP ratios (left) and respective plot of the electrophoretic mobility difference relative to the unconjugated sample against protein concentration (right), fitted to a Hill-Langmuir equation.

The assessment of putative electrophoretic mobility differences between the soft and hard protein coronas was attempted through AGE assays, by preparing exact duplicates of 13 nm AuNP-MUA 2 nM conjugates samples with increasing BSA:AuNP molar ratios and centrifuging one of each pair, therefore assuming the uncentrifuged sample as the soft corona one and vice-versa. However, since the conjugates samples required a concentration step prior to loading in the gel, lest the bands would not be observable, yet having the AuNP-MUA concentrated before conjugation rendered conjugates unstable and prone to aggregate upon any further centrifugations, a compromise was found by resuspending the unconjugated AuNP-MUA pellets, after the centrifugation to remove excess capping agent, in different final volumes for each pair. Thus, the soft corona samples, which would not be submitted to a second centrifugation, were resuspended in one tenth of the discarded supernatant volume, resulting in an approximate final concentration of 20 nM, whereas the hard corona ones were resuspended in an identical volume. After the conjugation procedure, the latter were centrifuged to remove the soft corona and resuspended in one tenth of the discarded supernatant volume, matching the final concentration of the former (figures 4.47 and 4.48).

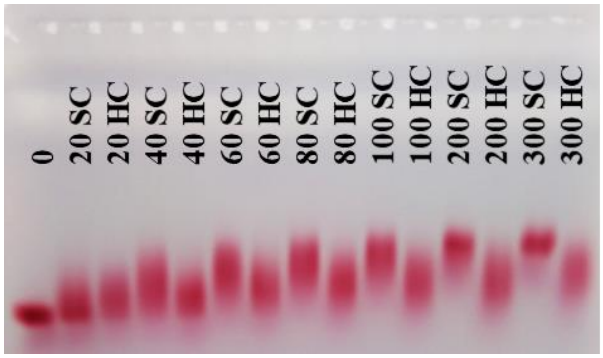

Figure 4.47. AGE bands corresponding to 13 nm AuNP-MUA conjugates in increasing BSA:AuNP ratios, in which, for every pair with the same ratio, the left and right bands correspond to uncentrifuged and centrifuged samples, of assumed soft corona (SC) and hard corona (HC), respectively.

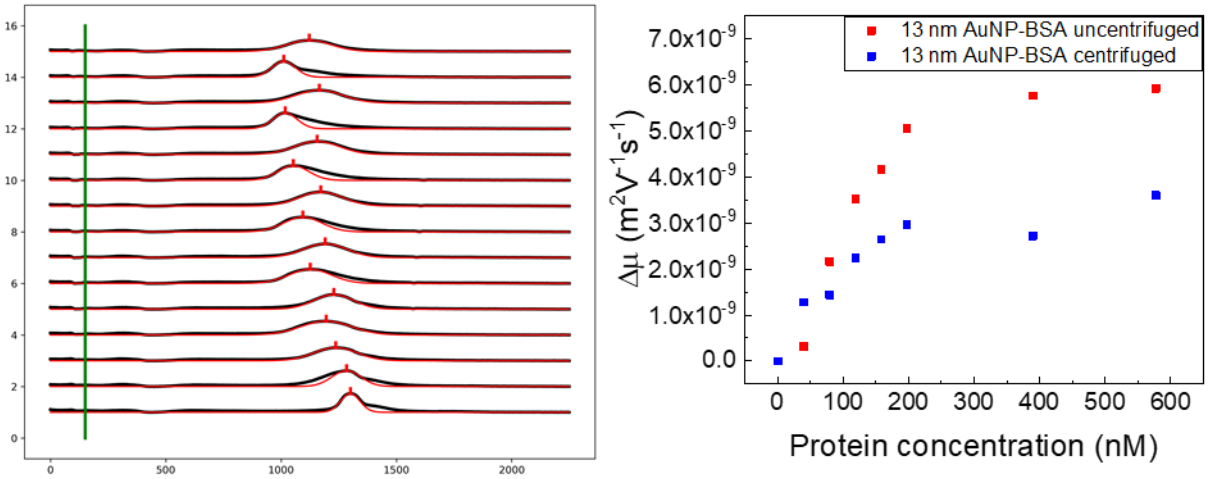

Figure 4.48. eReuss band migration profile for the above AGE image of soft and hard corona AuNP-BSA conjugates (left) and respective electrophoretic mobility difference relative to AuNP-MUA plotted in dependence of protein concentration (right) for the uncentrifuged samples, in red; and the centrifuged ones, in blue.

In order to test if this electrophoretic mobility variance observed between AuNP-BSA conjugates with identical protein:AuNP ratios was due to the removal of the soft corona through centrifugation or to another phenomenon derived from the conditions in which the samples were prepared, an AGE assay was devised to eliminate the possibility of protein corona interference.

Aliquots of 13 nm AuNP-MUA 2 nM were centrifuged once to remove excess capping agent and subsequently resuspended in different volumes prior to a conjugation procedure with BSA, as described in table 4.8, after which all samples were made up to an identical volume and immediately centrifuged a second time.

Table 4.8. Final colloidal suspension volumes in which conjugation occurred for the BSA:AuNP ratios described.

Sample	AuNP volume (µL)	BSA:AuNP ratio
1	-	0:1
2	50	20:1
3	500	
4	50	40:1
5	500	
6	50	60:1
7	500	
8	50	80:1
9	500	
10	50	100:1
11	500	
12	50	200:1
13	500	
14	50	300:1
15	500	

Based on the results (figures 4.49 and 4.50), the previous assumption that the variances observed in the electrophoretic mobility of uncentrifuged and centrifuged AuNP-BSA conjugates in the preceding AGE assay were due to the pairs of samples bearing a soft and hard corona, respectively, was reassessed, for identical results were obtained with the centrifugation of all samples.

Moreover, the electric field applied during the electrophoresis may interfere with the electrostatic interactions amongst the more loosely bound soft corona proteins, causing the detachment of these from the AuNP, which would make electrophoresis a protein corona separation method, at the minimum, as effective as centrifugation, thus precluding the visualisation of the soft and hard corona.

However, this AGE assay also revealed an overlooked phenomenon occurring in the conjugation process, in which the AuNP colloidal suspension volume appears to affect conjugation efficiency, given the electrophoretic mobility variances observed between samples conjugated in identical protein:AuNP ratios, but different AuNP volumes.

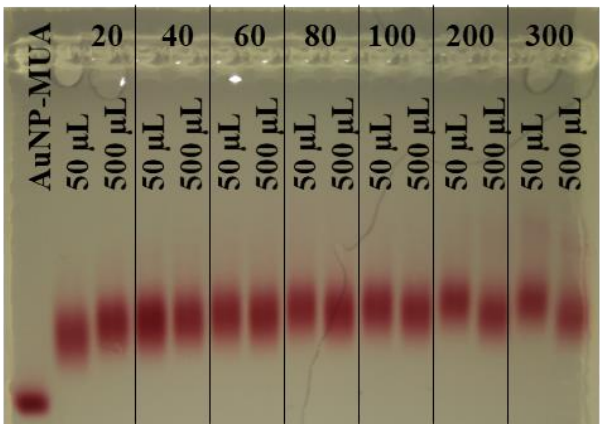

Figure 4.49. AGE bands corresponding to 13 nm AuNP-MUA conjugates in increasing BSA:AuNP ratios, in which, for every pair with the same ratio, the left and right bands were conjugated in the colloidal suspension volumes of 50 and 500 µL, respectively, with subsequent centrifugation for all samples.

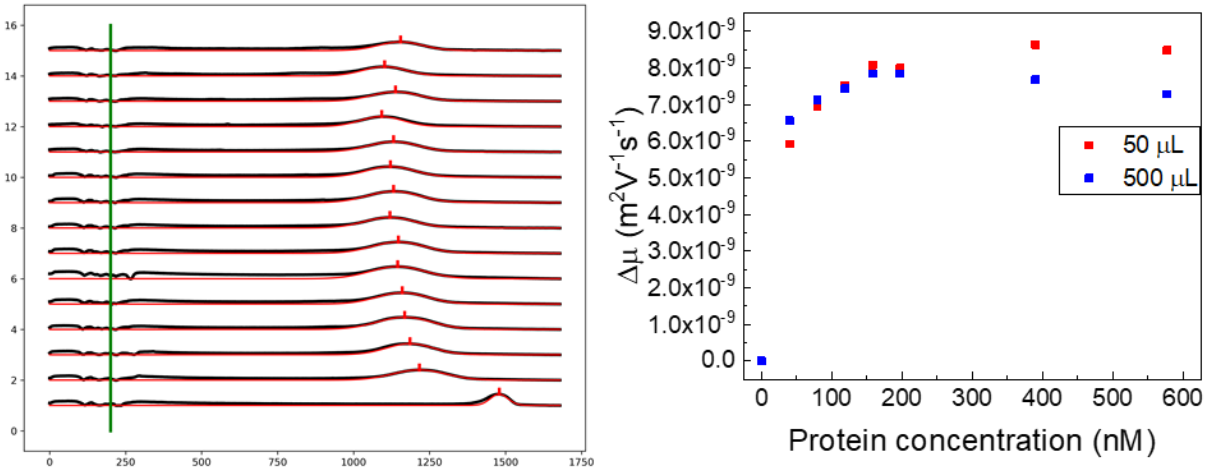

Figure 4.50. eReuss band migration profiling for the AGE image of AuNP-BSA samples conjugated in two different colloidal suspension volumes (left) and respective electrophoretic mobility difference relative to the unconjugated AuNP-MUA plotted against protein concentration (right) for the samples conjugated in 50 µL (red) and the ones conjugated in 500 µL (blue).

In order to verify if this phenomenon occurs with AuNP-MUA conjugated with the other studied proteins, a similar AGE assay was devised, with samples prepared as described in table 4.9. A complete surface coverage of the AuNP was intended, thus the selected protein:AuNP ratios were purposely high.

Table 4.9. Final colloidal suspension volumes in which conjugation with BSA, HSA, BPF or HPF occurred for the protein:AuNP ratios described.

Sample	Protein	Protein:AuNP ratio	AuNP volume (µL)
1	-	0:1	-
2	BSA	1000:1	500
3			50
4			10
5	HSA		500
6			50
7			10
8	BPF	200:1	500
9			50
10			10
11	HPF		500
12			50
13			10

After the conjugation procedure, all samples were adjusted to a final volume of 500 µL prior to the required concentration step through centrifugation, in order to have more perceptible bands. A first gel image was taken after an electrophoretic run of 20 minutes (figure 4.51).

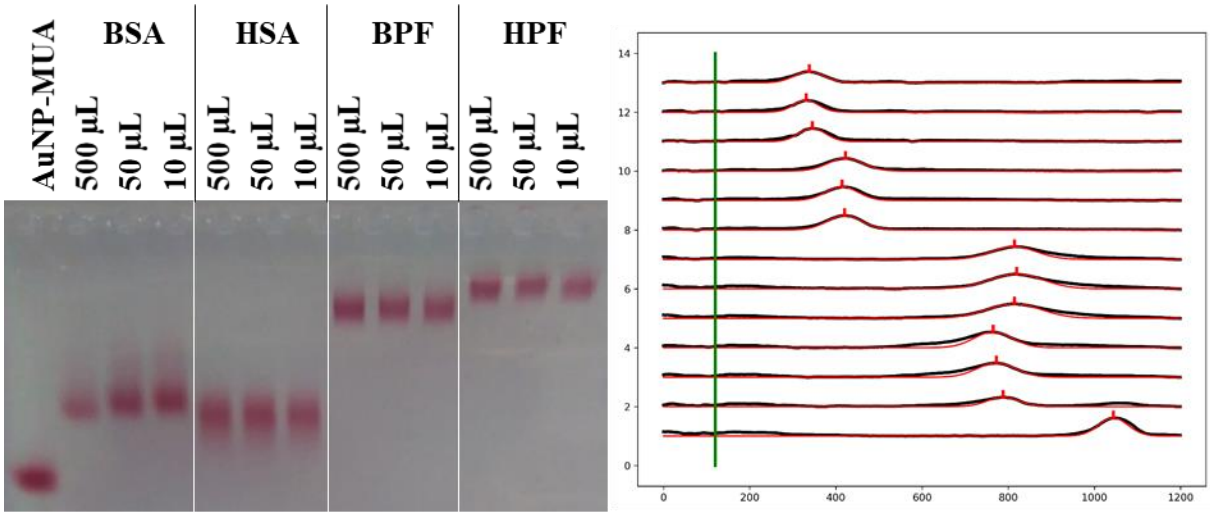

Figure 4.51. AGE bands of unconjugated AuNP-MUA and AuNP-MUA conjugated with BSA, HSA, BPF and HPF in purposely high protein:AuNP ratios, each protein conjugated in colloidal suspension volumes of 500, 50 and 10 µL, after an electrophoretic run of 20 minutes (left); and corresponding eReuss band migration profiling (right).

Although electrophoretic mobility variances were already visible between the different volumes for the BSA conjugates, this phenomenon was not perceptible on the conjugates with the other proteins, therefore – and to further accentuate these variances – the gel was submitted to an additional 10 minutes of electrophoretic run, at the cost of increased band smearing (figure 4.52).

Comparing first the electrophoretic mobility profiles between the different proteins, there were some interesting divergences, namely the fact that the human variant of serum albumin migrated further than its bovine counterpart, yet the opposite occurred with the fibrinogens. Given the great proximity between the molecular weights of bovine and human counterparts for each protein, these discrepancies may indicate a different a number of AuNP binding sites on the surfaces of these proteins, allowing the adsorption to more than one AuNP per protein.

By analysing, for each protein, the profiles between the samples conjugated in different volumes, there is a distinctive influence of colloidal suspension volume over conjugation efficiency only for BSA, as this phenomenon was not observed with the other proteins. This could be explained if the structure of BSA compresses in such way under the steric pressure of more concentrated mediums that it allows for more to fit on the surface of a AuNP, albeit this does not happen with the other proteins.

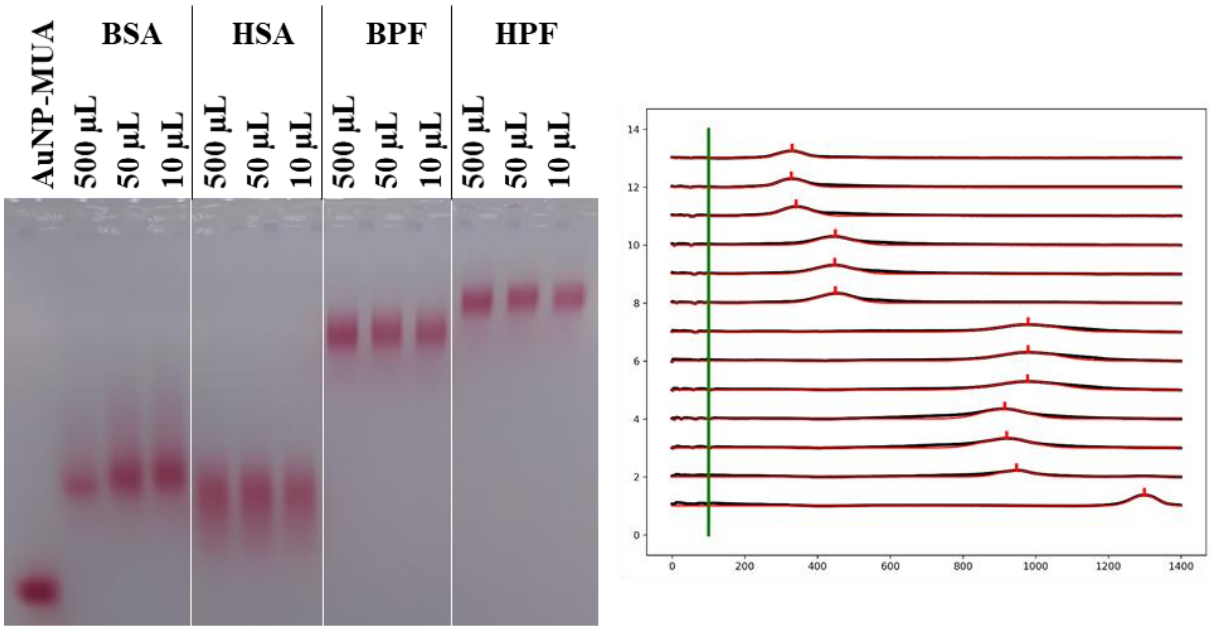

Figure 4.52. AGE bands of unconjugated AuNP-MUA and conjugated with BSA, HSA, BPF and HPF in purposely high protein:AuNP ratios, each protein conjugated in colloidal suspension volumes of 500, 50 and 10 µL, after an electrophoretic run of 30 minutes (left); and corresponding eReuss band migration profiling (right).

To further study this effect, a series of AGE assays were realised using various BSA:AuNP ratios each, with samples conjugated in different AuNP colloidal suspension volumes. For each assay, aliquots of 12 nm AuNP-MUA 1.5 nM were resuspended in final colloidal suspension volumes of 10 to 100 µL in intervals of 10 µL, then to 500 µL in intervals of 100 µL, after the centrifugation to remove excess capping agent; and subsequently conjugated with BSA in the same protein:AuNP ratio per assay, all of which are summarised in table 4.10. Good gel quality was achieved for all assays with an electrophoretic run of 20 minutes (figures 4.53 to 4.57).

Table 4.10. Preparation of samples for the AGE assay series, with varying AuNP colloidal suspension volumes and conjugated with the same BSA:AuNP ratio for each assay.

Sample	**AuNP volume (µL)**	**BSA:AuNP ratio**				
		Assay 1	Assay 2	Assay 3	Assay 4	Assay 5
1	-	0:1	0:1	0:1	0:1	0:1
2	10	20:1	40:1	60:1	80:1	100:1
3	20					
4	30					
5	40					
6	50					
7	60					
8	70					
9	80					
10	90					
11	100					
12	200					
13	300					
14	400					
15	500					

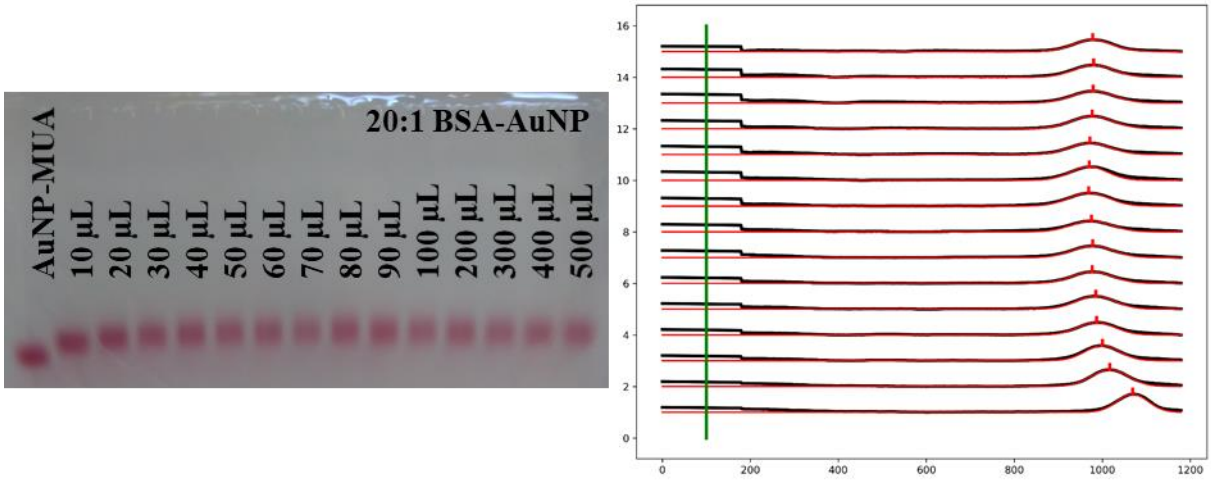

Figure 4.53. AGE bands of unconjugated AuNP-MUA and conjugated in a BSA:AuNP ratio of 20:1, in increasing colloidal suspension volumes (left); and corresponding eReuss band migration profiling (right).

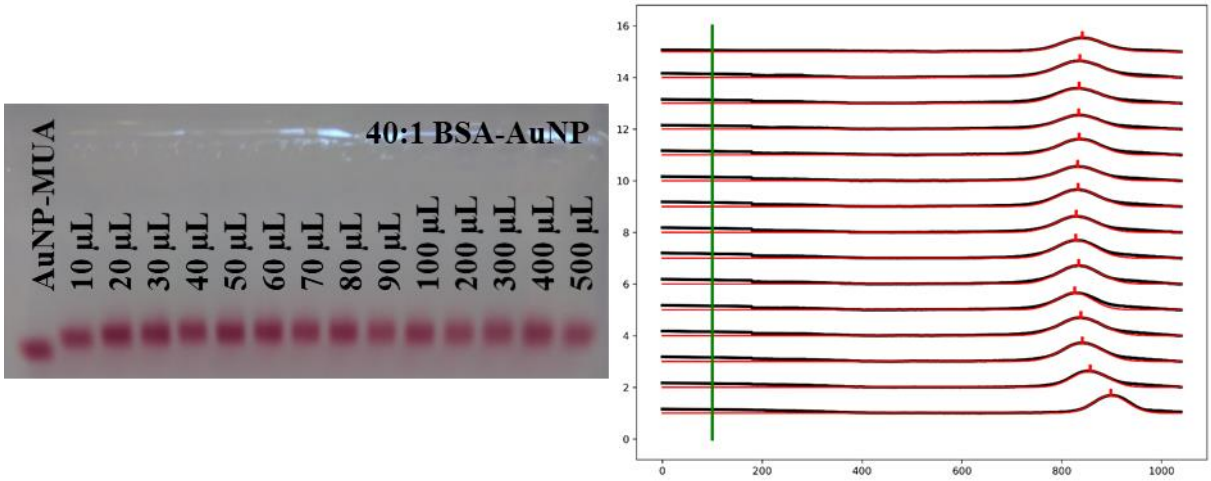

Figure 4.54. AGE bands of unconjugated AuNP-MUA and conjugated in a BSA:AuNP ratio of 40:1, in increasing colloidal suspension volumes (left); and corresponding eReuss band migration profiling (right).

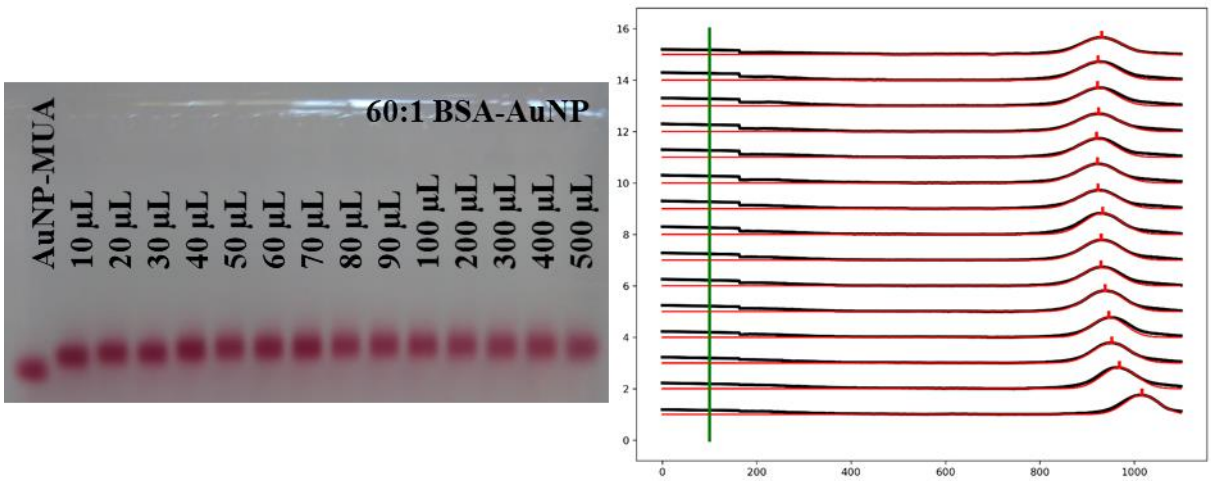

Figure 4.55. AGE bands of unconjugated AuNP-MUA and conjugated in a BSA:AuNP ratio of 60:1, in increasing colloidal suspension volumes (left); and corresponding eReuss band migration profiling (right).

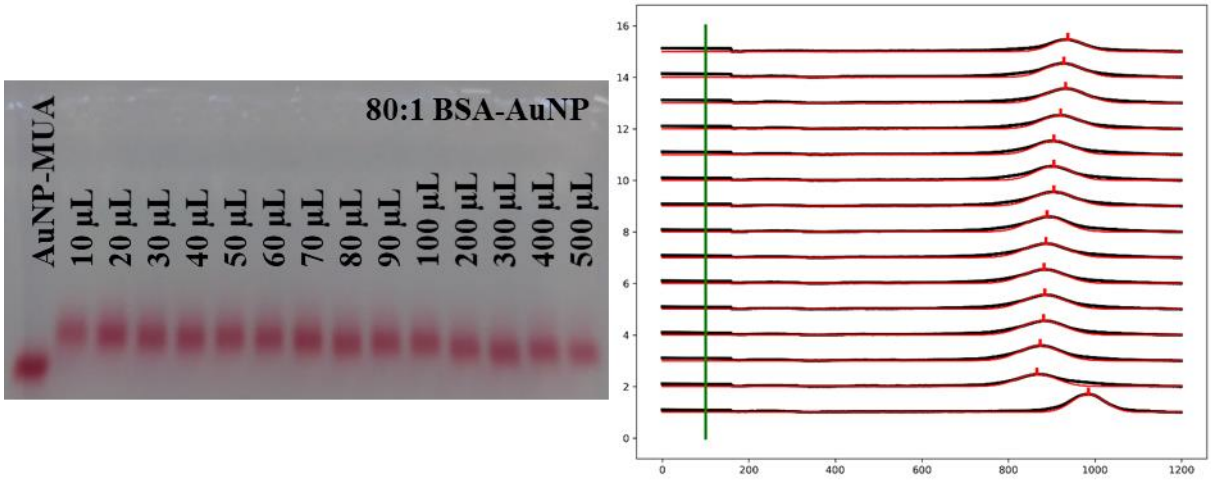

Figure 4.56. AGE bands of unconjugated AuNP-MUA and conjugated in a BSA:AuNP ratio of 80:1, in increasing colloidal suspension volumes (left); and corresponding eReuss band migration profiling (right).

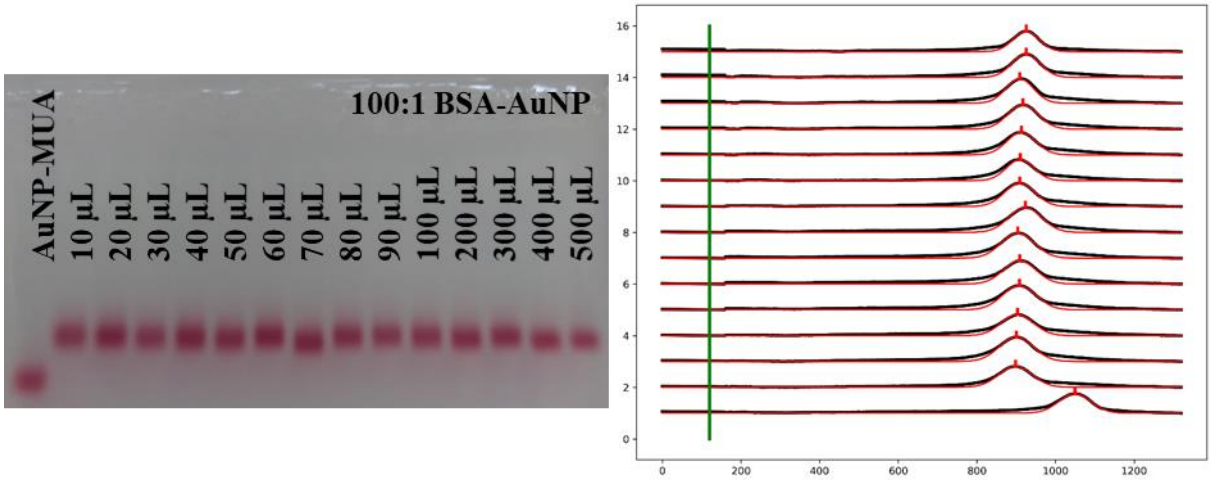

Figure 4.57. AGE bands of unconjugated AuNP-MUA and conjugated in a BSA:AuNP ratio of 100:1, in increasing colloidal suspension volumes (left); and corresponding eReuss band migration profiling (right).

The electrophoretic mobility difference relative to the unconjugated AuNP-MUA for the samples of each assay was plotted against the respective protein concentrations (figure 4.58).

For the BSA:AuNP molar ratios ≤ 60:1, conjugation was most efficient, as observed in the peaks of highest electrophoretic mobility difference in figure 4.58, at higher colloidal suspension volumes, in which the protein concentration is lower (< 1000 nM); whereas, for 80:1 and 100:1, conjugation appears more efficiency as protein concentration increases.

Since the conjugation curve for BSA reached an apparent scaffold at the protein:AuNP of 70:1, which was assumed as the required amount of this protein for a full hard corona monolayer formation, it is possible that the increased concentration of both AuNP and BSA – consequent of the decreased colloidal suspension volume during conjugation – would induce steric hindrance on the adsorption process with an insufficient amount of protein to cover the entire surface of a AuNP, which is surpassed as more protein is added. Beyond this point, the formation of the soft corona multilayers would be enhanced in environments of more concentrated AuNP and BSA. This prompts to the fact that the adsorption process is not a complete reaction and tends towards a thermodynamic equilibrium with populations of adsorbed protein as well as of unbound, free protein.

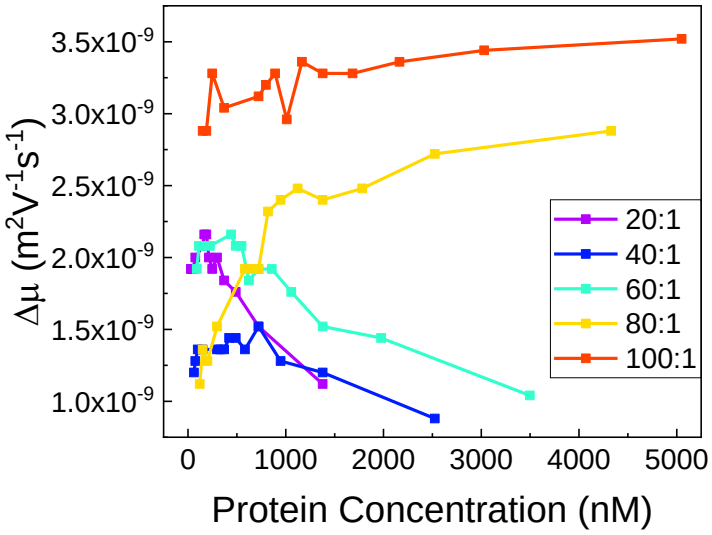

Figure 4.58. Profiles of relative electrophoretic mobility difference in dependence of protein concentration for each of the above AGE assays.

5 Conclusions and future perspectives

The studied proteins – both bovine and human counterparts of serum albumin (BSA and HSA, respectively) and fibrinogen (BPF and HPF, respectively) – were compared for sequential and structural homology. Gold nanoparticles (AuNP) functionalized with 11-mercaptoundecanoic acid (MUA) were successfully conjugated with each of the studied proteins. These single protein conjugates were studied for colloidal stability with varying ionic strength and pH, for protein conformational alterations through circular dichroism spectroscopy, for protein corona hydrodynamic diameter variations through dynamic light scattering and for electrophoretic mobility differences through agarose gel electrophoresis.

Both bovine and human counterparts of serum albumin and fibrinogen scored high sequential and structural homology, although the fibrinogen conjugates differed slightly in colloidal stability with ionic strength variation. However, in varying pH, all respective counterparts displayed quite similar colloidal stability patterns, with the gold nanoparticle conjugates withholding from irreversible aggregation until a less acidic microenvironment than unfunctionalized AuNP-citrate or even unconjugated AuNP-MUA. Moreover, comparatively to AuNP-citrate, AuNP-MUA is more advantageous as, besides the increment in stability and biocompatibility, the unconjugated gold nanoparticles would not migrate in agarose gel electrophoresis, making it impossible to estimate the binding constants by a Hill-Langmuir fitting to the conjugation curve.

The secondary structure of BSA and HSA underwent noticeable conformational alterations once adsorbed to the surface of AuNP, confirming a loss in α-helix density. Due to technical limitations of circular dichroism spectroscopy, these same measurements could not be performed for the fibrinogen conjugates. Alternatively, in the future, the secondary structure of proteins integrating the protein corona formed on a AuNP could be studied through Fourier transform infrared spectroscopy (FTIR) or nuclear magnetic resonance (NMR).[89]

Centrifugation was demonstrated to remove the soft corona, albeit with a high tendency of inducing irreversible nanoparticle aggregation. A decrease in hydrodynamic diameter for centrifuged conjugates samples was best observed for either serum albumin counterpart conjugated to 13 nm gold nanoparticles and for either fibrinogen conjugated to 42 nm gold nanoparticles. Furthermore, conjugates samples were less prone to aggregate upon centrifugation at protein:AuNP molar ratios higher than those determined, for each protein, as the minimum required to guarantee a complete coverage of the nanoparticle surface, which could be visualised in the conjugation curves exhibited in the agarose gel electrophoretic assays. For the future, the separation of soft and hard corona samples could be performed through asymmetrical flow field flow fractionation (AF4), which some studies have reported being more accurate in separating such samples, whilst much less aggressive than centrifugation, hence minimising risk of aggregation.[90] Additionally, the information provided by the hydrodynamic radius of conjugates with different protein coronas could be complemented by determining the radius of gyration, which can be measured through either multi-angle dynamic light scattering (MADLS), static light scattering (SLS) or small angle X-ray scattering (SAXS) and the ratio of which to the hydrodynamic radius is indicative of how compact the nanoparticles and the complexes formed with proteins are.[51]

Electrophoretic assays revealed the amount of HSA necessary to fully cover one gold nanoparticle is lower than that of its bovine counterpart, which could indicate both assume different orientations upon adsorbing to the nanoparticle surface. Assuming the Hill-Langmuir equation as the best fitting to the conjugation curves, further differences were discovered between respective protein counterparts, considering distinct binding constants were calculated (9.01×10^{-3} for BSA, 7.76×10^{-2} for HSA, 3.48 for BPF and 2.34×10^{-1} for HPF). Despite this, the binding constants for either serum albumin were much smaller than those of fibrinogen, which is in accordance with the Vroman effect, which states that fibrinogen possesses a higher affinity to surfaces than serum albumin. Discrepancies in the binding constants were also found for the same protein conjugated to gold nanoparticles with a different size. Moreover, colloidal gold suspension volume was determined to be an important factor for conjugation efficiency, as it was promoted at lower volumes, provided the amount of free protein available was sufficient to complete the formation of the first protein corona monolayer, or hard corona.

Finally, these experiments are to be performed on the other human blood plasma proteins, namely the globulins, including numerous proteins of various shapes and sizes and different affinities to AuNP. Furthermore, these experiments are also to be conducted on AuNP conjugates of more than one plasma protein, added at different times and varying the order, thus testing protein competition, as described by the Vroman effect. This is important, as AuNP biosensors would be exposed to whole blood samples and, therefore, the protein corona profiles would also vary with time, with proteins of lower abundance but higher affinity replacing the more abundant ones comprising the initial coronas.

6 References

1. 18.1 An Overview of Blood – Anatomy and Physiology. Available at: https://opentextbc.ca/anatomyandphysiology/chapter/an-overview-of-blood/. (Accessed: 2nd August 2019)
2. Muthusamy, B. *et al.* Plasma Proteome Database as a resource for proteomics research. *PROTEOMICS* **5**, 3531–3536 (2005).
3. Tarté, R. Meat protein ingredients. in *Handbook of Food Proteins* 56–91 (Elsevier, 2011). doi:10.1533/9780857093639.56
4. Ohwada, H., Nakayama, T., Kanaya, Y. & Tanaka, Y. Serum albumin levels and their correlates among individuals with motor disorders at five institutions in Japan. *Nutr. Res. Pract.* **11**, 57 (2017).
5. Koehler, N. K. U. *et al.* Altered Serum IgG Levels to α-Synuclein in Dementia with Lewy Bodies and Alzheimer's Disease. *PLoS ONE* **8**, e64649 (2013).
6. Luo, Y., Kim, H. S., Kim, M., Lee, M. & Song, Y. S. Elevated plasma fibrinogen levels and prognosis of epithelial ovarian cancer: a cohort study and meta-analysis. *J. Gynecol. Oncol.* **28**, (2017).
7. Hajipour, M. J., Laurent, S., Aghaie, A., Rezaee, F. & Mahmoudi, M. Personalized protein coronas: a "key" factor at the nanobiointerface. *Biomater. Sci.* **2**, 1210 (2014).
8. Hajipour, M. J. *et al.* Personalized disease-specific protein corona influences the therapeutic impact of graphene oxide. *Nanoscale* **7**, 8978–8994 (2015).
9. T., P. L., Mondal, M., Ramadas, K. & Natarajan, S. Molecular interaction of 2,4-diacetylphloroglucinol (DAPG) with human serum albumin (HSA): The spectroscopic, calorimetric and computational investigation. *Spectrochim. Acta. A. Mol. Biomol. Spectrosc.* **183**, 90–102 (2017).
10. Xiang, Y. *et al.* Fluorescence spectroscopy and molecular simulation on the interaction of caffeic acid with human serum albumin: Interaction study of Caffeic Acid with Human Serum Albumin. *Luminescence* **31**, 1496–1502 (2016).
11. Tsai, D.-H. *et al.* Adsorption and Conformation of Serum Albumin Protein on Gold Nanoparticles Investigated Using Dimensional Measurements and in Situ Spectroscopic Methods. *Langmuir* **27**, 2464–2477 (2011).
12. Fee, C. J., Billakanti, J. M. & Saufi, S. M. Methods for purification of dairy nutraceuticals. in *Separation, Extraction and Concentration Processes in the Food, Beverage and Nutraceutical Industries* 450–482 (Elsevier, 2013). doi:10.1533/9780857090751.2.450
13. Kilara, A. & Vaghela, M. N. Whey proteins. in *Proteins in Food Processing* 72–99 (Elsevier, 2004). doi:10.1533/9781855738379.1.72

14. Griffiths, W. C., Bogaars, H. A., Sheehan, C. F. & Diamond, B. S. Analysis of human serum proteins by molecular weight dependent acrylamide gel electrophoresis. *Ann. Clin. Lab. Sci.* **6**, 177–183 (1976).
15. Côté, H. C. F., Lord, S. T. & Pratt, K. P. γ-Chain Dysfibrinogenemias: Molecular Structure-Function Relationships of Naturally Occurring Mutations in the γ Chain of Human Fibrinogen. *Blood* **92**, 2195–2212 (1998).
16. Hall, C. E. The Fibrinogen Molecule: Its Size, Shape, and Mode of Polymerization. *J. Cell Biol.* **5**, 11–27 (1959).
17. Palta, S., Saroa, R. & Palta, A. Overview of the coagulation system. *Indian J. Anaesth.* **58**, 515 (2014).
18. Endres, G. F. & Scheraga, H. A. Molecular weight of bovine fibrinogen by sedimentation equilibrium. *Arch. Biochem. Biophys.* **144**, 519–528 (1971).
19. Fantl, P. & Ward, H. Molecular weight of human fibrinogen derived from phosphorus determinations. *Biochem. J.* **96**, 886–889 (1965).
20. McDonagh, J., Messel, H., McDonagh, R. P., Murano, G. & Blombäck, B. Molecular weight analysis of fibrinogen and fibrin chains by an improved sodium dodecyl sulfate gel electrophoresis method. *Biochim. Biophys. Acta BBA - Protein Struct.* **257**, 135–142 (1972).
21. Adamczyk, Z. *et al.* Fibrinogen conformations and charge in electrolyte solutions derived from DLS and dynamic viscosity measurements. *J. Colloid Interface Sci.* **385**, 244–257 (2012).
22. Peitinho, D. Interaction between Gold Nanoparticles and Blood Proteins to define Disease states. (Faculdade de Ciências e Tecnologia, Universidade NOVA de Lisboa, 2018).
23. Franco, R. & Pereira, E. Gold Nanoparticles and Proteins, Interaction. in *Encyclopedia of Metalloproteins* (eds. Kretsinger, R. H., Uversky, V. N. & Permyakov, E. A.) 908–915 (Springer New York, 2013). doi:10.1007/978-1-4614-1533-6_572
24. García-Álvarez, R., Hadjidemetriou, M., Sánchez-Iglesias, A., Liz-Marzán, L. M. & Kostarelos, K. *In vivo* formation of protein corona on gold nanoparticles. The effect of their size and shape. *Nanoscale* **10**, 1256–1264 (2018).
25. Lacerda, S. H. D. P. *et al.* Interaction of Gold Nanoparticles with Common Human Blood Proteins. *ACS Nano* **4**, 365–379 (2010).
26. Khan, I., Saeed, K. & Khan, I. Nanoparticles: Properties, applications and toxicities. *Arab. J. Chem.* S1878535217300990 (2017). doi:10.1016/j.arabjc.2017.05.011
27. Doria, G. *et al.* Noble Metal Nanoparticles for Biosensing Applications. *Sensors* **12**, 1657–1687 (2012).
28. Sperling, R. A., Rivera Gil, P., Zhang, F., Zanella, M. & Parak, W. J. Biological applications of gold nanoparticles. *Chem. Soc. Rev.* **37**, 1896 (2008).
29. Jain, S., Hirst, D. G. & O'Sullivan, J. M. Gold nanoparticles as novel agents for cancer therapy. *Br. J. Radiol.* **85**, 101–113 (2012).

30. Reddy, V. Gold Nanoparticles: Synthesis and Applications. *Synlett* **2006**, 1791–1792 (2006).
31. Wang, P. *et al.* Interaction of gold nanoparticles with proteins and cells. *Sci. Technol. Adv. Mater.* **16**, 034610 (2015).
32. Kosuda, K. M., Bingham, J. M., Wustholz, K. L. & Van Duyne, R. P. Nanostructures and Surface-Enhanced Raman Spectroscopy. in *Comprehensive Nanoscience and Technology* 263–301 (Elsevier, 2011). doi:10.1016/B978-0-12-374396-1.00110-0
33. Amendola, V., Pilot, R., Frasconi, M., Maragò, O. M. & Iatì, M. A. Surface plasmon resonance in gold nanoparticles: a review. *J. Phys. Condens. Matter* **29**, 203002 (2017).
34. Guo, L. *et al.* Strategies for enhancing the sensitivity of plasmonic nanosensors. *Nano Today* **10**, 213–239 (2015).
35. Maier, S. A. *Plasmonics: Fundamentals and Applications*. (Springer US, 2007). doi:10.1007/0-387-37825-1
36. Sepúlveda, B., Angelomé, P. C., Lechuga, L. M. & Liz-Marzán, L. M. LSPR-based nanobiosensors. *Nano Today* **4**, 244–251 (2009).
37. Liu, G. *et al.* Continuous Flow Controlled Synthesis of Gold Nanoparticles Using Pulsed Mixing Microfluidic System. *Adv. Mater. Sci. Eng.* **2015**, 1–11 (2015).
38. Diemer, M. E. Aurous Chloride. *J. Am. Chem. Soc.* **35**, 552–559 (1913).
39. Enustun, B. V. & Turkevich, J. Coagulation of Colloidal Gold. *J. Am. Chem. Soc.* **85**, 3317–3328 (1963).
40. Kumar, S., Gandhi, K. S. & Kumar, R. Modeling of Formation of Gold Nanoparticles by Citrate Method. *Ind. Eng. Chem. Res.* **46**, 3128–3136 (2007).
41. Ojea-Jiménez, I., Bastús, N. G. & Puntes, V. Influence of the Sequence of the Reagents Addition in the Citrate-Mediated Synthesis of Gold Nanoparticles. *J. Phys. Chem. C* **115**, 15752–15757 (2011).
42. Park, S.-J. & Seo, M.-K. Intermolecular Force. in *Interface Science and Technology* **18**, 1–57 (Elsevier, 2011).
43. Gumustas, M., Sengel-Turk, C. T., Gumustas, A., Ozkan, S. A. & Uslu, B. Effect of Polymer-Based Nanoparticles on the Assay of Antimicrobial Drug Delivery Systems. in *Multifunctional Systems for Combined Delivery, Biosensing and Diagnostics* 67–108 (Elsevier, 2017). doi:10.1016/B978-0-323-52725-5.00005-8
44. Selvamani, V. Stability Studies on Nanomaterials Used in Drugs. in *Characterization and Biology of Nanomaterials for Drug Delivery* 425–444 (Elsevier, 2019). doi:10.1016/B978-0-12-814031-4.00015-5
45. Adair, J. H., Suvaci, E. & Sindel, J. Surface and Colloid Chemistry. in *Encyclopedia of Materials: Science and Technology* 1–10 (Elsevier, 2001). doi:10.1016/B0-08-043152-6/01622-3
46. Ohshima, H. Interaction of colloidal particles. in *Colloid and Interface Science in Pharmaceutical Research and Development* 1–28 (Elsevier, 2014). doi:10.1016/B978-0-444-62614-1.00001-6

47. Campbell, L. DLVO Theory - folio. Available at: https://folio.brighton.ac.uk/user/lc355/dlvo-theory. (Accessed: 12th August 2019)
48. Frens, G. Particle size and sol stability in metal colloids. *Kolloid-Z. Z. Für Polym.* **250**, 736–741 (1972).
49. Zhang, Z., Zhao, L., Li, Y. & Chu, M. A Modified Method to Calculate Critical Coagulation Concentration Based on DLVO Theory. *Math. Probl. Eng.* **2015**, 1–5 (2015).
50. Hsu, J.-P. & Liu, B.-T. Critical Coagulation Concentration of a Colloidal Suspension at High Particle Concentrations. *J. Phys. Chem. B* **102**, 334–337 (1998).
51. Bhattacharjee, S. DLS and zeta potential – What they are and what they are not? *J. Controlled Release* **235**, 337–351 (2016).
52. Protein-Surface Interactions. in *An Introduction To Tissue-Biomaterial Interactions* 37–52 (John Wiley & Sons, Inc., 2003). doi:10.1002/0471270598.ch3
53. Häkkinen, H. The gold–sulfur interface at the nanoscale. *Nat. Chem.* **4**, 443–455 (2012).
54. Pensa, E. *et al.* The Chemistry of the Sulfur–Gold Interface: In Search of a Unified Model. *Acc. Chem. Res.* **45**, 1183–1192 (2012).
55. Alkilany, A. M. *et al.* Colloidal Stability of Citrate and Mercaptoacetic Acid Capped Gold Nanoparticles upon Lyophilization: Effect of Capping Ligand Attachment and Type of Cryoprotectants. *Langmuir* **30**, 13799–13808 (2014).
56. Nambara, K. *et al.* Reverse Size Dependences of the Cellular Uptake of Triangular and Spherical Gold Nanoparticles. *Langmuir* **32**, 12559–12567 (2016).
57. Kaufman, E. D. *et al.* Probing Protein Adsorption onto Mercaptoundecanoic Acid Stabilized Gold Nanoparticles and Surfaces by Quartz Crystal Microbalance and ζ-Potential Measurements. *Langmuir* **23**, 6053–6062 (2007).
58. Ballantine, D. S. *et al.* Chemical and Biological Sensors. in *Acoustic Wave Sensors* 222–330 (Elsevier, 1997). doi:10.1016/B978-012077460-9/50005-8
59. Nguyen, V. H. & Lee, B.-J. Protein corona: a new approach for nanomedicine design. *Int. J. Nanomedicine* **Volume 12**, 3137–3151 (2017).
60. Andrade, J. D. & Hlady, V. Plasma Protein Adsorption: The Big Twelve. *Ann. N. Y. Acad. Sci.* **516**, 158–172 (1987).
61. Winzen, S. *et al.* Complementary analysis of the hard and soft protein corona: sample preparation critically effects corona composition. *Nanoscale* **7**, 2992–3001 (2015).
62. Zanganeh, S., Spitler, R., Erfanzadeh, M., Alkilany, A. M. & Mahmoudi, M. Protein corona: Opportunities and challenges. *Int. J. Biochem. Cell Biol.* **75**, 143–147 (2016).
63. Li, W. & Chen, X. Gold nanoparticles for photoacoustic imaging. *Nanomed.* **10**, 299–320 (2015).
64. Nangia, S. & Sureshkumar, R. Effects of Nanoparticle Charge and Shape Anisotropy on Translocation through Cell Membranes. *Langmuir* **28**, 17666–17671 (2012).

65. Liu, W. *et al.* Protein corona formation for nanomaterials and proteins of a similar size: hard or soft corona? *Nanoscale* **5**, 1658 (2013).
66. Lim, Z.-Z. J., Li, J.-E. J., Ng, C.-T., Yung, L.-Y. L. & Bay, B.-H. Gold nanoparticles in cancer therapy. *Acta Pharmacol. Sin.* **32**, 983–990 (2011).
67. Khang, D., Lee, Y. K., Choi, E.-J., Webster, T. J. & Kim, S.-H. Effect of the protein corona on nanoparticles for modulating cytotoxicity and immunotoxicity. *Int. J. Nanomedicine* 97 (2014). doi:10.2147/IJN.S72998
68. Casals, E., Pfaller, T., Duschl, A., Oostingh, G. J. & Puntes, V. Time Evolution of the Nanoparticle Protein Corona. *ACS Nano* **4**, 3623–3632 (2010).
69. Turkevich, J., Stevenson, P. C. & Hillier, J. A study of the nucleation and growth processes in the synthesis of colloidal gold. *Discuss. Faraday Soc.* **11**, 55 (1951).
70. Kimling, J. *et al.* Turkevich Method for Gold Nanoparticle Synthesis Revisited. *J. Phys. Chem. B* **110**, 15700–15707 (2006).
71. Haiss, W., Thanh, N. T. K., Aveyard, J. & Fernig, D. G. Determination of Size and Concentration of Gold Nanoparticles from UV−Vis Spectra. *Anal. Chem.* **79**, 4215–4221 (2007).
72. Wagers, K. B., Chui, T. C. P. & Adem, S. Effect of pH on the Stability of Gold Nanoparticles and Their Application for Melamine Detection in Infant Formula. in (2014). doi:10.9790/5736-07821520
73. Gomes, I. *et al.* Controlled adsorption of cytochrome c to nanostructured gold surfaces. *J. Nanoparticle Res.* **14**, 1321 (2012).
74. He, F. BCA (Bicinchoninic Acid) Protein Assay. *BIO-Protoc.* **1**, (2011).
75. Dolinsky, T. J., Nielsen, J. E., McCammon, J. A. & Baker, N. A. PDB2PQR: an automated pipeline for the setup of Poisson-Boltzmann electrostatics calculations. *Nucleic Acids Res.* **32**, W665–W667 (2004).
76. Smith, P. K. *et al.* Measurement of protein using bicinchoninic acid. *Anal. Biochem.* **150**, 76–85 (1985).
77. Pierce BCA Protein Assay Kit - Thermo Fisher Scientific. Available at: https://www.thermofisher.com/order/catalog/product/23225?SID=srch-srp-23225. (Accessed: 15th July 2019)
78. Altschul, S. F., Gish, W., Miller, W., Myers, E. W. & Lipman, D. J. Basic local alignment search tool. *J. Mol. Biol.* **215**, 403–410 (1990).
79. Prlić, A. *et al.* Pre-calculated protein structure alignments at the RCSB PDB website: Fig. 1. *Bioinformatics* **26**, 2983–2985 (2010).
80. Kaar, J. L. *et al.* Matrix metalloproteinase-1 treatment of muscle fibrosis. *Acta Biomater.* **4**, 1411–1420 (2008).

81. Siriwardana, K., Wang, A., Vangala, K., Fitzkee, N. & Zhang, D. Probing the Effects of Cysteine Residues on Protein Adsorption onto Gold Nanoparticles Using Wild-Type and Mutated GB3 Proteins. *Langmuir* **29**, 10990–10996 (2013).
82. Siriwardana, K. *et al.* Studying the Effects of Cysteine Residues on Protein Interactions with Silver Nanoparticles. *J. Phys. Chem. C* **119**, 2910–2916 (2015).
83. Carmody, W. R. An easily prepared wide range buffer series. *J. Chem. Educ.* **40**, A386 (1963).
84. Slocik, J. M., Govorov, A. O. & Naik, R. R. Plasmonic Circular Dichroism of Peptide-Functionalized Gold Nanoparticles. *Nano Lett.* **11**, 701–705 (2011).
85. Kelly, S. M., Jess, T. J. & Price, N. C. How to study proteins by circular dichroism. *Biochim. Biophys. Acta BBA - Proteins Proteomics* **1751**, 119–139 (2005).
86. Wang, G., Yan, C., Gao, S. & Liu, Y. Surface chemistry of gold nanoparticles determines interactions with bovine serum albumin. *Mater. Sci. Eng. C* **103**, 109856 (2019).
87. Gomes, I. *et al.* Probing Surface Properties of Cytochrome *c* at Au Bionanoconjugates. *J. Phys. Chem. C* **112**, 16340–16347 (2008).
88. Ansar, S., Chakraborty, S. & Kitchens, C. pH-Responsive Mercaptoundecanoic Acid Functionalized Gold Nanoparticles and Applications in Catalysis. *Nanomaterials* **8**, 339 (2018).
89. Pederzoli, F. *et al.* Protein corona and nanoparticles: how can we investigate on?: Protein corona and nanoparticles. *Wiley Interdiscip. Rev. Nanomed. Nanobiotechnol.* **9**, e1467 (2017).
90. Weber, C., Simon, J., Mailänder, V., Morsbach, S. & Landfester, K. Preservation of the soft protein corona in distinct flow allows identification of weakly bound proteins. *Acta Biomater.* **76**, 217–224 (2018).
91. Wangoo, N., Suri, C. R. & Shekhawat, G. Interaction of gold nanoparticles with protein: A spectroscopic study to monitor protein conformational changes. *Appl. Phys. Lett.* **92**, 133104 (2008).
92. Santos, N. C. & Castanho, M. A. Teaching light scattering spectroscopy: the dimension and shape of tobacco mosaic virus. *Biophys. J.* **71**, 1641–1650 (1996).
93. Drabik, A., Bodzoń-Kułakowska, A. & Silberring, J. Gel Electrophoresis. in *Proteomic Profiling and Analytical Chemistry* 115–143 (Elsevier, 2016). doi:10.1016/B978-0-444-63688-1.00007-0
94. Kitanovski, A. *et al. Magnetocaloric Energy Conversion*. (Springer International Publishing, 2015). doi:10.1007/978-3-319-08741-2
95. Ohshima, H. Modified Henry Function for the Electrophoretic Mobility of a Charged Spherical Colloidal Particle Covered with an Ion-Penetrable Uncharged Polymer Layer. *J. Colloid Interface Sci.* **252**, 119–125 (2002).
96. Makino, K. & Ohshima, H. Electrophoretic Mobility of a Colloidal Particle with Constant Surface Charge Density. *Langmuir* **26**, 18016–18019 (2010).

Appendix

I. Techniques

I.1 Circular dichroism

An important part of understanding the behaviour of proteins as these integrate the protein corona is to detect conformational alterations upon adsorption to the surface of nanoparticles. For this purpose, circular dichroism (CD) has been a valuable technique in structural biology, which allows to determine the secondary structure of proteins in solution, as these are generally found. A CD signal arises with the absorption of circularly polarised radiation by chiral molecules, of which proteins possess various chiral chromophores, namely aromatic amino acid chains, which absorb in the 320-260 nm wavelength range; disulphide bonds, which absorb at approximately 260 nm; or peptide bonds, absorbing below 240 nm.[85] The measured circularly polarised radiation corresponds to the differential absorbance between left and right circularly polarised radiation, respectively oriented counter-clockwise and clockwise, as described in the equation:

$$\Delta A = A_L - A_R \qquad \text{Equation I.1}$$

If the amplitudes of both left and right circularly polarised radiation components are not identical, the combined radiation is elliptically polarised (figure I.1. AII), hence CD spectra are typically reported as ellipticity, θ and measured in degrees.[85] The ellipticity can be calculated from the circularly polarised radiation differential absorbance:

$$\theta = 32.98\Delta A = \tan^{-1}\frac{b}{a} \qquad \text{Equation I.2}$$

b and a are the minor and major axes of the resulting ellipse, respectively.

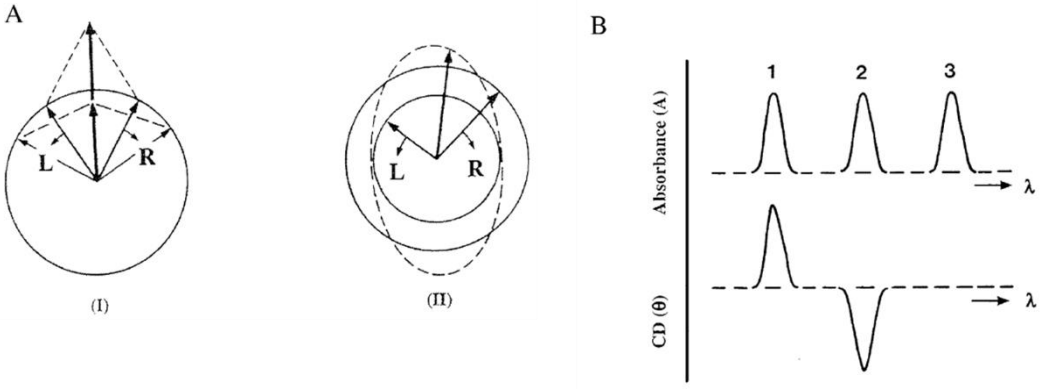

Figure I.1. Left (L) and right (R) circularly polarised light combine to generate plane polarised radiation if both have the same amplitude (AI); or elliptically polarised radiation if both have different amplitudes (AII). CD spectra bands coincide with UV-Vis absorption spectra ones, although these can be positive if L is absorbed more than R (B1), negative if R is absorbed more than L (B2) or null in achiral chromophores (B3). Adapted from [85].

CD spectra of proteins are typically measured in the far UV wavelength range, considering most protein chiral chromophores absorb in this region, as previously mentioned, as well as the fact that CD measurements in the far UV provide quantitative secondary structure estimates which can be compared to those from X-ray crystallography or nuclear magnetic resonance (figure I.2). Additionally, CD data acquired in the near UV or visible wavelengths require a much higher and more limited range of sample concentration.[85]

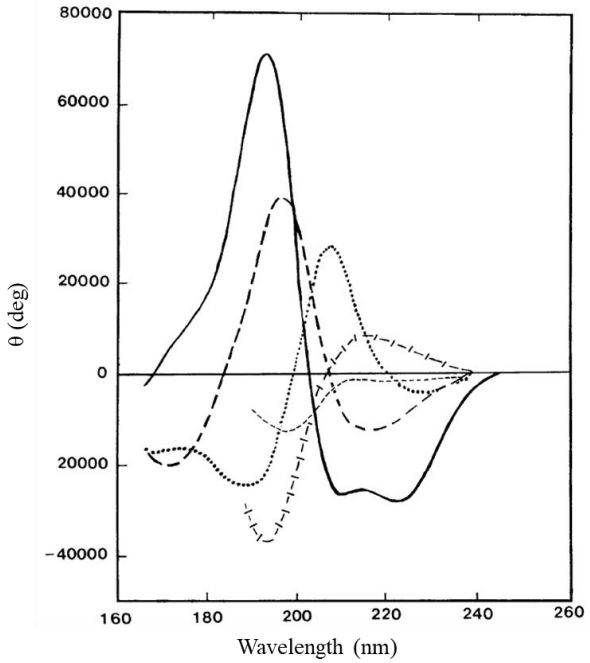

Figure I.2. CD spectra of prevalent protein secondary structures: α-helix (solid line), β-sheet (long dashed line), β-turn (dotted line), polyproline helix (cross dashed line) and random coil (short dashed line). Adapted from [85].

Since AuNP are achiral structures and thus do not exhibit chiroptical properties, these should not cause interference in the CD spectra of adsorbed proteins. Nevertheless, some noise in these spectra has been attributed to bare AuNP, which is assumed to be due to the circularly polarised radiation interacting with the electromagnetic field generated from the gold surface. However, this effect is diminished if all AuNP are properly coated with protein, as the incident circularly polarised radiation is modulated solely by the outermost molecules in a complex.[84–86,91]

I.2 Dynamic light scattering

One simple approach to characterise a complex formed of plasma proteins adsorbed to the surface of AuNP is the measurement of its increase in diameter, through which the surface density of conjugated molecules can be quantified, whilst also providing information on nanoparticle aggregation and protein compactness, thus hinting at conformational alterations.[11] Dynamic light scattering (DLS) is a technique which allows to estimate the size of solvated particles at the nanoscale based on how these scatter light from an incident laser, requiring low sample concentrations and yielding robust data on size distribution and polydispersity index (PDI). Transmission electron microscopy (TEM) can also be used for the same purpose, although samples cannot be measured in solution and must be thoroughly dried – thus making for a more extensive sample preparation procedure – whereas DLS can even measure a greater number of particles than this technique, therefore producing more reliable size distribution data.[51] Nanoparticle tracking analysis (NTA) is another alternative technique to DLS which is also based on light scattering. Both techniques estimate particle size from the diffusion coefficient, which DLS detects by correlating the scattered light intensity fluctuations over time, whereas NTA detects it by recording the mobility of diffusing particles based on the light these scatter, using charged-couple device cameras. Despite being slightly less prone to calculated particle size error than DLS, NTA is less capable of detecting particles smaller than 30 nm, besides being more complex and expensive.[51]

DLS measures the hydrodynamic diameter of suspended particles – the diameter of a hypothetical hard sphere of identical diffusion velocity – as these are in a constant motion due to density fluctuations in the colloidal suspension, known as Brownian motion. Light from an incident monochromatic laser is scattered by the dipoles formed from the oscillating electric fields of sampled particles, which originate from the interaction with the electric field of the incident light, as previously discussed. Scattered light can be shifted to different frequencies depending on particle diffusion velocity and direction relative to the detector, as per the Doppler effect. Moreover, if the particles are smaller than a tenth of the incident light wavelength, the scattered light is not angle dependent and its energy is conserved, which describes an elastic Rayleigh scattering; otherwise the anisotropic, quasi-elastic Mie scattering is observed (figure I.3).

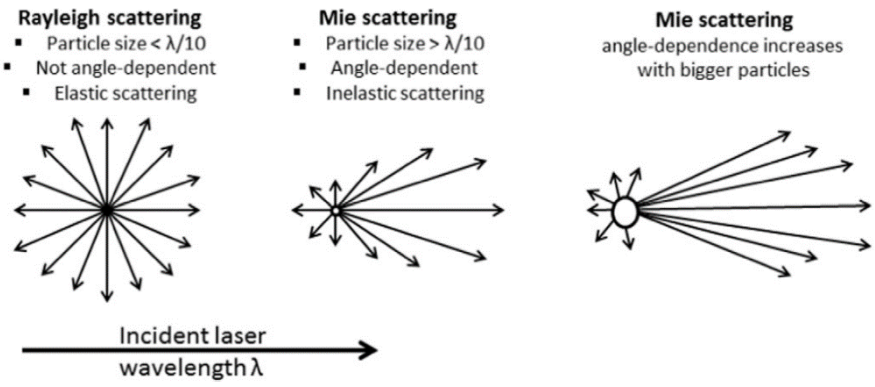

Figure I.3. Differences between Rayleigh and Mie scattering.[51]

As several particles diffuse continuously through the medium and the incident laser, constructive and destructive interferences are detected on the scattered light intensity over time. These scattered light intensity fluctuations are thus correlated against short decay intervals, τ and an intensity auto-correlation function (ACF), G can be obtained through the following equation:

$$G(\tau) = 1 + be^{-2D_t q^2 \tau} \quad \text{Equation I.3}$$

b is a constant dependent on the DLS instrument and optical settings, D_t the translational diffusion coefficient – obtained through the Stokes-Einstein equation – and q the scattering vector, which can be expressed as:

$$D_t = \frac{k_B T}{6\pi\eta R_H} \quad \text{Equation I.4}$$

$$|q| = \frac{4\pi n_0}{\lambda_0 \sin\frac{\theta}{2}} \quad \text{Equation I.5}$$

k_B is the Boltzmann constant, T the temperature, η the dispersant viscosity, R_H the hydrodynamic radius, n_0 the solvent refractive index, λ_0 the laser wavelength in vacuum and θ the scattering angle. The PDI corresponds to the calculated particle hydrodynamic diameter for each scattered light intensity peak measured over time divided by the mean. Sampled particles with a PDI < 0.1 can be considered virtually monodisperse, whilst a PDI of 0.1-0.4 or > 0.4 indicates moderate and high polydispersity, respectively. In sufficiently polydisperse samples, larger particles scatter light with much more intensity than smaller ones – given the scattered light intensity is proportional to the sixth power of the particle hydrodynamic radius – thus compromising an accurate size estimation for the entire population, as the smaller particles go undetected. Additionally, too concentrated samples can also induce such measurement imprecisions, since the light scattered by one particle has a greater probability to be scattered again by another in close proximity, therefore producing erroneous results which can even mislead the instrument into assuming a cluster of neighbouring smaller particles as a single larger one. Despite these issues related to samples, one limitation inherent to this technique is its relatively low resolution, as it can only distinguish particle sizes differing by a minimum factor of three (for example, 10 and 30 nm, or 50 and 150 nm), considering anything below this threshold as one single broad peak, instead of two individual peaks.[51,92]

I.3 Electrophoresis

Suspended molecules such as nanoparticles or proteins – or complexes formed of both – possess an electric surface charge and thus migrate in solution as an external electric field is applied. This effect is exploited in various electrophoretic techniques for the separation of such suspended molecules based on charge and, in the specific case of gel electrophoresis, shape, size and molecular weight, as these are forced to migrate through the pores of the gel. Considering null molecular dynamics in the course of an electrophoretic assay, meaning no chemical reactions occur amongst the sampled molecules, molecular dynamics occur at a uniform rate and with a constant migration ratio, which is influenced by the applied electric current, the shape, size and hydrophobicity of the molecules being separated, the ionic strength and viscosity of the solvent and the temperature.[93] The electrophoretic mobility, μ can thus be calculated through the following equation:

$$\mu = \frac{v}{E} = \frac{Z}{f} \qquad \text{Equation I.6}$$

$$f = 6\pi\eta r \qquad \text{Equation I.6}$$

v is the migration velocity, *E* the electric field strength, *Z* the total molecular charge, *f* the friction coefficient, η the medium viscosity and *r* the molecule radius. In a uniform electric field, E corresponds to the negative quotient of the electric potential difference, V and the distance separating the electrodes, d, which is expressed as:

$$E = -\frac{V}{d} \qquad \text{Equation I.7}$$

As the charged molecules under an electric field are driven towards the electrode of the opposite charge through an electrostatic coulombic force, the opposite occurs for counterions in solution, which can also integrate the diffuse layer of the sampled molecules, as previously discussed. The force applied onto the counterions in the diffuse layer of a molecule generates a drag – a retardation force – of which a part is transferred to the molecule surface by viscous stress (figure 1.19). The thickness of the EDL is directly proportional to the distance between the retardation force point of application and the molecule surface and, consequently, inversely proportional to the retardation force applied onto the molecule.[94]

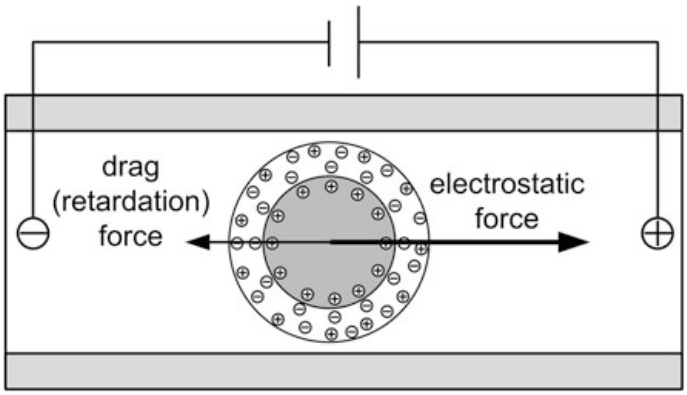

Figure I.4. Electrophoretic flow of a positively charged particle.[94]

Given the relationship between the EDL of a suspended molecule and its electrophoretic mobility (μ), its ζ-potential (ζ) can be obtained through Henry's equation:

$$\mu = \frac{\varepsilon_r \varepsilon_0 \zeta}{\eta} f(\kappa r) \qquad \text{Equation I.8}$$

$$f(\kappa r) = \{1 - e^{\kappa r}[5E_7(\kappa r) - 2E_5(\kappa r)]\} \qquad \text{Equation I.9}$$

ε_r is the relative permittivity of the solution, ε_0 the permittivity of vacuum, η the solvent viscosity, $f(\kappa r)$ Henry's function of the product of the Debye-Hückel parameter (κ) and the radius of the molecule (r) and $E_n(\kappa r)$ the exponential integral of order n. As the thickness of the EDL (κ^{-1}) decreases, f(κr) tends to unity, as described by the Smoluchowski theory; conversely, for an EDL of infinite thickness, it tends to a value of 2/3, which corresponds to the Hückel approximation.[93–96]

I.3.1 Agarose gel electrophoresis

A common and simple technique used for the separation of biomolecules such as nucleic acids, proteins or nanoparticle-protein conjugates, agarose gel electrophoresis (AGE) has samples placed in a gel matrix of agarose and forced to migrate horizontally through the gel pores by an electric field applied from placing two electrodes of opposite charge on both extremities of the gel matrix (figure I.5). Sample migration is visualised by dying these either before or after an electrophoretic assay, although this is unnecessary for AuNP and its conjugates with protein, given the red colour characteristic to these nanoparticles. The porosity, viscosity and conductivity of the gel can be tuned by adjusting the buffer composition and agarose concentration, which is inversely proportional to pore size and, consequently, affects the size range of the molecules being separated.[93]

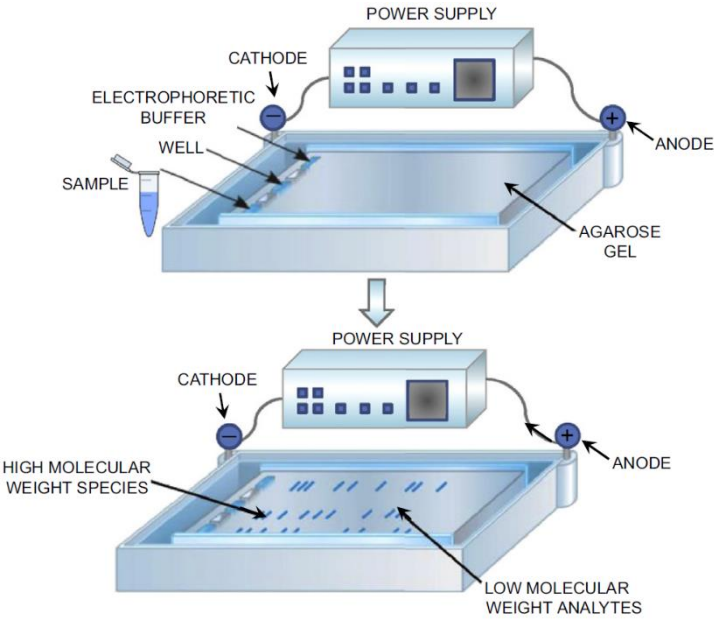

Figure I.5. Agarose gel electrophoresis system.[93]

I.3.2 SDS-PAGE

Sodium dodecyl sulphate-polyacrylamide gel electrophoresis (SDS-PAGE) is an electrophoretic technique based on a gel matrix, differing from AGE in that the gel is polymerised from acrylamide and bisacrylamide in the presence of the cross-linking agent ammonium persulphate, which yields a well-defined, well-structured matrix of more finely tuneable pore sizes and a higher molecular weight resolution comparatively to agarose. SDS-PAGE also requires two gels, one more concentrated for the separation of samples and another in which these are loaded and allowed to concentrate prior to applying the electric field, respectively denominated the resolving and stacking gels. Since two gels are required to polymerise atop one another, this results in a vertically oriented gel matrix (figure I.6).[93]

The molecular weight of proteins can be determined through this technique. As proteins possess distinct surface electrostatic potentials and structural conformations, in order to have a separation based solely on molecular weight differences, these are typically denatured by the anionic detergent sodium dodecyl sulphate – hence the SDS part in SDS-PAGE, distinguishing it from a native PAGE – prior to the electrophoretic assay. This detergent imparts a uniform negative charge to the proteins, allowing separation to be based only on molecular weight. In SDS-PAGE, denatured proteins are fragmented into its component chains by using a thiol reducing agent such as β-mercaptoethanol. These denatured proteins assume an elongated form and acquire an evenly distributed negative surface charge.[93]

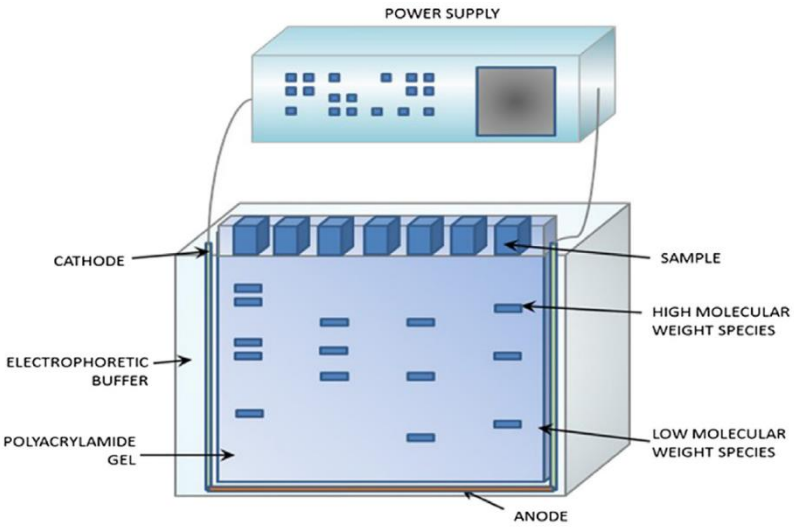

Figure I.6. Electrophoretic protein separation through SDS-PAGE.[93]

II. Reagents and instruments

Reagents:

11-mercaptoundecanoic acid, ≥ 95%, Sigma-Aldrich

Absolute ethanol, HPLC grade, ≥ 99.9%, Carlo Erba

Acrylamide/bis-acrylamide, 30% (w/v), Bio-Rad

Agarose, low electroendosmosis, Sigma

Ammonium persulfate (APS), ≥ 98%, Sigma-Aldrich

Bicinchoninic acid solution, Supelco (Sigma-Aldrich)

Bovine plasma fibrinogen, lyophilised powder, 65-85%, Sigma-Aldrich

Bovine serum albumin protein standard, 1 mg/mL, ≥ 99.9%, Sigma-Aldrich

Bovine serum albumin, lyophilised powder, ≥ 96%, Sigma-Aldrich

Bromophenol blue, ≥ 99.5%, PanReac AppliChem

Coomassie brilliant blue R-250, Sigma-Aldrich

Copper(II) sulphate pentahydrate, ≥ 98.0%, Sigma-Aldrich

Ethylenediaminetetraacetic acid (EDTA) 0.5 M, ≥ 98%, Honeywell Fluka

Glacial acetic acid, 98.5%, Carlo Erba

Glycerol, ≥ 99.5%, Sigma Aldrich

Glycerol, 87%, PanReac AppliChem

Glycine, ≥ 99%, Sigma

Gold(III) chloride solution, ≥ 99.99%, 30% (w/w) in dilute HCl, Sigma-Aldrich

Human plasma fibrinogen, lyophilised powder, 50-70%, Sigma-Aldrich

Human serum albumin, lyophilised powder, ≥ 96%, Sigma-Aldrich

Hydrochloric acid, ≥ 37%, Honeywell Fluka

Methanol, ≥ 99.9%, Fisher Scientific

Nitric acid, 65%, PanReac AppliChem

Potassium phosphate dibasic, anhydrous, ≥ 98%, Sigma-Aldrich

Potassium phosphate monobasic, anhydrous, ≥ 99%, Sigma-Aldrich

Sodium chloride, ≥ 99.5%, Scharlau

Sodium citrate tribasic dihydrate, ≥ 99.0%, Sigma-Aldrich

Sodium dodecyl sulphate (SDS), ≥ 98.5%, Sigma Aldrich

Sodium hydroxide, pellets (anhydrous), ≥ 98%, Sigma-Aldrich

Tetramethylethylenediamine (TEMED), ≥ 99%, VWR Life Science AMRESCO

Tris(hydroxymethyl)aminomethane, ≥ 99.5%, Carlo Erba

Unstained low range SDS-PAGE standards, Bio-Rad

β-mercaptoethanol, Sigma-Aldrich

Instruments:

Bio-Rad Mini-PROTEAN Tetra Electrode Assembly

Bio-Rad Mini-PROTEAN Tetra Vertical Electrophoresis Cell

Bio-Rad Mini-Sub Cell GT

Bio-Rad PowerPac Basic Power Supply

Biosan TS-100 Thermo-Shaker

Centurion Scientific K3 Series centrifuge, rotor BRK5424

Chirascan qCD spectrometer

Crison pH meter Basic 20+

Hellma quartz cuvette, 1 mm path length

Hellma quartz cuvette, 10 mm path length

HORIBA SZ-100 nanopartica analyser

J.P. Selecta Agimatic-N magnetic stirrer with heating plate

Macherey-Nagel pH-Fix 0-14 pH test strips

RADWAG AS 220/C/2 analytical balance

Sarstedt PMMS cuvettes, 4 openings

Varian Cary 50 Bio UV-Vis spectrophotometer

III. Characterisation of gold nanoparticle

Table III.1. Estimated molar extinction coefficients, ε at a wavelength of 450 nm for gold nanoparticles of a size, d ranging from 2 to 100 nm.

d/ nm	ε_{450} / $M^{-1}cm^{-1}$	*d*/ nm	ε_{450} / $M^{-1}cm^{-1}$	*d*/ nm	ε_{450} / $M^{-1}cm^{-1}$
2	4.25E+05	35	3.21E+09	68	2.50E+10
3	1.49E+06	36	3.52E+09	69	2.61E+10
4	3.62E+06	37	3.84E+09	70	2.71E+10
5	7.20E+06	38	4.18E+09	71	2.82E+10
6	1.26E+07	39	4.54E+09	72	2.93E+10
7	2.03E+07	40	4.92E+09	73	3.05E+10
8	3.07E+07	41	5.32E+09	74	3.16E+10
9	4.43E+07	42	5.74E+09	75	3.28E+10
10	6.15E+07	43	6.18E+09	76	3.40E+10
11	8.27E+07	44	6.65E+09	77	3.52E+10
12	1.09E+08	45	7.13E+09	78	3.64E+10
13	1.39E+08	46	7.65E+09	79	3.77E+10
14	1.76E+08	47	8.18E+09	80	3.89E+10
15	2.18E+08	48	8.74E+09	81	4.02E+10
16	2.67E+08	49	9.32E+09	82	4.14E+10
17	3.24E+08	50	9.92E+09	83	4.27E+10
18	3.87E+08	51	1.06E+10	84	4.40E+10
19	4.60E+08	52	1.12E+10	85	4.53E+10
20	5.41E+08	53	1.19E+10	86	4.65E+10
21	6.31E+08	54	1.26E+10	87	4.78E+10
22	7.31E+08	55	1.33E+10	88	4.91E+10
23	8.42E+08	56	1.41E+10	89	5.04E+10
24	9.64E+08	57	1.48E+10	90	5.17E+10
25	1.10E+09	58	1.57E+10	91	5.30E+10
26	1.24E+09	59	1.65E+10	92	5.43E+10
27	1.40E+09	60	1.73E+10	93	5.56E+10
28	1.58E+09	61	1.82E+10	94	5.69E+10
29	1.76E+09	62	1.91E+10	95	5.82E+10
30	1.96E+09	63	2.00E+10	96	5.94E+10
31	2.18E+09	64	2.10E+10	97	6.07E+10
32	2.41E+09	65	2.19E+10	98	6.19E+10
33	2.66E+09	66	2.29E+10	99	6.31E+10
34	2.93E+09	67	2.40E+10	100	6.44E+10

IV. Dynamic light scattering supplemental information

Table IV.1. DLS hydrodynamic diameter data of 13 and 42 nm AuNP-MUA samples conjugated with a purposely excessive amount of BSA, HSA, BPF and HPF; of soft corona (SC) and hard corona (HC).

Sample			Peak mode (nm)	Z-average (nm)	Polydispersity index
13 nm AuNP	BSA	SC	68.9	64.4	0.550
		HC	68.3	107.8	0.589
	HSA	SC	32.9	181.2	0.535
		HC	25.9	147.2	0.557
	BPF	SC	42.6	3095.4	6.287
		HC	77.7	4003.9	1.983
	HPF	SC	56.2	2679.7	2.866
		HC	69.6	13596.3	2.713
42 nm AuNP	BSA	SC	87.1	75.4	0.293
		HC	77.6	79.3	0.258
	HSA	SC	68.2	62.2	0.221
		HC	77.9	82.6	0.184
	BPF	SC	87.0	86.1	0.075
		HC	77.5	83.7	0.140
	HPF	SC	87.1	82.9	0.29
		HC	87.2	87.8	0.123

Table IV.2. DLS hydrodynamic diameter data of 42 nm AuNP-MUA samples conjugated with BSA, HSA, BPF and HPF in increasing protein:AuNP ratios; of soft corona (SC) and hard corona (HC).

Sample		**Peak mode (nm)**		**Z-average (nm)**		**Polydispersity index**	
		SC	HC	SC	HC	SC	HC
BSA-AuNP	20:1	53.6	60.5	47.5	54.5	0.404	0.240
	40:1	53.6	60.4	49.1	54.1	0.208	0.230
	60:1	47.6	60.4	46.1	54.0	0.537	0.263
	80:1	53.6	60.5	47.8	56.7	0.293	0.174
	100:1	53.7	60.9	46.7	57.0	0.373	0.159
HSA-AuNP	20:1	53.6	60.5	49.1	54.2	0.247	0.274
	40:1	53.5	60.5	47.5	56.3	0.280	0.137
	60:1	47.7	60.5	48.0	55.3	0.179	0.244
	80:1	47.7	53.7	46.5	49.6	0.380	0.521
	100:1	53.5	60.8	48.3	57.1	0.303	0.293
BPF-AuNP	20:1	68.6	87.5	65.4	74.3	0.280	0.334
	40:1	99.5	98.4	81.5	82.0	0.278	0.280
	60:1	126.7	77.2	93.7	67.2	0.454	0.597
	80:1	99.1	60.6	95.8	395.1	0.394	0.825
	100:1	99.5	77.2	103.3	67.1	0.496	0.399
HPF-AuNP	20:1	60.8	68.7	58.8	64.3	0.170	0.304
	40:1	68.6	98.5	59.6	86.4	0.324	0.218
	60:1	68.5	77.3	62.1	70.7	0.343	0.500
	80:1	87.2	87.5	72.1	78.9	0.349	0.442
	100:1	87.4	87.3	89.6	84.6	0.423	0.359